DISSERTATION

ENVIRONMENTAL CONTROLS AND AEROSOL IMPACTS ON TROPICAL SEA BREEZE CONVECTION

Submitted by

Jungmin Park

Department of Atmospheric Science

In partial fulfillment of the requirements

For the Degree of Doctor of Philosophy

Colorado State University

Fort Collins, Colorado

Fall 2020

Doctoral Committee:

Advisor: Susan C. van den Heever

Daniel S. Cooley
Sonia M. Kreidenweis
Steven D. Miller
Kristen L. Rasmussen

ABSTRACT

ENVIRONMENTAL CONTROLS AND AEROSOL IMPACTS ON TROPICAL SEA BREEZE CONVECTION

Nearly half of the world's human population resides within 150 km of the ocean, and this coastal population is expected to continue increasing over the next several decades. The accurate prediction of convection and its impacts on precipitation and air quality in coastal zones, both of which impact all life's health and safety in coastal regions, is becoming increasingly critical. Thermally driven sea breeze circulations are ubiquitous and serve to initiate and support the development of convection. Despite their importance, forecasting sea breeze convection remains very challenging due to the coexistence, covariance, and interactions of the thermodynamic, microphysical, aerosol, and surface properties of the littoral zone. Therefore, the overarching goal of this dissertation research is to enhance our understanding of the sensitivity of sea breeze circulation and associated convection to various environmental parameters and aerosol loading. More specifically, the objectives are the following: (1) to assess the relative importance of ten different environmental parameters previously identified as playing critical roles in tropical sea breeze convection; and (2) to examine how enhanced aerosol loading affects sea breeze convection through both microphysical and aerosol-radiation interactions, and how the environment modulates these effects.

In the first study, the relative roles of five thermodynamic, one wind, and four land/ocean-surface properties in determining the structure and intensity of sea breeze convection are evaluated using ensemble cloud-resolving simulations combined with statistical emulation.

The results demonstrate that the initial zonal wind speed and soil saturation fraction are the primary controls on the inland sea breeze propagation. Two distinct regimes of sea breeze-initiated convection, a shallow and a deep convective mode, are also identified. The convective intensity of the shallow mode is negatively correlated by the inversion strength, whereas the boundary layer potential temperature is the dominant control of the deep mode. The processes associated with these predominant controls are analyzed, and the results of this study underscore possible avenues for future improvements in numerical weather prediction of sea breeze convection.

The sea breeze circulation and associated convection play an important role in the transport and processing of aerosol particles. However, the extent and magnitude of both direct and indirect aerosol effects on sea breeze convection are not well known. In the second part of this dissertation, the impacts of enhanced aerosol concentrations on sea breeze convection are examined. The results demonstrate that aerosol-radiation-land surface interactions produce less favorable environments for sea breeze convection through direct aerosol forcing. When aerosol-radiation interactions are eliminated, enhanced aerosol loading leads to stronger over-land updrafts in the warm-phase region of the clouds through increased condensational growth and latent heating. This process occurs irrespective of the sea breeze environment. While condensational invigoration of convective updrafts is therefore robust in the absence of aerosol direct effects, the cold-phase convective responses are found to be environmentally modulated, and updrafts may be stronger, weaker, or unchanged in the presence of enhanced aerosol loading. Surface precipitation responses to aerosol loading also appear to be modulated by aerosol-radiation interactions and the environment. In the absence of the aerosol direct effect, the impacts of enhanced aerosol loading may produce increased, decreased, or unchanged accumulated surface precipitation, depending on the environment in which the convection develops. However, when aerosols are allowed to interact with the radiation, a consistent reduction in surface precipitation with increasing aerosol loading is observed, although the environment once again modulated the magnitude of this aerosol-induced reduction.

ACKNOWLEDGMENTS

This work would not have been possible without the support of a number of different people. Thanks to their love and encouragement, I have made it to this final milestone in my academic career, became a more resilient person, and have learned a lot about myself in the process - it has been such an honor to have them throughout my Ph.D. journey! First and foremost, I would like to thank my advisor, Dr. Susan van den Heever, for asking me tough questions, training me to be a better presenter, writer, and scientist, supporting me to participate in summer schools, field opportunities, and conferences, and most importantly, being patient with me. Her insights on what we do and do not know about cloud processes as a community have always inspired and motivated me. I also thank my doctoral committee members, Drs. Sonia Kreidenweis, Steven Miller, Kristen Rasmussen, and Daniel Cooley, for their willingness to serve on my committee and to share their insights and time.

The coauthors of the paper presented in Chapter 2 should also be acknowledged for their contributions, as I have learned so much from them: Dr. Adele Igel for teaching me how to make science fun and letting me vent when I struggled; Dr. Jill Johnson for answering questions in the process of applying the emulation approach and interpreting statistical results meaningfully, as well as sharing R codes; Dr. Leah Grant for guiding me through process-level thinking and spending time with me outside of work over a wide range of places from Fort Collins to Yellowstone National Park; Steve Saleeby for addressing all of my RAMS-related questions and providing me snacks and cat pictures; Dr. Steven Miller for helping me to see the bigger picture and think about future observational needs; and Dr. Jeff Reid for providing observational perspectives.

I am greatly indebted to the past and current members of the van den Heever group for their abundant scientific and emotional support: Jennie Bukowski, Dr. Aryeh Drager, Nick Falk, Sean Freeman, Dr. Leah Grant, Dr. Ross Heikes, Stephen Herbener, Dr. Adele Igel, Dr. Matt Igel, Dr. Stacey Kawecki, Bee Leung, Brianna Lund, Dr. Peter Marinescu, Yasutaka Murakami, Dr. Bowen Pan, Dr. Emily Riley Dellaripa, Steve Saleeby, Alex Sokolowsky, and Kristen Van Valkenburg. Each and every one has nurtured me to be a better team player at work and a more emotionally intelligent friend. I am incredibly grateful to my office mate and office neighbor, Jennie Bukowski and Sean Freeman, respectively. Together with them, I have flown drones in the field, played golf and intermural sports outside of work, and had human interactions even during the daunting COVID-19 era. I would also like to thank the entire CSU Department of Atmospheric Science for being a friendly and welcoming community to be part of.

Before starting my Ph.D. program, I worked with Dr. Hui Su at the Jet Propulsion Laboratory (JPL). I could not have been where I am now without her opening the door for me and always giving me a warm hug and fruitful advice. The three months of visiting research opportunities and one summer school at JPL have left me a great deal of friendship. Drs. Kyo Lee, Luis Millan, Jonathan Murphy, Kathleen Schiro, Hanii Takahashi, and Robert Thurstans have always been there for me. Thank you all.

Several other people should be explicitly acknowledged here for their invaluable friendship: Eunice Park for being a shoulder to cry on and offering a home to rest at over spring breaks; Yoonjin Lee for introducing me a whole new world of hobbies and lifestyles; Dr. Christina McCluskey and Andrew Wagoner for their powerful and contagious positivity; Dr. Yoo-Jeong Noh for being a supportive roommate with delicious food and thoughtful words; Dr. Heeje Cho, Ahreum Lee, and Boram Kim for being all ears for me from South Korea; and Sunmi

Jin for sharing exciting stories from her world travels. Lastly, Alex Sokolowsky has been an extraordinary and bottomless source of goofiness, positivity, and creativity. Alex and his family have showered me with love and laughter. Thank you all for making me feel safe and okay to be myself.

My parents and my brother have served as members of a lifelong team effort, family. They have supported me to the fullest extent while I pursue higher education from half a world away. One of my favorite memories with them is having gone to public libraries every weekend when I was growing up. Thank you for raising me as an enthusiastic reader and avid writer. Let's keep entertaining each other with different values, passions, and hobbies!

Finally, this work has been financially supported by the Office of Naval Research project entitled "Advancing Littoral Zone Aerosol Prediction via Holistic Studies in Regime-Dependent Flows" under Grant N00014–16–1-2040. The RAMS simulations were performed at the Navy Department of Defense Supercomputing Resource Center.

TABLE OF CONTENTS

CHAPTER 1: INTRODUCTION

1.1 Importance of sea breeze convection

Sea breeze circulations are one of the most prevalent flow regimes in tropical coastal regions. During the daytime, the horizontal differences in the diabatic heating of the air over land and sea surfaces can give rise to a significant horizontal air temperature gradient. This thermal contrast increases during the day and produces a pressure gradient at low levels in the atmosphere which drives a low-level onshore wind, defined as a sea breeze. As long as a sufficient thermal contrast exists between land and ocean surfaces and that cross-coast horizontal pressure gradients are achieved as a result, sea breeze circulations can develop. At the leading edge of sea breeze circulations, sea breeze convergence can initiate convection by lifting low-level air to the level of free convection (LFC). During the daytime, lines of clouds along the coastline evident in satellite imagery mark the inland propagation of sea breeze (Figure 1.1). A wide range of clouds can form along the sea breeze convergence, from fair-weather cumuli (Loughner et al., 2011) to heavily precipitating cumulonimbi (Song, 1984; Yuter and Houze, 1995) depending on the environment in which the sea breeze develops.

Due to its ubiquity and recurrence, sea breeze-initiated convection is the major contributor to the diurnal variability of convective activity in the tropics (Yang and Slingo, 2001; Laing et al., 2011; Wang and Sobel, 2017). Given the continual increase in the human population within coastal regions (NOAA, 2013), the associated anthropogenic activities, as well as climate change, it is imperative to understand how tropical sea breeze convection varies, both as a function of current aerosol and environmental factors, and within the different aerosol and local environments that may result as a function of climate change. Despite a variety of past sea breeze studies dedicated to investigating the primary drivers of sea breeze circulations (as discussed in more detail in 1.2), forecasting sea breeze convection remains challenging due to the significant uncertainties generated by the coexistence, covariance and interactions of the thermodynamic, microphysical, wind, aerosol and surface characteristics important to sea breeze circulations.

Figure 1.1. Aqua Moderate Resolution Imaging Spectroradiometers (MODIS) image over Sri Lanka around midday on April 9, 2013. (https://earthobservatory.nasa.gov/images/81833/fair-weather-clouds-sri-lanka)

1.2 Limitations in previous sea breeze sensitivity studies

Past studies investigating how different environmental parameters affect the sea breeze circulation have primarily focused on the zonal wind speed and land-surface heat flux (e.g., Arritt, 1993; Finkele, 1998; Molina and Chen, 2009), which affect the horizontal pressure gradient and land-sea thermal contrast. In particular, the variation in the propagation speed and inland extent as a function of these two parameters have been extensively studied (Crosman and

Horel, 2010; Igel et al., 2018). Firstly, previous studies revealed that the critical range of offshore background wind that prevents sea breezes is 6–11 m s^{-1} (Arritt, 1993). The inland propagation speed of the sea breeze front is also decreased by increasing offshore background wind (Physick, 1980). Secondly, the magnitude of land-surface sensible heat flux has been found to be the primary driver of sea breeze circulations. Higher land-surface sensible heat flux values drive greater inland penetration and faster propagation of sea breeze front (Physick, 1980; Ogawa et al., 2003; Antonelli and Rotunno, 2007). As the solar zenith angle, which determines the amount of incoming solar radiation reaching the surface, is a function of latitude, the inland penetration also depends on latitude (Rotunno, 1983). Only a few studies in the literature have examined the impacts of the multitudinous interactions between aerosols, radiation, and other environmental factors on sea breeze processes, where the focus has been on the following:

1. the effects of two-way interactive land surface processes on sea breezes (Baker et al., 2001; Miao et al., 2013; Steele et al., 2013; Grant and van den Heever, 2014; Igel et al., 2018; Rajeswari et al., 2020);
2. the response of the sea breeze to a multidimensional environmental parameter space in dry environments (Igel et al., 2018);
3. the manner in which aerosol particle interactions with microphysics and radiation affect sea breeze circulations and convection (Fan et al., 2012; Grant and van den Heever, 2014); and
4. the modulation of aerosol impacts by multiple environmental conditions (Tao et al., 2012).

The following subsections summarize the salient findings of the previous studies.

1.2.1 Two-way interactive land surface processes

Most of the previous studies examining the characteristics of the sea breeze circulation only perturbed the land-surface sensible heat flux by prescribing temporally varying but spatially homogeneous surface flux profiles (Antonelli and Rotunno, 2007; Wang and Kirshbaum, 2017; Shen et al., 2018). This is typically due to the lack of appropriate and/or fully interactive land-surface parameterizations within the models being utilized. While the land-sea thermal contrast is primarily dominated by the land-surface sensible heat flux and thus land-surface temperature, in reality, surface latent heat flux also influences surface temperature via partitioning of surface fluxes (i.e., Bowen ratio). Furthermore, when convection within sea breeze flow regimes produces precipitation, evaporative cooling can cool down the surface. Therefore, feedbacks between the land surface and atmosphere via evapotranspiration, radiation, turbulent mixing, and precipitation need to be included to represent the surface heat flux variations adequately.

1.2.2 Multidimensional parameter space

Most of the previous sea breeze sensitivity studies have applied a one-at-a-time (OAT) approach, perturbing only one parameter across a given value range while keeping all the other parameters of interest constant. Through the OAT approach, individual impacts of environmental parameters such as background wind speed have been particularly well understood. Different onshore and offshore cross-coast ambient wind velocities have been tested (Crosman and Horel, 2010). It has been found that the sea breeze does not form when the background wind is stronger than critical threshold values, which depend on the location and other environmental conditions. However, the OAT analysis cannot detect how multi-parameter interactions or feedbacks change sea breeze convection. Some previous of studies (Baker et al., 2001; Lynn et al., 2001; Darby et al., 2002; Grant and van den Heever, 2014) have considered parameter interactions in their sea breeze sensitivity experiments through the use of factor separation analysis (Stein and Alpert, 1993). While synergistic interactions among parameters have been quantified in these studies, only two or three parameters were perturbed together over a coarse parameter uncertainty space due to the large computational expense involved when multiple parameters are varied. For example, if one examines three values for each parameter, the minimum number of simulations necessary for factor separation simulations is 3^n, where n is the number of parameters of interest. Therefore, examining sea breeze sensitivity to multiple parameters over a finely resolved uncertainty parameter space is computationally infeasible when applying factor separation techniques.

In order to overcome the limitations of OAT and factor separation methods, a Bayesian statistical approach has recently been developed (Lee et al., 2011, 2013; Johnson et al., 2015). This approach employs a statistical experiment design (Santner et al., 2003), Gaussian process emulation (O'Hagan, 2006; Rasmussen and Williams, 2006), and variance-based sensitivity analysis (Saltelli et al., 2000). In particular, the Gaussian process emulation and variance-based sensitivity analysis techniques can be used to perform a Monte Carlo sampling of the sea breeze convection characteristics across the multi-dimensional parameter space and then to assess the relative importance of individual parameters as well as parameter interactions. Utilizing this approach, Igel et al. (2018) successfully quantified the sensitivity of sea breeze convection in *dry subtropical environments* to eleven different environmental parameters by describing initial conditions of idealized sea breeze simulations. While this was the first study of its kind to do so, Igel et al. (2018) focused only on the structure of the sea breeze circulation and did not examine the cloud sensitivities to environmental changes.

1.2.3 Aerosol particle interactions with microphysics and radiation

Aerosol particles may impact sea breeze convection by either (1) changing the three primary convective ingredients (Doswell, 1987)—moisture, instability, and lift—through aerosol-radiation interactions or (2) by directly changing cloud characteristics (e.g., vertical extent, albedo, buoyancy) through microphysical-dynamical feedback processes. In the first instance, aerosol particles can scatter or absorb radiation, thereby altering the thermodynamic instability and surface fluxes through the aerosol direct effect (Yu et al., 2002; Koren et al., 2004, 2008; Feingold et al., 2005; Jiang and Feingold, 2006; Zhang et al., 2008). In turn, convective ingredients, such as moisture, instability, and lift, can be altered, thus affecting the development of sea breeze convection. In the second instance, as aerosol particles can serve as cloud condensation nuclei (CCN), changes in aerosol number concentration may affect microphysical processes within clouds that form over tropical sea breeze flow regimes. Changes in latent cooling or heating associated with CCN-induced microphysical processes can affect cloud dynamics through changes in cloud buoyancy through the aerosol indirect effect (Andreae et al., 2004; Khain et al., 2005; van den Heever et al., 2006).

1.2.4 Environmental modulation of aerosol impacts

The two pathways mentioned in Section 1.2.3 may be modulated by environmental conditions (Tao et al., 2012). While we know that environments can modulate aerosol impacts on convection, this has not been explored in the context of sea breeze convection. Furthermore, there is still much to be learned about the environmental modulation of aerosols on cloud processes. To fill this gap, this dissertation research investigates aerosol impacts on sea breeze circulation and associated convection as a function of a wide range of environments and as a function of different aerosol conditions.

1.3 Dissertation outline

As the four aspects outlined above have not been extensively examined by previous studies, the primary goal of the work outlined in this dissertation is to understand the controls of tropical sea breeze convection under different environments (i.e., initial conditions) where aerosol, radiation, cloud, and land-surface interact with one another.

In Chapter 2[1], an extensive ten-dimensional environmental parameter sensitivity analysis of tropical sea breeze convection is conducted. An ensemble of 130 idealized cloud-resolving simulations is performed by simultaneously perturbing six atmospheric and four surface parameters describing the initial conditions. All idealized tropical simulations are carried out using the Regional Atmospheric Modeling System (RAMS) coupled to a two-way fully interactive land surface model. The key parameters impacting the inland characteristics and the intensity of sea breeze convection in a tropical rainforest are then identified through the application of a statistical emulation and variance-based sensitivity analysis techniques. The processes responsible for environmental controls on the sea breeze are investigated.

[1] This study, titled "Environmental Controls on Tropical Sea Breeze Convection and Resulting Aerosol Redistribution," has been published in Journal of Geophysical Research: Atmospheres (Park et al., 2020; © 2020 American Geophysical Union). Park, J. M., van den Heever, S. C., Igel, A. L., Grant, L. D., Johnson, J. S., Saleeby, S. M., Miller, S. D., and Reid, J. S. (2020). Environmental controls on tropical sea breeze convection and resulting aerosol redistribution. *Journal of Geophysical Research: Atmospheres*, 125, e2019JD031699. https://doi.org/10.1029/2019JD031699

Chapter 3[2] extends the study presented in Chapter 2 by introducing several additional simulation ensembles with different aerosol conditions. In this chapter, the manner in which microphysically and radiatively active aerosol particles influence over-land convection developing under a wide range of environments is examined, with particular focus on the modulation of aerosol direct and indirect effects within the context of sea breeze convection. The first two ensembles allow for aerosol particles to interact with both radiation and microphysics. The aerosol species considered in this study are comprised of ammonium sulfate, which primarily scatter radiation, and are only weak absorbers of radiation. These ensembles are designed to address the impacts of enhanced loading of aerosols, and as such, only differ in their initial aerosol loading, with one ensemble being representative of low aerosol loading or clean conditions, while the other is initialized with heavier aerosol loading being representative of more polluted conditions. Similar to the research presented in Chapter 2, each of these two ensembles contains 130 members initialized with 130 different initial conditions, where ten thermodynamic, wind, and surface properties are simultaneously perturbed. The next two ensembles are carried out to isolate aerosol indirect effects by eliminating the interactions between aerosol particles and radiation (i.e., the aerosol direct effect). Utilizing the 12 initial conditions that produce deep convection under clean conditions within the first ensemble described above, 24 additional simulations are performed, 12 of which are clean and 12 of which are polluted, and all of which have aerosol-radiation interactions turned off. These 4 different ensembles are then used to assess the direct and indirect impacts of aerosols on both the sea

[2] This study, titled "Environmental Modulation of Aerosol Impacts on Tropical Sea Breeze Convection" (Park and van den Heever, 2020, in preparation) is to be submitted.

breeze circulation and the associated convection, as well as the manner in which these effects are modulated by the environment in which the sea breeze develops.

Chapter 4 summarizes this dissertation research. Implications of this research for enhancing our abilities to forecast sea breeze convection are presented, and suggestions for future work are provided.

CHAPTER 2: ENVIRONENTAL CONTROLS ON TROPICAL SEA BREEZE CONVECTION AND RESULTING AEROSOL REDISTRIBUTION

2.1 Introduction

Along the coastlines, the discontinuities between radiative and thermodynamic properties of the land and the ocean regions lead to the land-sea breeze circulation (Crosman and Horel, 2010; Miller et al., 2003; Simpson, 1994). During the day, differential heating over land and ocean surfaces creates an inland-directed pressure gradient force. In response, a relatively colder, moister, and more stable marine air mass advances inland, with compensating offshore flow aloft. On the landward side, the convergence at the leading edge of the circulation induces upward motion, which supports convective cloud formation by lifting the low-level air parcels to the level of free convection.

The sea breeze can affect a wide range of human activities along the coastlines, including recreation, agriculture, transportation, naval activities, wind energy use, and industry. Given that nearly half of the world's population resides within 150 km of the coastline and that this coastal population is expected to continue increasing (United Nations Atlas of the Oceans http://www.oceansatlas.org), it is important to provide reliable forecasts of sea breeze convection and associated coastal air quality. Observations indicate that the horizontal extent of sea breezes varies from a few kilometers to several hundred kilometers inland (Clarke, 1983; Muppa et al., 2012; Physick and Smith, 1985) and from several hundred meters to a kilometer in vertical (Atkins et al., 1995; Miller et al., 2003; Thompson et al., 2007). Furthermore, as both surface and meteorological conditions vary depending on the region and time of the year, sea breeze forecasting techniques developed for a specific region do not necessarily work well in another region (Miller and Keim, 2003).

As a persistent boundary layer feature existing along the inhomogeneous land-sea interface, the sea breeze responds to and interacts with various surface properties such as soil moisture (Baker et al., 2001), surface roughness length (Kala et al., 2010), the coastline curvature (Boybeyi and Raman, 1992), and sea surface temperature (Lombardo et al., 2018; Seroka et al., 2018). Atmospheric parameters such as large-scale winds (Arritt, 1993), wind shear (Drobinski et al., 2011; Moncrieff and Liu, 1999), relative humidity (Rousseau-Rizzi et al., 2017), and low-level instability (Xian and Pielke, 1991) play important roles as well. The sea breeze can be influenced by preexisting boundary layer processes such as river breezes (Zhong et al., 1991), Rayleigh-Bénard convective thermals (Ogawa et al., 2003; Rochetin et al., 2017), horizontal convective rolls (Atkins et al., 1995; Fovell, 2005), and convective cold pool boundaries (Kingsmill, 1995; Rieck et al., 2015; Soderholm et al., 2016; Wilson and Megenhardt, 1997). Since these environmental properties and boundary layer processes covary and interact with one another in time and space, they introduce significant uncertainties both in the initial condition and prognostic fields of numerical simulations.

Although several numerical experiments have demonstrated the individual impacts of the surface and atmospheric layer properties on the sea breeze convection, only a few studies (e.g., Baker et al., 2001; Darby et al., 2002; Grant and van den Heever, 2014) have assessed both the individual influences of parameters and their interactions by perturbing two or more parameters (i.e., factor separation technique by Stein and Alpert, 1993), the uncertainty ranges of which tended to be coarse. A comprehensive assessment of the relative influences of the many environmental parameters impacting sea breezes and their synergistic interactions is scarce and hence forecasting the timing, location, and intensity of sea breeze convection remains a challenging problem that is worthy of more in-depth inquiry.

The extent and the intensity of the sea breeze have received considerable attention due to their role in the redistribution of near-surface aerosols (Blumenthal et al., 1978; Edinger and Helvey, 1961; Lu and Turco, 1994; Verma et al., 2016). Near-surface aerosols can be transported further inland and/or higher aloft through inland propagation and/or frontal uplift, respectively (Lyons et al., 1995; Thompson et al., 2007). While aerosol redistribution within the boundary layer has been studied extensively (Banta et al., 2011; Ding et al., 2004; Iwai et al., 2011; Liu et al., 2001; Loughner et al., 2014), the convective processes that may redistribute aerosols further aloft have received little attention. This is particularly true in observational studies using in situ measurements where sea breeze cases accompanying convective clouds and precipitation have been excluded from the analysis, since those signals generate substantial aerosol backscatter gradients which hinder the retrieval of boundary layer and aerosol properties (Caicedo et al., 2019). In the presence of moist sea breeze-initiated convection, aerosols in the lower troposphere may be vertically redistributed to upper tropospheric levels via cloud venting (Cotton et al., 1995). It is, therefore, necessary to identify the response of the sea breeze convection and associated aerosol redistribution via convective processes to different environmental parameters, including those that may be altered by anthropogenic activity in these already populated coastal regions.

Primarily due to the computationally intensive nature of the problem, few studies have considered the sensitivities of the sea breeze convection over a multidimensional parameter space where simultaneous parameter variations are allowed. Igel et al. (2018, hereafter IvJ18) explored this problem as part of the Holistic Analysis of Aerosols in Littoral Environments

(HAALE) team effort, an Office of Naval Research (ONR)-funded Multidisciplinary University Research Initiative (MURI). One of the primary goals of the HAALE-MURI team has been to characterize the fundamental environmental parameters that control aerosol redistribution in littoral (coastal) zones in order to aid the development of coupled data assimilation systems. IvJ18 quantified the percentage contribution of 11 environmental parameters to sea breeze characteristics and aerosol redistribution in a dry, cloud-free subtropical environment. The present study extends the work of IvJ18 by examining a moist coastal rainforest environment that supports the development of both diurnal and sea breeze-initiated convective clouds and precipitation over land.

This research seeks to answer the following questions: in a moist coastal rainforest environment, what are the key environmental parameters that control the uncertainty in (1) the inland characteristics of sea breeze; (2) the intensity of the associated tropical sea breeze convection; and (3) the potential vertical redistribution of aerosols? We address these questions with an ensemble of idealized cloud-resolving model simulations and the application of the same statistical procedure used in IvJ18. Specifically, this procedure includes statistical emulation (O'Hagan, 2006), enabling prediction of the model output responses for a large number of untried parameter combinations, thereby allowing us to efficiently investigate a wide range of multidimensional parameter relationships. Finally, the controlling environmental parameters are characterized using variance-based sensitivity analysis (Saltelli et al., 2000), which decomposes the overall variance in a model output variable into contributions from the individual parameters, as well as their interactions.

2.2 Methods

2.2.1 Choice of perturbed environmental parameters

Table 2.1. A list of the environmental parameters perturbed in this study, including the ranges selected. Adapted from IvJ18 but for a moist tropical rainforest environment. See Table 1 in IvJ18 for detailed descriptions.

Parameter	Uncertainty Range	
	This study	IvJ18
Atmospheric	Moist tropical	Arid subtropical
Inversion layer strength	1–15 K km^{-1}	
Inversion layer depth	100–1000 m	
Boundary layer potential temperature	285–300 K	
Boundary layer relative humidity	75–95 %	20–50 %
Boundary layer height	100–1000 m	
Initial wind speed	−5–5 m s^{-1}	
Surface	Rainforest	Desert
Sea-air temperature difference (SST-T_{atm})	−10–10 K	
Sea surface temperature gradient (SST Gradient)	−0.02–0.02 K km^{-1}	
Land-air temperature different (T_{land}-T_{atm})	0–10 K	
Soil saturation fraction	(0.1, 0.9) with the saturation volumetric moisture content of 0.420 m^3 m^{-3}, sandy clay loam	(0.1, 0.9) with the saturation volumetric moisture content of 0.395 m^3 m^{-3}, sandy soil

IvJ18 compiled six atmospheric and five surface characteristics that have previously been identified in the literature as important to sea breeze circulations (see Table 2.1 in IvJ18) and perturbed them to conduct the sensitivity experiments. To facilitate comparisons with IvJ18, we adopt 10 of those 11 parameters as initial conditions for each of the sea breeze simulations conducted here (Table 2.1). Each parameter has an uncertainty range, and we perturb these parameters simultaneously over their ranges to produce a perturbed parameter ensemble over the 10-dimensional parameter space. We assign to each parameter the same uncertainty range utilized in IvJ18, with the exception of the boundary layer humidity, which differs between the arid and moist environments. The latitude, which determines the Coriolis parameter and solar zenith angle, thereby affecting the timing and strength of the circulation (Rotunno, 1983), is excluded here since our focus is on tropical sea breezes.

Six atmospheric parameters are examined, and five of them are selected based on their potential impact on the moisture and instability available to the moist convection. These parameters are the thermodynamic characteristics of the boundary layer (potential temperature, relative humidity, and height) and those of the inversion layer (strength and depth). For the development of moist convection, higher values are assigned to the minimum and maximum values of the boundary layer relative humidity compared to IvJ18. The initial wind speed, which can exert strong control over sea breeze characteristics in different environments, is also considered (Crosman and Horel, 2010).

The impacts of four surface parameters are analyzed due to their potential effects on sea breeze characteristics and convective properties via the partitioning of the surface sensible and latent heat fluxes. These parameters are the sea-air temperature difference, sea surface temperature gradient, land-air temperature difference, and soil saturation fraction. Over both ocean and land surfaces, the surface temperature is varied by perturbing the temperature difference between surface temperature and the initial air temperature (i.e., initial boundary layer potential temperature) at the lowest atmospheric level. The horizontal gradient of the sea surface temperature is specified to linearly vary from the coast to further offshore with the uncertainty range of -0.02 to 0.02 K km^{-1}, based on the analysis by Reynolds et al. (2007). Soil saturation fraction is perturbed for all 11 soil levels with the same value.

2.2.2 Model configuration

The Regional Atmospheric Modeling System (RAMS) is a three-dimensional, nonhydrostatic, fully compressible cloud-resolving model that has been successfully used to investigate sea breeze in a number of prior studies (e.g., Darby et al., 2002; Freitas et al., 2006; Grant and van den Heever, 2014; IvJ18; Miao et al., 2003). A suite of three-dimensional idealized simulations of sea breezes, where the 10 environmental parameters are simultaneously perturbed, is carried out using RAMS version 6.2.08 (Cotton et al., 2003). Details of the RAMS parameter settings and grid configuration discussed below are all included in Table 2.2. The spatial resolution chosen here is fine enough to represent the detailed sea breeze structure (Crosman and Horel, 2010) while still being computationally feasible for a large ensemble approach. To ensure that a land breeze develops before dawn and a sea breeze develops during the day, thereby capturing one full diurnal cycle of the sea breeze, the model is integrated for 24 hr, beginning at 0000 local time (LT). The RAMS output responses from the regions within 250 km of the zonal borders are removed from the analysis to exclude any potential uncertainties associated with lateral boundary conditions.

RAMS is coupled to the Land-Ecosystem-Atmosphere-Feedback Version 3 (LEAF-3, Walko et al., 2000), an interactive land-surface model that is comprised of different surface vegetation types and soil classes. LEAF-3 prognoses temperature and moisture fields for 11 soil levels and the vegetation canopy. Furthermore, through the two-way interactive coupling, the land surface and atmosphere can interact via the exchanges of momentum, heat, moisture, and radiative fluxes, as well as transpiration and precipitation. For example, precipitation over land can modulate the spatial distribution of soil moisture, thereby altering the partition of surface fluxes. Then the changes in these fluxes feed back to the atmosphere and hence can impact the development of convective clouds and precipitation.

Table 2.2. RAMS model setup

Model Aspect	Setting
Grid	• 1500 (zonal) × 150 (meridional) points • $\Delta x = \Delta y = 1$ km • 57 vertical levels; model top ~ 26 km • $\Delta z = 100$ m near the surface increasing to 1 km near the model top
Integration	• 3 s time step • 24 h simulation duration beginning at 0000 local time (LT) • Sunrise at 0600 LT and sunset at 1800 LT
Surface parameterization	• Land-Ecosystem-Atmosphere-Feedback version 3 (LEAF-3, Walko et al., 2000) • Eastern half of the domain: flat ocean with fixed sea surface temperature (SST) and horizontal gradient of SST • Western half of the domain: flat land surface; evergreen broadleaf surface type (vegetation fraction = 0.90, vegetation height = 32 m, surface roughness length = 3.5 m) with sandy clay loam soil • Eleven soil levels from 0.01 m to 0.5 m below ground • Straight coastline stretching north-south at the mid-point in the zonal direction ($x = 750$ km, black dashed line in Figure 3)
Initialization	• Thermodynamic profile: horizontally homogenous • Wind profile: horizontally homogenous, oriented perpendicular to the coastline without vertical shear • Random temperature perturbations within the lowest 500 m of the domain with a maximum perturbation of 0.1 K at the surface • Aerosol profile: horizontally homogeneous and exponentially decreasing with height with a maximum concentration of 500 mg^{-1} at the surface
Boundary conditions	• Open-radiative in zonal direction • Periodic in meridional direction
Radiation parametrization	• Two-stream (Harrington, 1997), updated every 60 s
Microphysics parameterization	• Double-moment bin-emulating bulk scheme with eight hydrometeors (Meyers et al., 1997; Saleeby and Cotton, 2004; Saleeby and van den Heever, 2013; Walko et al., 1995)
Aerosol treatment	• Ammonium sulfate • Radiatively and microphysically active • Sources and sinks
Coriolis	No ($f = 0$)

We use the same surface configurations used in Grant and van den Heever (2014, hereafter GvdH14) to represent tropical rainforests such as those found in the coastal Cameroon region (Table 2.2). The surface configurations are significantly different from those used in IvJ18 (i.e., a bare desert surface type where vegetation is absent and with a surface roughness length of 0.07 m). As such, we can investigate sea breezes and convection over vegetated land surfaces in which friction and evapotranspiration can play an important role.

The initial horizontally homogeneous thermodynamic profiles for our simulations (Figure 2.1) are based on representative profiles derived for tropical coastal environments, allowing for the development of convective clouds and precipitation. Specifically, we adapt the initial thermodynamic profile used in GvdH14 (see Figure 1 of GvdH14), which is representative of equatorial Africa's summer months (June–August). Given the idealized nature of our framework, initial conditions are chosen to broadly represent moist coastal regimes, and not to represent a particular event over a tropical coastal rainforest. While utilizing the upper-tropospheric thermodynamic profile from GvdH14, we perturb the lower-tropospheric characteristics such as boundary layer potential temperature, relative humidity, and height, as well as the inversion layer strength and depth.

Within the boundary layer, whose vertical extent is determined by the initial boundary layer height, the relative humidity and potential temperature are held constant with height. The initial relative humidity is made vertically homogeneous to ensure that we never initialize a simulation with supersaturated conditions. At the top of the boundary layer, the inversion layer begins immediately, and the potential temperature is increased linearly with height within the inversion layer. Example initial thermodynamic profiles from three of the 130 simulations are shown in Figure 2.1. Random temperature perturbations, which break the homogeneity of the initial thermodynamic conditions thereby permitting the realistic development of the idealized sea breezes, are introduced to the potential temperature field.

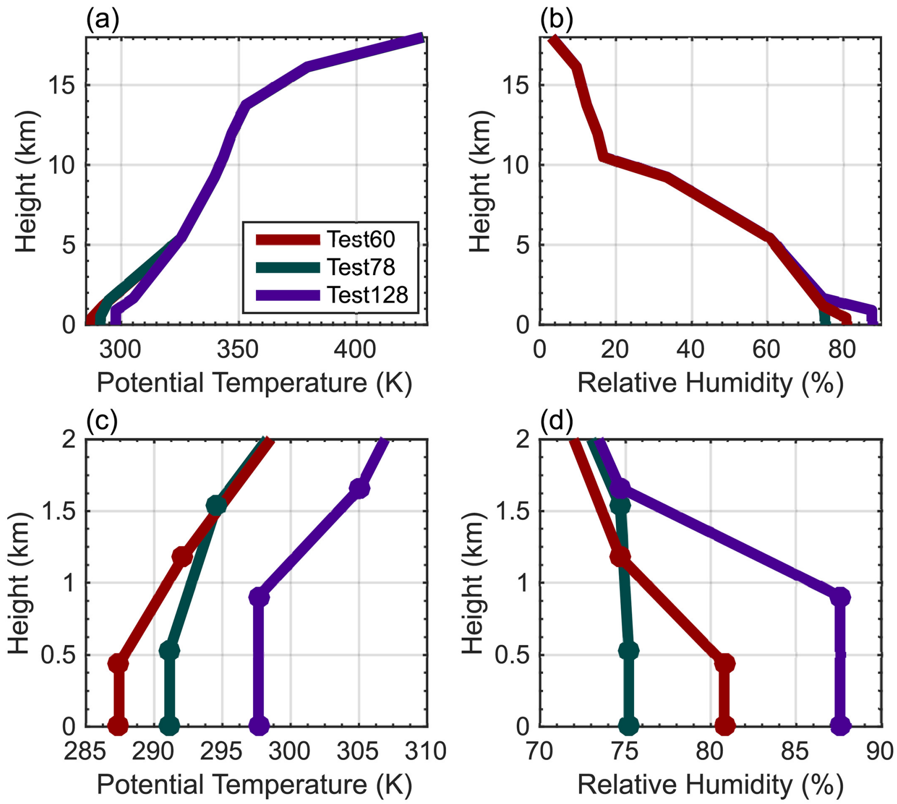

Figure 2.1. Example initial thermodynamic profiles from Tests 60 (red), 78 (green), and 128 (purple) of the 130 ensemble members: (a) Potential temperature profiles and (b) relative humidity profiles. The upper-tropospheric relative humidity and potential temperature profiles are kept identical above the inversion layer for all simulations, based on GvdH14. In the GvdH14 sounding, the relative humidity becomes less than 75% at 600 hPa, which is the minimum value over the parameter uncertainty range. At the same time, the potential temperature first exceeds 315 K, which is the maximum value for the inversion top, considering the uncertainty ranges of the parameters. Panels (c) and (d) show the lowest 2 km of panels (a) and (b), respectively. Filled circles in (c) and (d) indicate the base of the boundary layer, the base of the inversion layer, and the top of the inversion layer.

A passive tracer, serving as a proxy for the aerosol field, is introduced with concentrations identical to the initial ammonium sulfate distribution. This tracer field is not microphysically active but can be transported by the three-dimensional wind field. Therefore, the tracer field represents particles that do not serve as cloud condensation nuclei and which are not scavenged, but are vertically and horizontally transported. Hence, it allows us to take the first steps in visualizing and quantifying the dispersion and transport of aerosols while reducing the complexity introduced as a result of microphysical interactions.

2.2.3 Statistical analysis methodology

The proposed science questions are addressed through the application of a statistical procedure. This approach enables us to quantify the response of model output to individual input parameters and their interactions over the 10-dimensional parameter uncertainty space at a relatively low computational expense. This statistical framework has been successfully employed in several previous modeling studies (Lee et al., 2011, 2013; Johnson et al., 2015; IvJ18; Wellmann et al., 2018) that have assessed the relative importance of simultaneously perturbed input parameters to modeled responses. This statistical procedure is composed of three major steps (see Figure 1 of Lee et al., 2011): statistical experiment design, statistical emulation, and variance-based sensitivity analysis.

2.2.3.1 Perturbed parameter ensemble of simulations

The statistical procedure begins with the design of a perturbed parameter ensemble of simulations—a set of simulations in which the parameters are perturbed over their uncertainty ranges simultaneously to cover the multidimensional parameter uncertainty space. The selected input combinations of the parameters for each ensemble member correspond to the initial conditions of a RAMS sea breeze simulation. We utilize a space-filling algorithm called maximin Latin Hypercube sampling (Morris and Mitchell, 1995), which generates simultaneous variations of the input parameters while ensuring good coverage of the multidimensional parameter space with a minimum number of parameter combinations. We generate 130 combinations of the parameters in Table 2.1 and use them to initialize and run 130 sensitivity simulations of sea breeze convection with RAMS.

2.2.3.2 Gaussian process emulation

The next step in this approach is the construction of a statistical emulator (O'Hagan, 2006) for each of the output variables. Emulators are used to act as statistical surrogates of the RAMS simulator, where for each model output an emulator maps the relationship between the uncertain input parameters and the output response over the entire parameter uncertainty space. For each RAMS output variable of interest, we construct an emulator using the statistical software R (R Core Team, 2017) and the DiceKriging package (Roustant et al., 2012). The information from the first 100 RAMS simulations in our perturbed parameter ensemble (the "training set") is used to build an emulator. We then validate the statistical robustness of each emulator and its ability to produce a reasonable representation of the RAMS output response using the remaining 30 RAMS simulations (the "validation set"). As depicted in Figure 2.2, we compare RAMS output responses from the validation set with corresponding emulator predictions. The emulator is considered valid when at least 90% of the RAMS simulated "true" output values (values on the abscissa in Figure 2.2) lie within the 95% confidence bounds of the corresponding emulator prediction (values on the ordinate in Figure 2.2), and these values follow along the line of equality (solid black lines in Figure 2.2).

Emulators for the maximum inland extent of the sea breeze front (Figure 2.2a) and the median updraft speed (Figure 2.2e) satisfy the validation criteria very well. For the sea breeze acceleration (Figure 2.2b) and the maximum mixed layer depth (Figure 2.2c), the emulator predictions are noisier but still capture the overall signal and following the line-of-equality reasonably well. When there is a sharp regime shift that leads to substantial variability in the output over an area of parameter space, the constructed emulator can struggle to capture the model response. For example, as shown in Figures 2.2d and 2.2f (the maximum updraft speed and maximum tracer perturbation height, respectively), the validation data set looks acceptable at all points except those highlighted in red. These outliers are associated with the sharp convective behavior changes that occur when the initial boundary layer potential temperature is at the upper end of its range (~298 K). In these cases, we do not sample from the emulator where the emulator prediction is vastly underestimating the model output, and hence the contribution to output variance from the initial boundary layer potential temperature is likely underestimated for them.

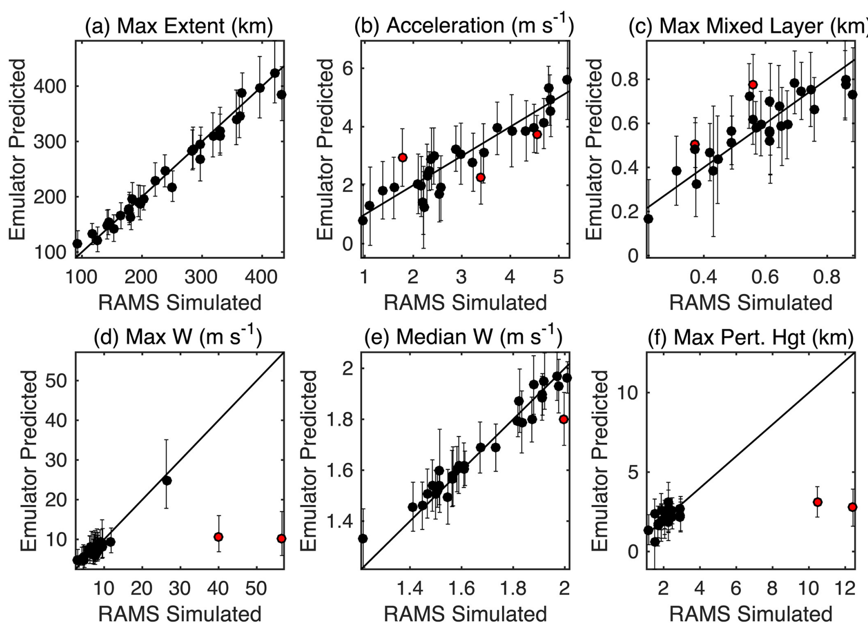

Figure 2.2. Emulator validation for six outputs of interest: (a) maximum inland extent, (b) sea breeze acceleration, (c) maximum mixed-layer depth, (d) maximum updraft speed, (e) median updraft speed, and (f) maximum tracer perturbation height. For each RAMS model output of interest, the values explicitly simulated from 30 reserved RAMS simulations out of the ensemble (x axis) are plotted against that predicted by the emulator (y axis). The error bars are 95% confidence bounds on the emulator predictions. The solid line is the 1:1 line of agreement. Outliers are marked in red.

2.2.3.3 Variance-based sensitivity analysis

Finally, variance-based sensitivity analysis (Saltelli et al., 2000) is performed to decompose the overall variance in a given RAMS output variable into contributions from individual parameters and their interactions. Utilizing the validated emulators, we sample the model output response across the 10-dimensional parameter space. We then compute the variance decomposition measures using the extended-Fourier Amplitude Sensitivity Test method (Saltelli et al., 1999) in the R package "sensitivity" (Pujol et al., 2013).

2.3 Results

2.3.1 Overview of the sea breeze characteristics and convective morphology

As the extent and intensity of sea breeze convection are different among the 130 simulations, a summary of the sea breeze characteristics and the convective morphologies is given here.

2.3.1.1 Inland propagation characteristics

First, we consider the characteristics of the inland propagation of the sea breeze. In all of the 130 simulations in our ensemble, sea breeze convergence develops, and the inland propagation of each sea breeze front is objectively identified every 10 min using the identification algorithm developed by IvJ18. This algorithm uses the meridionally averaged surface fields of potential temperature and zonal wind speed to track the sea breeze convergence (see Appendix A in IvJ18 for further details).

An example of the identified inland location of the sea breeze front is shown in Figure 2.3a on the Hovmöller diagram of the meridionally averaged surface zonal wind speed.

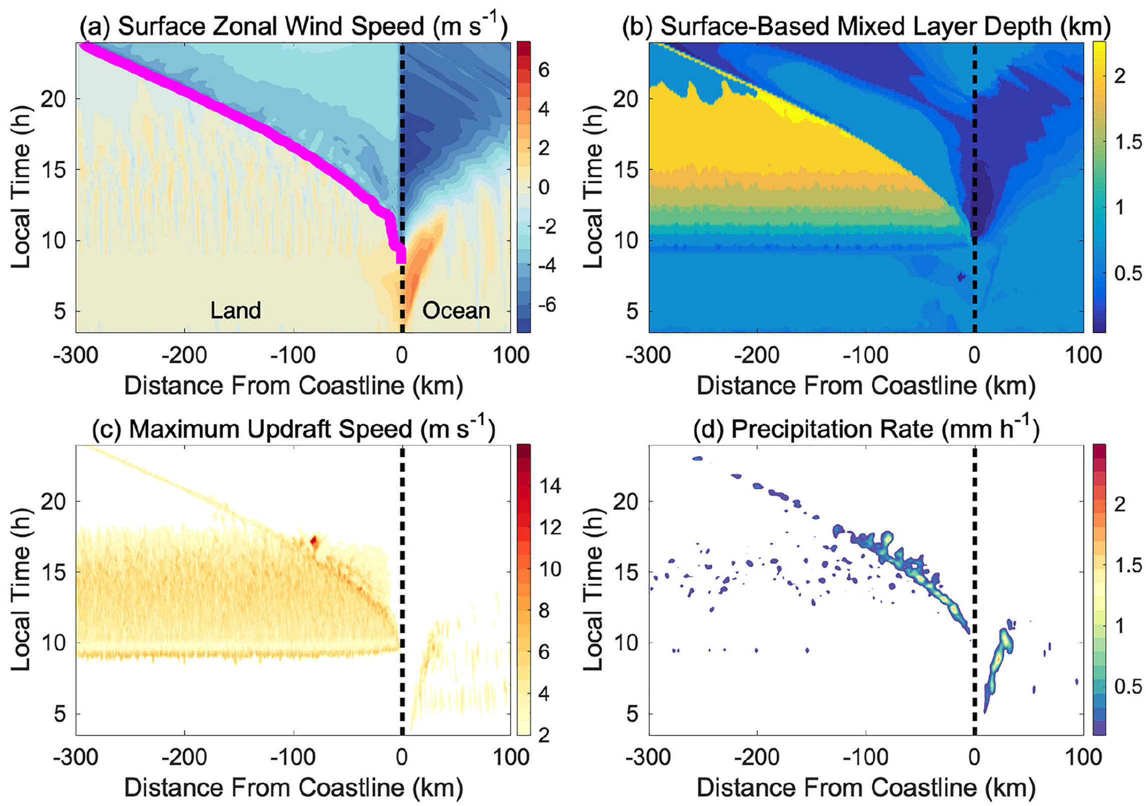

Figure 2.3. Hovmöller diagrams of (a) meridionally averaged surface zonal wind speed (m s^{-1}), (b) surface-based mixed layer depth (km), (c) maximum updraft speed (m s^{-1}), and (d) meridionally averaged precipitation rate (mm hr^{-1}) from Test 37. These figures demonstrate an example of the tracked evolution of the sea breeze front in this case. The land is on the left side of the domain and the ocean is on the right side, and as such the sea breeze front advances to the left (westward) as time advances upward on the ordinate. The magenta line denotes the horizontal location of a sea breeze front objectively identified every 10 simulation minutes. The black dashed line at $x = 0$ km denotes the forest-ocean border. Only a portion of the grid domain is shown.

We define the time when the algorithm first identifies the sea breeze front as the onset of the sea breeze for all simulations. The last algorithm-identified location represents the maximum inland penetration distance of the sea breeze front, and consequently, the maximum distance that the near-surface pollutants can be horizontally advected over land through the dynamics of the sea breeze. The ensemble-mean of the maximum inland extent is 243.8 km with a standard deviation of 84.6 km, which indicates that there is a considerable amount of variation in the sea breeze evolution across the ensemble. The range of the maximum inland extent in the simulations is within the range of previously observed moist tropical sea breeze extents, as discussed above (Clarke, 1983; Muppa et al., 2012; Physick and Smith, 1985).

It is known that sea breezes propagate slower during the daytime than at night since the turbulence ahead of the front associated with the daytime surface heating and convection acts as a drag, slowing the inland propagation of the sea breeze (Physick and Smith, 1985; Reible et al., 1993; Simpson et al., 1977). The speed of the inland penetration thus decreases in the afternoon due to the enhanced turbulent mixing and increases after sunset due to the decreased turbulence (Tijm et al., 1999). As in IvJ18, we define the daytime propagation speed by dividing the inland location of the sea breeze front at sunset by the total time that the sea breeze has existed from onset to sunset ($\frac{\text{inland extent at 1800 LT}}{\text{1800 LT}-\text{onset}}$). The nighttime propagation speed is computed as the final location of the sea breeze front divided by the time interval from sunset to the final time that sea breeze is identifiable. In all simulations, the daytime propagation speed is less than the nighttime propagation speed. The ensemble-mean ± standard deviation daytime and nighttime propagation speeds are computed as 3.3 ± 1.3 and 6.2 ± 2.0 m s^{-1}, respectively. We took the difference between the nighttime and the daytime propagation speed of the sea breeze front as a proxy of the sea breeze acceleration and examine this metric to demonstrate the impact of daytime turbulence on the sea breeze propagation.

The inland advection of a relatively cold and stable marine air mass suppresses the development of the convective mixed layer over land within the air mass, as shown in Figure 2.3b, demonstrating lower surface-based mixed layer depths behind the sea breeze front compared to that ahead of the front. The maximum depth of this suppressed mixed layer behind the sea breeze front is also analyzed to describe the stability of the air mass adjacent to the sea breeze front, which can potentially impact the frontogenesis/frontolysis. Surface-based mixed layer depth is identified using the meridionally averaged potential temperature field at each model output time and is defined as the height above the surface at which the vertical potential temperature gradient first exceeds 2 K km^{-1} (IvJ18). The diurnal variations in the mixed-layer depth are well captured with a 2 K km^{-1} threshold, and while other threshold values were tested, they did not qualitatively change the results.

2.3.1.2 Convective characteristics

We now examine the characteristics of the convection developing over land during the daytime (from onset to sunset) along and ahead of the sea breeze. At the sea breeze front, the sea breeze convergence induces vertical lifting, one of the key ingredients for moist convection (Doswell, 1987). An example of a Hovmöller diagram of maximum updraft speeds from one of the ensemble members clearly shows the most vigorous updrafts along the front (Figure 2.3c). For the same simulation, a Hovmöller diagram of the meridionally averaged precipitation rate is presented in Figure 2.3d, illustrating that the heaviest rainfall is also localized along the sea breeze front, while lighter rainfall associated with the daytime boundary layer convection occurs ahead of the sea breeze front.

Figure 2.4a displays the frequency distributions of the low (< 4 km), middle (4–7 km), and high (> 7 km) clouds for each simulation based on the cloud top height. We define the cloud top height in each column as the highest height at which the total condensate exceeds 0.1 g kg^{-1}. Lower thresholds are not used to avoid capturing the top of cirrus clouds. The neighboring columns are checked as well for the presence of condensate. In the majority of simulations, the percentage occurrence of the low clouds (gray bars) significantly exceeds that of the middle (cyan bars) or high clouds (magenta bars), which indicates the dominance of the low cloud

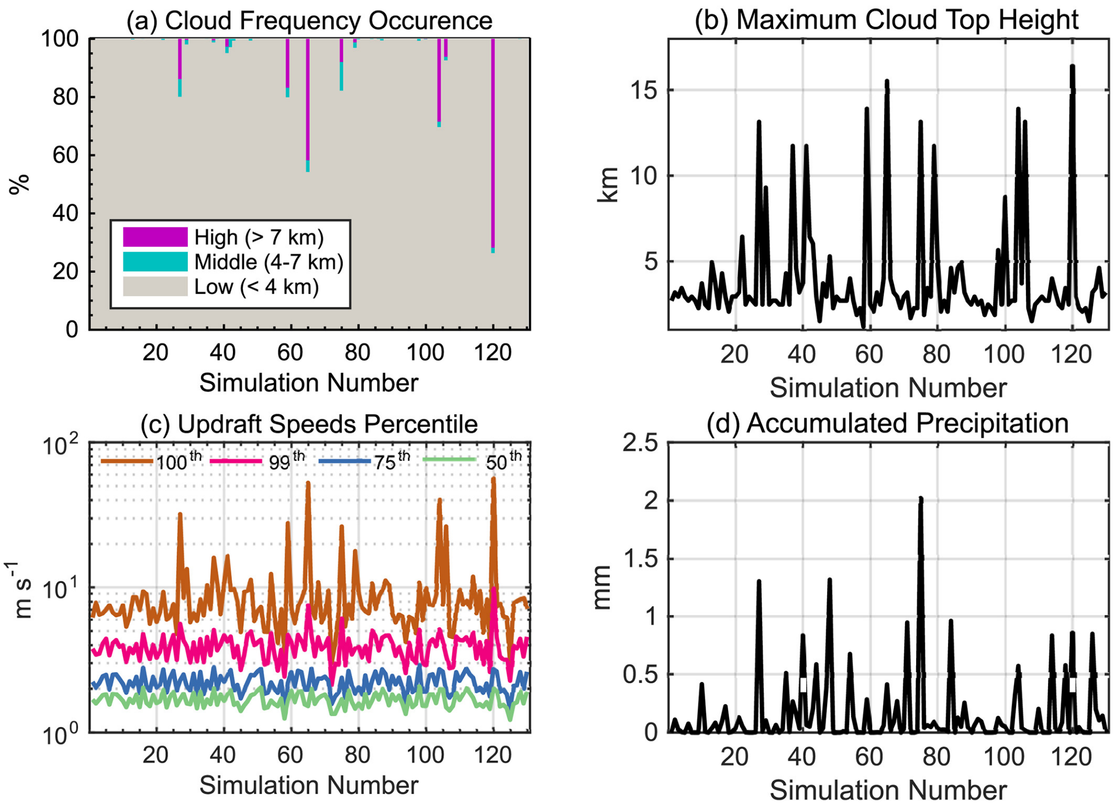

Figure 2.4. Summary of convective morphologies during the daytime over the land region: (a) cumulative frequency of occurrence (%) of low (< 4 km, gray bars), middle (4–7 km, cyan bars), and high (> 7 km, magenta bars) clouds where the sum of these three make 100%; (b) maximum cloud top height (km); (c) percentiles of updraft velocity for all grid points where the vertical velocity is greater than or equal to 1.0 m s^{-1} (log-scaled); and (d) land-averaged accumulated surface precipitation at sunset.

regime. No middle and high clouds develop in 104 out of 130 simulations, and thus the maximum cloud top height of these simulations is lower than 4 km (Figure 2.4b). In 12 of the 130 simulations, the frequency occurrence of high clouds is greater than zero, and these simulations are also marked with maximum cloud top heights greater than 7 km (Figure 2.4b).

Figure 2.4c shows the different percentiles of updraft speeds greater than or equal to 1 m s^{-1}. The sensitivity of different percentiles to different updraft speed thresholds was evaluated and did not qualitatively change the results. The peaks in the maximum updraft speed correspond with those peaks evident in the simulations with high clouds. For the 50th–99th percentiles, the updraft speeds do not exceed 10 m s^{-1} in any of the simulations (Figure 2.4c). While the updraft speeds and cloud top heights show a close correspondence, the land-averaged accumulated precipitation does not always match those peaks in cloud top height or updraft maxima (Figure 2.4d). Furthermore, the land-averaged accumulate precipitation is lower than 0.1 mm in 94 out of 130 simulations. As such, there is no distinct relationship between individual input parameters and land-averaged accumulate precipitation revealed from pairwise scatter plots (not shown), and the emulator approach is not applicable.

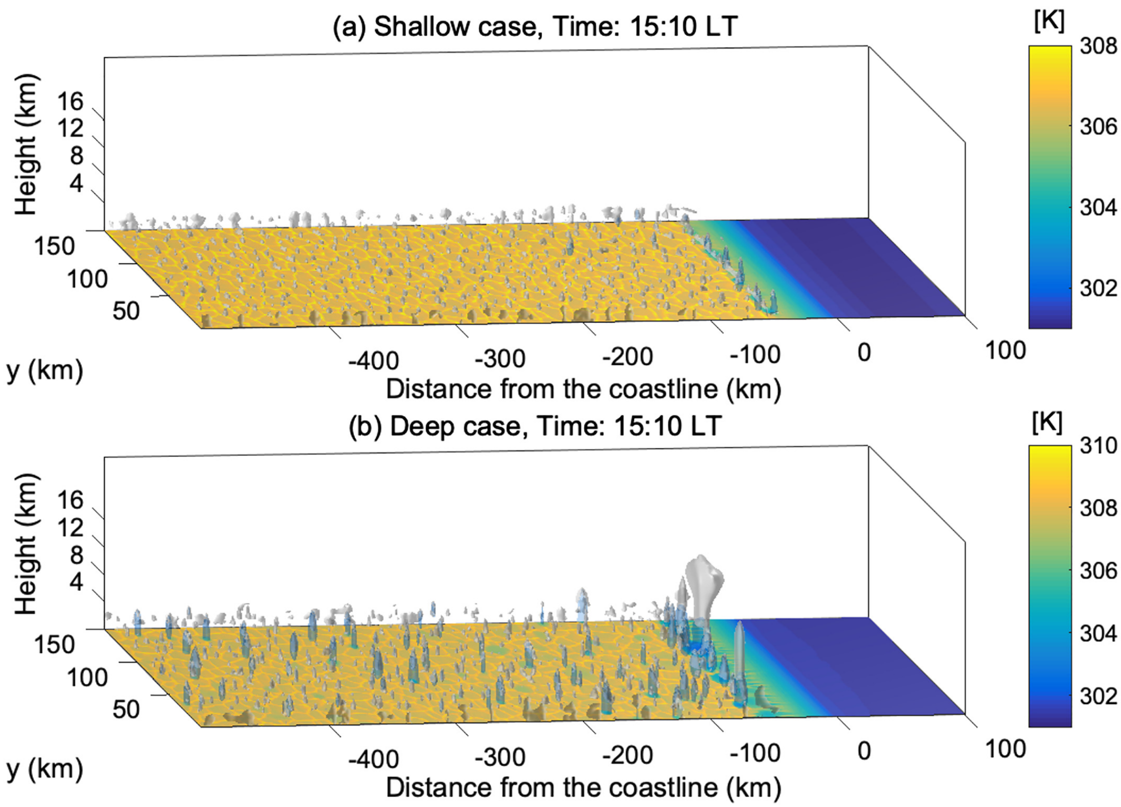

Figure 2.5. Example convective morphologies from a simulation where sea breeze-initiated convection is (a) shallow (Test 80) and (b) deep (Test 59) at 15:10 LT. White isosurfaces are where total condensate except for rain is 0.1 g kg^{-1}, and blue isosurfaces are where rain mixing ratio is 0.1 g kg^{-1}. Shaded contours are the density potential temperature (K, Emanuel, 1994) at the surface.

A graphical example of the convective morphologies that develop is illustrated in the three-dimensional condensate fields in Figure 2.5. Two examples are chosen here to illustrate two cases where the sea breeze-initiated convection is shallow (Figure 2.5a) and deep

(Figure 2.5b), respectively. In both cases, the deepest clouds and heaviest precipitation are collocated and localized along the sea breeze convergence. However, in the shallow case (Figure 2.5a), shallow clouds are prevalent over land, both ahead of and along the sea breeze front, and only the latter clouds produce precipitation. In the deep case (Figure 2.5b), the sea breeze-initiated deep convective development and anvils are evident. Moreover, boundary layer convection marked by shallow clouds ahead of the sea breeze front also produce precipitation in this deep case.

Altogether, in our ensemble, daytime boundary layer convection producing relatively lower clouds, weaker updrafts, and weaker precipitation are prevalent over land, particularly ahead of the sea breeze. In contrast, the stronger convection accompanying the highest cloud tops, strongest updrafts, and heavier precipitation is focused along the sea breeze convergence. Even though the boundary layer convection is not directly linked to the sea breeze convergence, they have a potential impact on the preconditioning of the sea breeze-initiated convection, via boundary layer mixing (Fankhauser et al., 1995), cumulus formation (Waite and Khouider, 2010), and cold pool development (Wilson and Megenhardt, 1997).

2.3.2 Sensitivity analysis: inland propagation characteristics of the sea breeze

In this section, the sensitivity of the inland extent of the sea breeze is demonstrated. In particular, to facilitate direct comparison with the IvJ18 study, the same three model outputs are examined: (1) the maximum inland extent of the sea breeze, (2) the sea breeze acceleration, and (3) the maximum mixed layer depth behind the sea breeze.

Throughout the following sections, the variance-based sensitivity analysis results are presented as stacked, color-coded bar graphs to demonstrate the relative contributions of the 10

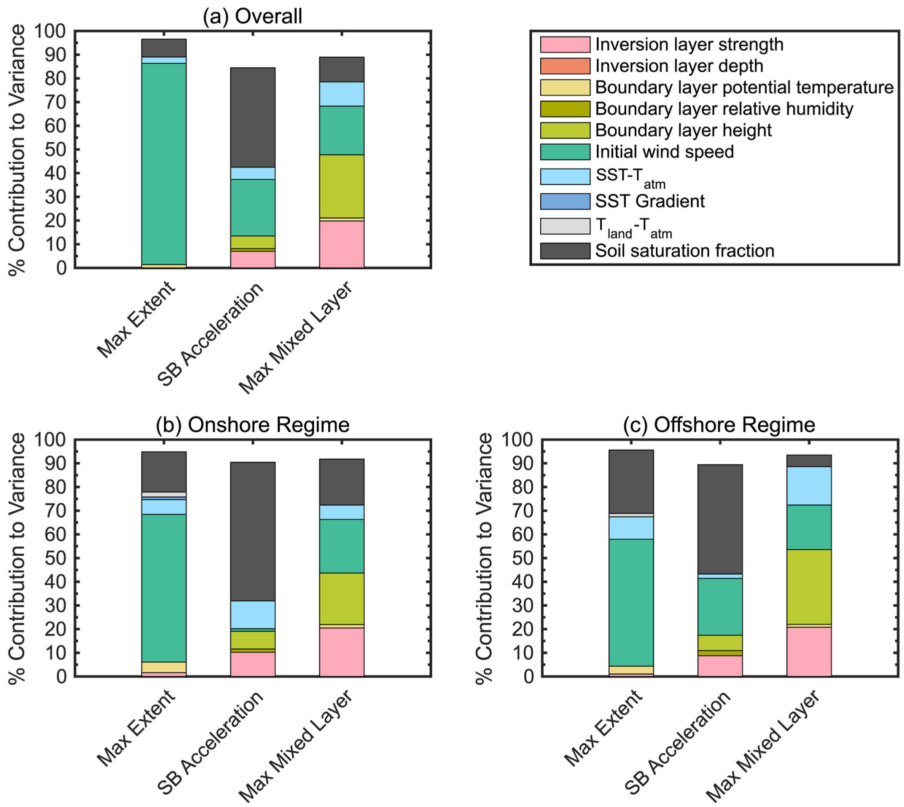

Figure 2.6. Percentage contribution to the variance of maximum sea breeze inland extent (left stacked bar), nighttime minus daytime propagation speed (middle stacked bar), and the maximum surface-based mixed layer depth behind the sea breeze front (right stacked bar) caused by each of the 10 parameters of interest over (a) the entire uncertainty parameter space, (b) the onshore regime only (initial wind speeds ≤ 0 m s^{-1}), and (c) the offshore regime only (initial wind speeds ≥ 0 m s^{-1}). Only those parameters which contribute to at least 1% of the variance are indicated. The height of each stacked bar indicates the summation of individual contributions to the output uncertainty from the 10 parameters. If the height is less than 100% this means that there are further contributions to the parameter variance arising from interactions among the parameters.

environmental parameters to the variance in the output parameter being examined (see the legend in Figure 2.6). In order to understand how the dominant parameters drive the changes in the output response, the mean response of each output to the environmental parameters that contribute 5% or more to the output variance is demonstrated.

Over the 10-dimensional parameter uncertainty range here, for each fixed value of a given parameter, we make 500 emulator predictions. A set of 500 response surfaces records the predicted output at each of these combinations for each response surface. An average of this large set of output data is then taken to determine the mean response.

2.3.2.1 Maximum inland extent

Initial wind speed dominates the variance in the maximum inland extent of the sea breeze front, explaining 85% thereof (Figure 2.6a). The mean response of the maximum inland extent to the initial wind speed (Figure 2.7a) shows that the sea breeze front propagates further inland when the initial wind is onshore (negative values), and vice versa. This response agrees with many previous studies, thus demonstrating the intuitive notion that strong offshore ambient flow inhibits the inland propagation of the sea breeze front (Arritt, 1993; Finkele, 1998; Porson et al., 2007; IvJ18). At the same time, when the ambient flow is offshore, it enhances convergence at the sea breeze front supporting frontogenesis (Reible et al., 1993).

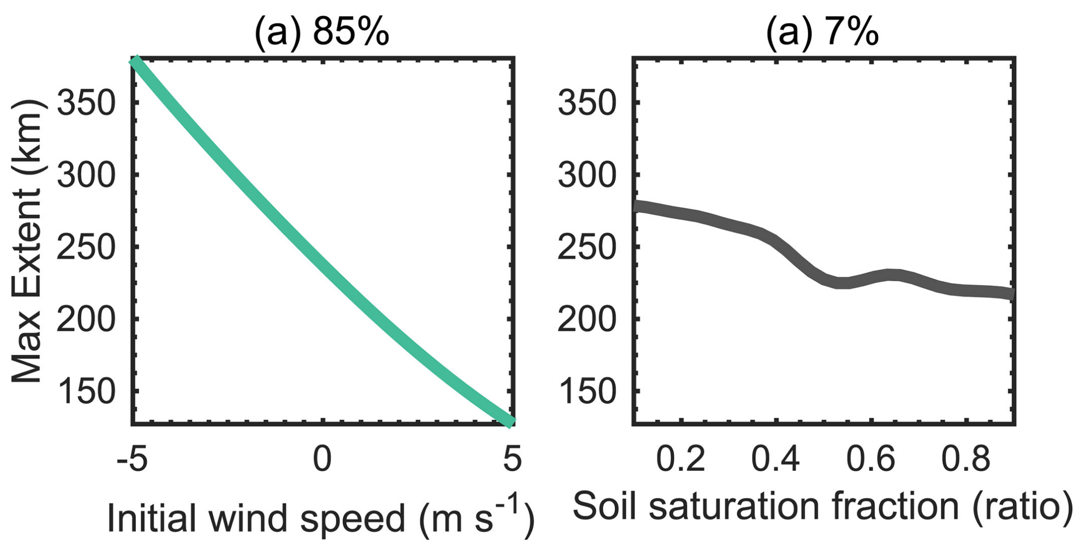

Figure 2.7. Mean responses of the maximum sea breeze inland extent to the parameters that contribute 5% or more to the output variance: (a) initial wind speed and (b) soil saturation fraction. Numbers at the top of each plot indicate the percentage contribution of each parameter to the output variance.

Soil saturation fraction is the second-most-important parameter contributing to the variance in the maximum inland penetration of the sea breeze front (7%, Figure 2.6a). The sea breeze front propagates further inland in drier soil conditions (Figure 2.7b). When the soil is drier, the sensible heat fluxes over the land surface are enhanced while the latent heat fluxes are reduced due to less evapotranspiration. As a result, the land surface temperature increases in drier conditions, and hence, the horizontal temperature gradient between the land and ocean regions, which is the primary driver of the sea breeze formation and propagation, increases as well. The variance-based sensitivity analysis for the maximum horizontal temperature gradient (not shown) also identifies the soil saturation fraction as being the most influential parameter in determining the maximum thermal gradient.

In IvJ18, the initial wind speed is also found to be the key parameter in determining the maximum sea breeze inland extent, accounting for 75% of the variance. Soil saturation fraction and sea-air temperature difference are also found to be important, contributing 13% and 7% to the output variance, respectively. While initial wind speed and soil saturation fraction are identified as being critical in our analysis as well, the influence of the sea-air temperature difference on the maximum inland extent is not found to be significant here. Overall, the relative importance of surface parameters (i.e., soil saturation and sea-air temperature difference) on the inland extent is greater in IvJ18 than in this study.

We hypothesize here as to why surface parameters are relatively more important for the maximum inland extent in a dry environment than in the moist environment. In the moist environment, shallow boundary layer clouds form over both land and ocean via boundary layer mixing, thereby reducing the incoming shortwave radiation absorbed at the surface. Additionally, surface vegetation, which is absent in IvJ18, responds to the incoming shortwave radiation via evapotranspiration. In other words, the land surface is more effectively heated in an arid desert environment, thereby directly determining the ocean-land thermal contrast. Therefore, the surface properties more directly influence the development and propagation of the incipient sea breeze front in the dry environment compared to the moist environment, where a number of other parameters modulate the role of the surface parameters.

2.3.2.2 Sea breeze acceleration

For the sea breeze acceleration, the key parameters vary between the analysis over the full parameter uncertainty space (Figure 2.6a) and the analysis over two different wind regimes (Figures 2.6b and 2.6c). These wind regimes are defined based on the uncertainty range of the initial wind speed: −5 to 0 m s^{-1} corresponds to the onshore regime, and 0 to 5 m s^{-1} corresponds to the offshore regime. While key parameters for the maximum inland extent and the maximum mixed layer depth (see Section 2.3.2.3) do not change as a function of the two wind regimes, the contribution of the initial wind speed to the sea breeze acceleration is almost absent in the onshore regime, with the contributions from inversion layer strength and sea-air temperature difference being more important (second stacked bar graph in Figure 2.6b).

In both the onshore and offshore regimes, soil saturation fraction is found to be the most important contributor to the sea breeze acceleration uncertainty, accounting for 35% and 48% of the variance, respectively. As shown in Figures 2.8a and 2.8e, the sea breeze acceleration increases when the soil saturation fraction is lower. Under drier soil conditions, the inland sea breeze propagation is reduced during the day due to enhanced boundary layer turbulence mixing processes, which are weaker in the wetter soil conditions. After sunset, drier soil cools down faster than wetter soil, and hence the turbulence over land surface disappears quicker in drier

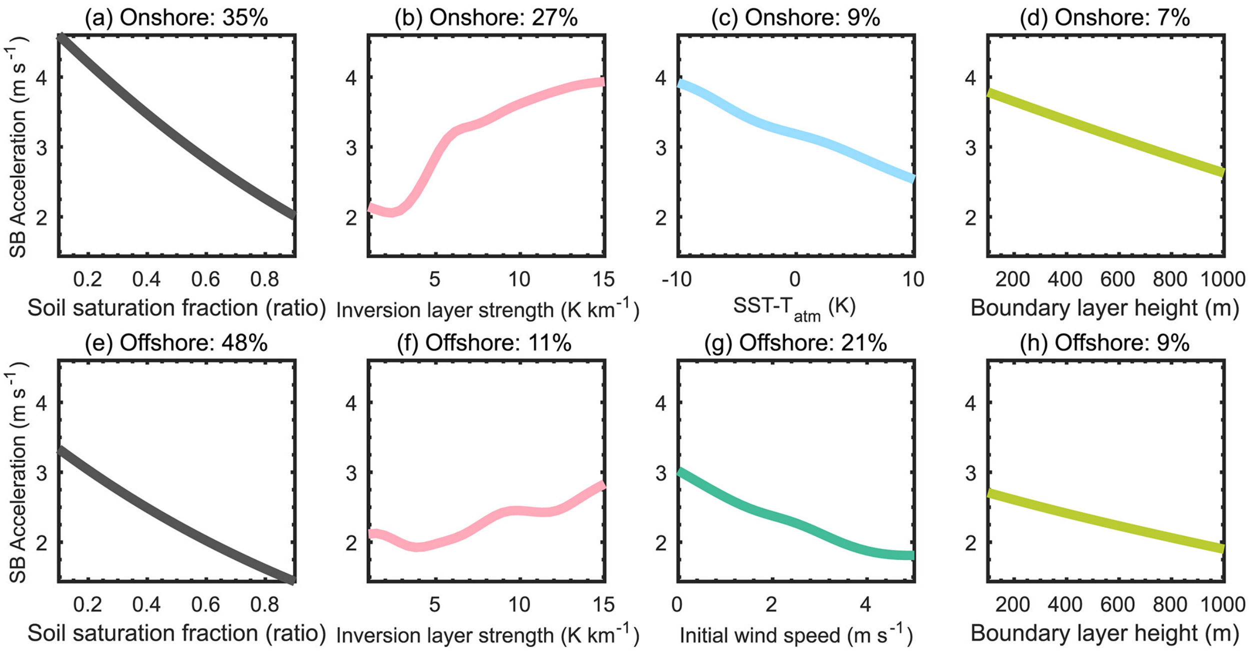

Figure 2.8. Mean responses of the sea breeze acceleration to the parameters that contribute 5% or more to the output variance in the onshore (a–d) and offshore (e–h) regimes. Numbers on the top of each plot indicate the percentage contribution of each parameter to the output variance.

soil. With less drag ahead of it, sea breeze front propagates faster in the nighttime. Therefore, the difference between the nighttime and daytime is greater in drier soil. To support this explanation, we examine the surface sensible heat fluxes over dry and wet soil simulations (Figure 2.9). Figure 2.9 shows that dry soil simulations have higher surface sensible heat fluxes (i.e., more near-surface turbulence) during the daytime than the wet simulations. Also, the surface sensible heat flux increases faster in the morning and decreases faster in the late afternoon over dry soil than wet soil, as shown by the steep slope in Figure 2.9, supporting the explanation.

Two more parameters contribute at least 5% to the variance in the sea breeze acceleration, in both the onshore and offshore regimes: inversion layer strength (27% in onshore and 11% in offshore) and boundary layer height (7% in onshore and 9% on offshore). Sea breeze acceleration increases when the inversion is stronger (Figures 2.8b and 2.8g), and the boundary layer is shallower (Figures 2.8d and 2.8h). These initial conditions are associated with shallower

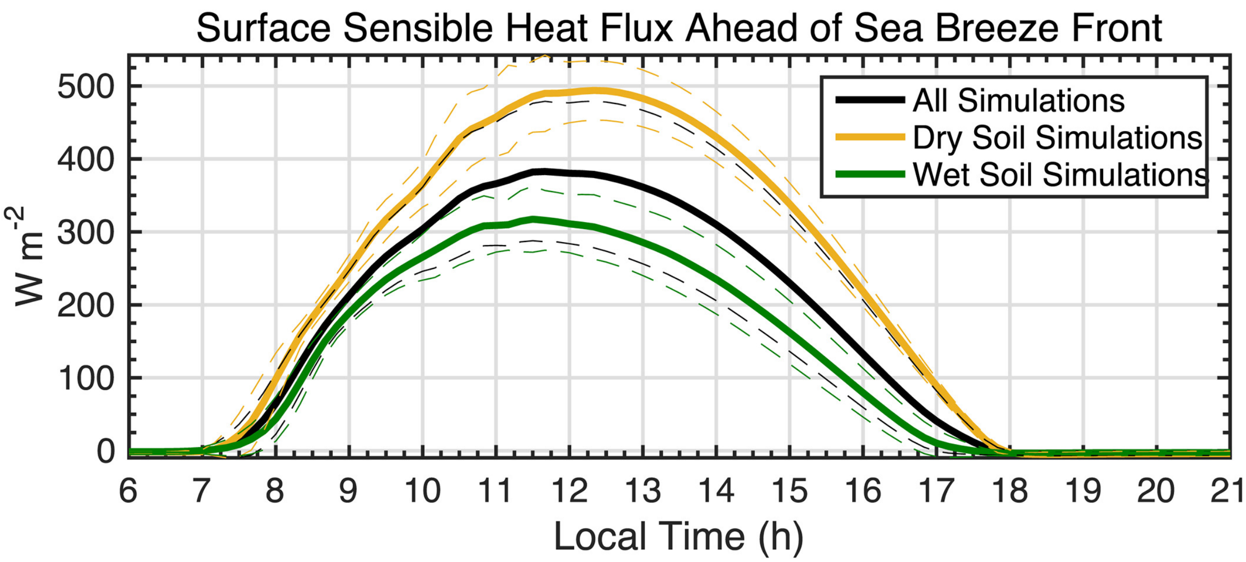

Figure 2.9. Time series of the land-averaged surface sensible heat flux (W m^{-2}) ahead of sea breeze front averaged from all simulations (black). Based on the permanent wilting point (i.e., the amount of soil moisture below which most plants will wilt and not be able to recover), simulations are separated into two groups: dry (soil saturation ratio ≤ 0.4, yellow lines) and wet (soil saturation ratio > 0.4, green lines). Dashed lines denote one standard deviation from the averaged sensible heat flux.

mixed layers over land during the daytime (see Section 2.3.2.3 for behind the sea breeze front), which indicate increases in the static stability of the air adjacent to the sea breeze front. The enhanced static stability inhibits the entrainment of the ambient environmental air into the sea breeze front. This entrainment can perturb the sharp gradient between the land and ocean air masses and reduce the thermal gradient across the sea breeze front during the daytime. Finally, the enhanced thermal gradient will result in the sea breeze propagating faster, especially at nighttime, when there is less drag from surface heat fluxes and convection.

In the onshore regime, the sea-air temperature difference is also a significant parameter, contributing 9% to the variance of the acceleration. In other words, the impact of the marine air mass that is advected inland along the sea breeze front is relatively more important in the onshore regime than the offshore regime. Figure 2.8c demonstrates that sea breeze acceleration increases when the sea surface temperature is colder than the initial air temperature at the lowest model level, and vice versa. Relatively warm ocean temperatures support deeper mixing (Figure 2.10e) and vice versa. Therefore, the mean response (Figure 2.8c) can be related to the mean responses of the inversion layer strength and boundary layer height: suppressed development of the mixed layer behind the sea breeze front (see Section 2.3.2.3) produces a greater thermal gradient between the land and ocean which results in the faster propagation of the sea breeze in the evening.

In the offshore regime, the sea breeze acceleration decreases when the offshore wind is stronger (Figure 2.8f). This response can be related to the "stagnation" of the sea breeze (Banta et al., 1993; Estoque, 1962). It appears that due to the stagnation effect in the stronger offshore wind flow, the difference between the nighttime and the daytime propagation speed is less notable compared to weaker offshore flow. The lower values in the mean responses of the sea breeze acceleration predicted over the offshore regime compared to the onshore regime also support this explanation.

In IvJ18, the initial wind speed, soil saturation, sea-air temperature difference, and Coriolis parameters were all found to be important for the sea breeze acceleration. The additional parameters of inversion layer strength and boundary layer height revealed in the moist regime can be explained as follows. A weaker inversion and a higher boundary layer result in stronger turbulent mixing, making the sea breeze more susceptible to entrainment and turbulence within the boundary layer.

2.3.2.3 Maximum mixed layer depth

The stacked bar graph on the right hand side in Figure 2.6a shows that there are five parameters contributing to more than 5% of the variance in the maximum mixed layer depth behind the sea breeze front: boundary layer height (30%), initial wind speed (18%), inversion layer strength (16%), soil saturation fraction (10%), and the sea-air temperature difference (10%). These contributions are similar in magnitude when the analysis is split into the onshore and offshore regimes (Figures 2.6b and 2.6c). Figure 2.10 shows that the maximum mixed layer depth behind the sea breeze front increases when the initial boundary layer is deeper, the initial wind is stronger regardless of the direction, the inversion is weaker, the soil is drier, and the sea surface is warmer than the air above it. The mean responses of the first four parameters are straightforward as they all promote deeper mixing of the boundary layer. For the sea-air temperature difference (Figure 2.10e), the warmer sea surface temperatures relative to the air above it promotes the mixing of air over the ocean, and that this deeper marine boundary layer air mass is advected inland through the inland propagation of the sea breeze.

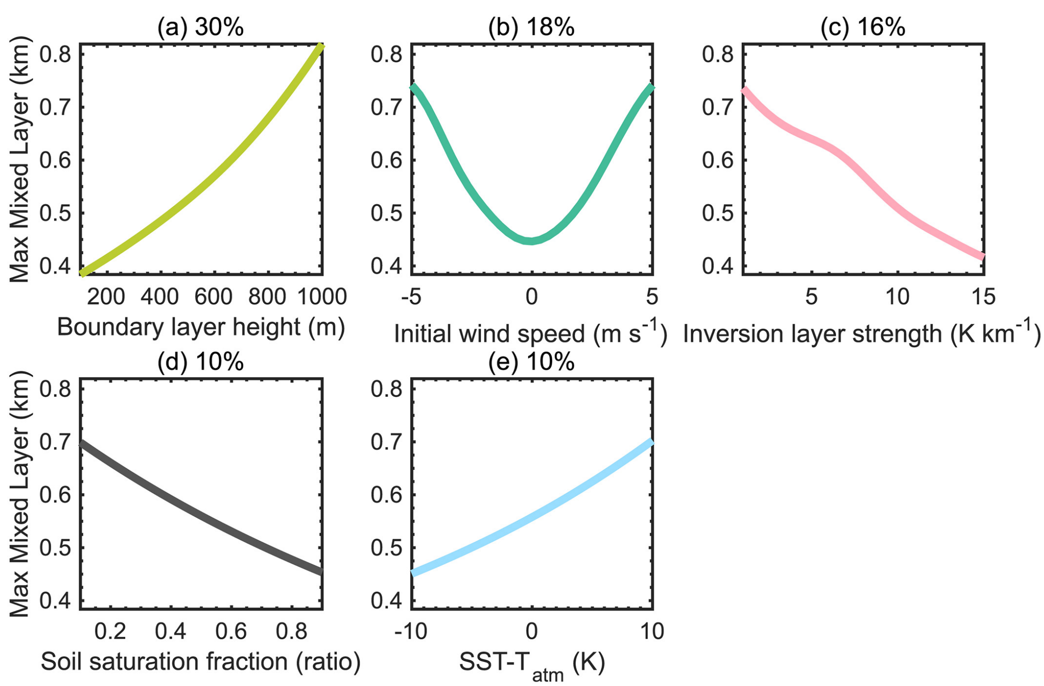

Figure 2.10. Mean responses of the maximum mixed layer depth behind the sea breeze front to the parameters that contribute 5% or more to the output variance: (a) boundary layer height, (b) initial wind speed, (c) inversion layer strength, (d) soil saturation fraction, and (e) sea-air temperature difference. Numbers on the top of each plot indicate the percentage contribution of each parameter to the output variance.

IvJ18 revealed that the initial boundary layer height, inversion layer strength, and sea-air temperature difference are the controlling parameters for the maximum mixed layer depth in an arid sea breeze regime. The mean responses of the mixed layer depth to these parameters shown by IvJ18 are in agreement with the responses shown here for a moist regime. The initial wind speed and soil saturation fraction, which can influence surface sensible heat flux and boundary layer turbulence, are also found to be dominant in our analysis, in contrast to IvJ18. It would seem that the difference between these two studies can be attributed to the presence of the vegetation canopy, which is completely absent in IvJ18. The presence of the vegetation canopy increases the mechanical production of turbulence (Melas and Kambezidis, 1992) in addition to the convective turbulence, thereby assisting in deepening the boundary layer.

2.3.3 Sensitivity analysis: convective intensity

In this section, we detail the impacts of our set of parameters on the intensity of the convection ahead of and along the sea breeze convergence, as quantified by updraft speeds. Here we look at the responses of the maximum and the median updraft speeds to represent the sensitivity of the sea breeze-initiated convection and daytime boundary layer convection, respectively.

2.3.3.1 Maximum updraft speed

Before performing the variance-based sensitivity analysis, we first explore pairwise scatterplots of the training and validation sets for all input-output combinations to see whether there is a regime shift separating shallow and deep convection. It is evident from Figures 2.11a and 2.11b that there are two convective regimes: shallow and deep regimes. The variability in the maximum updraft and the maximum cloud top height is small below the boundary layer potential temperature of 298 K, whereas there is a sharp transition from the weaker updrafts and shallow clouds to the strong updrafts and deep clouds around 298 K.

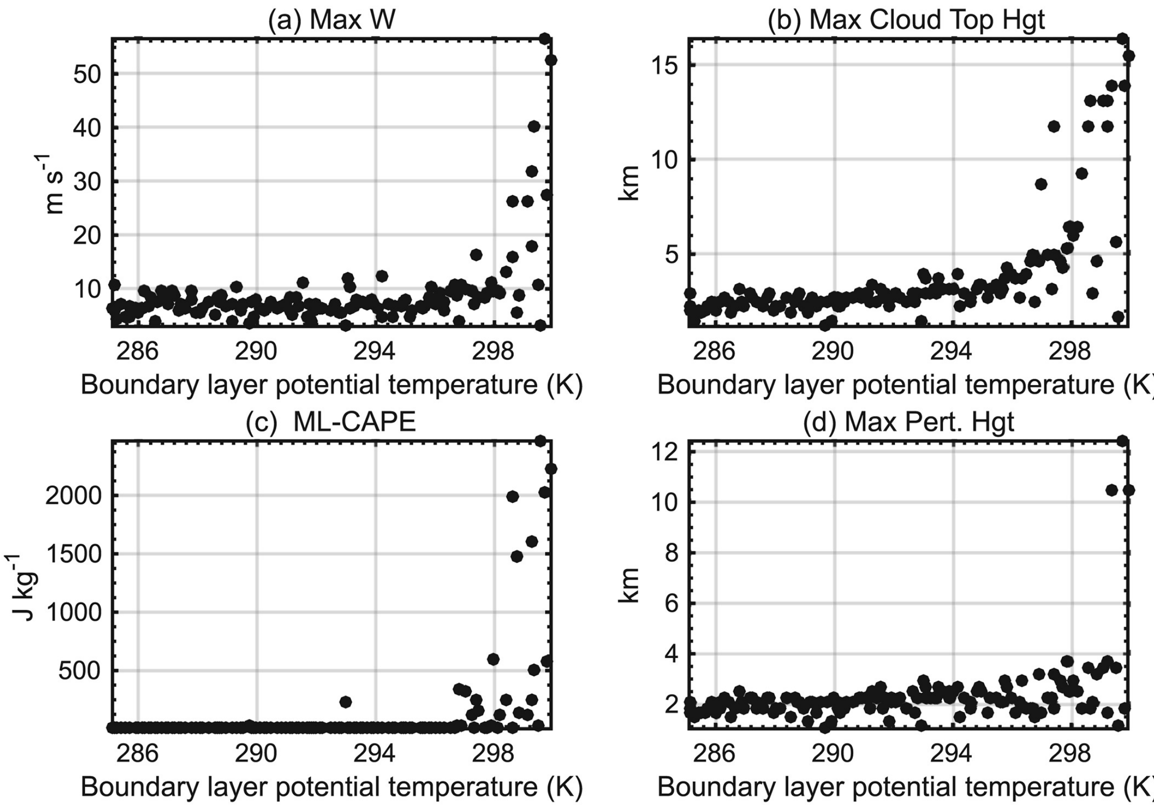

Figure 2.11. Pairwise scatterplots of the RAMS simulations for the (a) maximum updraft speed (m s^{-1}), (b) maximum cloud top height (km), (c) mixed-layer CAPE (J kg^{-1}), and (d) maximum tracer perturbation height versus the initial boundary layer potential temperature (K), showing two different convective regimes: shallow convection (< 298 K) and deep convection (298–300 K).

In the deep regime, the maximum updraft speed and the maximum cloud top height dramatically increase with the warmer boundary layer (Figures 2.11a and 2.11b). This result is not surprising given that the convective available potential energy (CAPE) is higher for the warmer boundary layer conditions in our environmental setup, all else being equal. Here we computed the mixed-layer CAPE at every output time step using spatially averaged soundings (from 10 km ahead of the sea breeze front to the western domain edge), and then temporally averaged these soundings from the sea breeze onset to sunset. Since by design the initial potential temperature profile above 5 km is identical in all of the simulations (Figure 2.1a), those simulations initialized with warmer boundary layer potential temperature have higher CAPE and are more likely to have deep convection. The pairwise scatterplot of the mixed-layer CAPE versus initial boundary layer potential temperature (Figure 2.11c) also illustrates that the CAPE behavior changes sharply for the warmer boundary layer within the strong updraft regime.

We now examine the sensitivity of the maximum updraft speed over the shallow convection regime to our 10 parameters. As stated in Section 2.2.3, we perform the variance-based sensitivity analysis for the maximum updraft speed only over the shallow regime where the emulator predictions of the model output behavior are statistically robust (i.e., 285–297 K). In Figure 2.12, the height of the stacked bar graph is 75%, which indicates that parameter interactions contribute 25% to the output variance in the maximum updraft speed over the shallow regime.

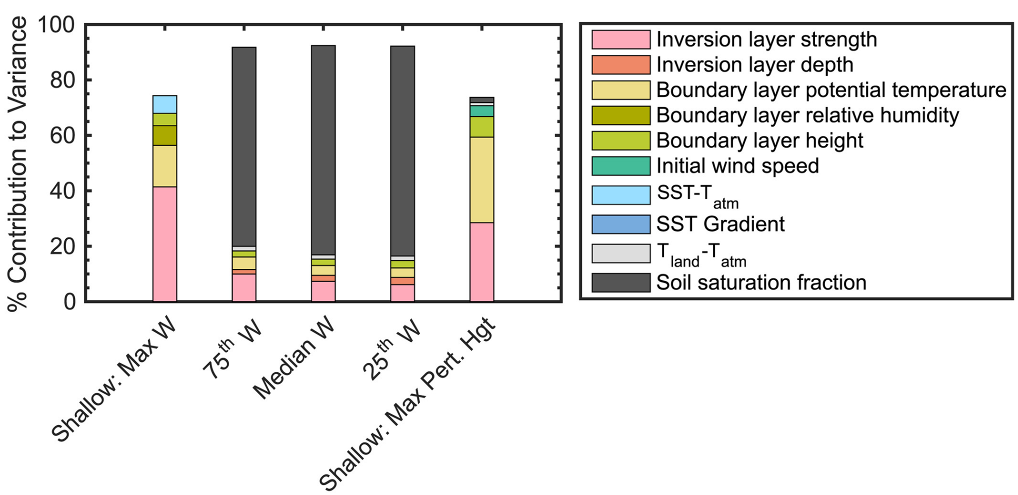

Figure 2.12. Percentage contribution to the variance by each of 10 parameters for the 100th (maximum), 75th, 50th (median), and 25th percentiles of updrafts speeds equal to or greater than 1.0 m s^{-1}, and the maximum tracer perturbation height. For maximum updraft speed and the maximum tracer perturbation height, the range of the initial boundary layer potential temperature was limited 285–297 K where the emulator approach was suitable. Only those parameters which cause at least 1% of the variance are indicated.

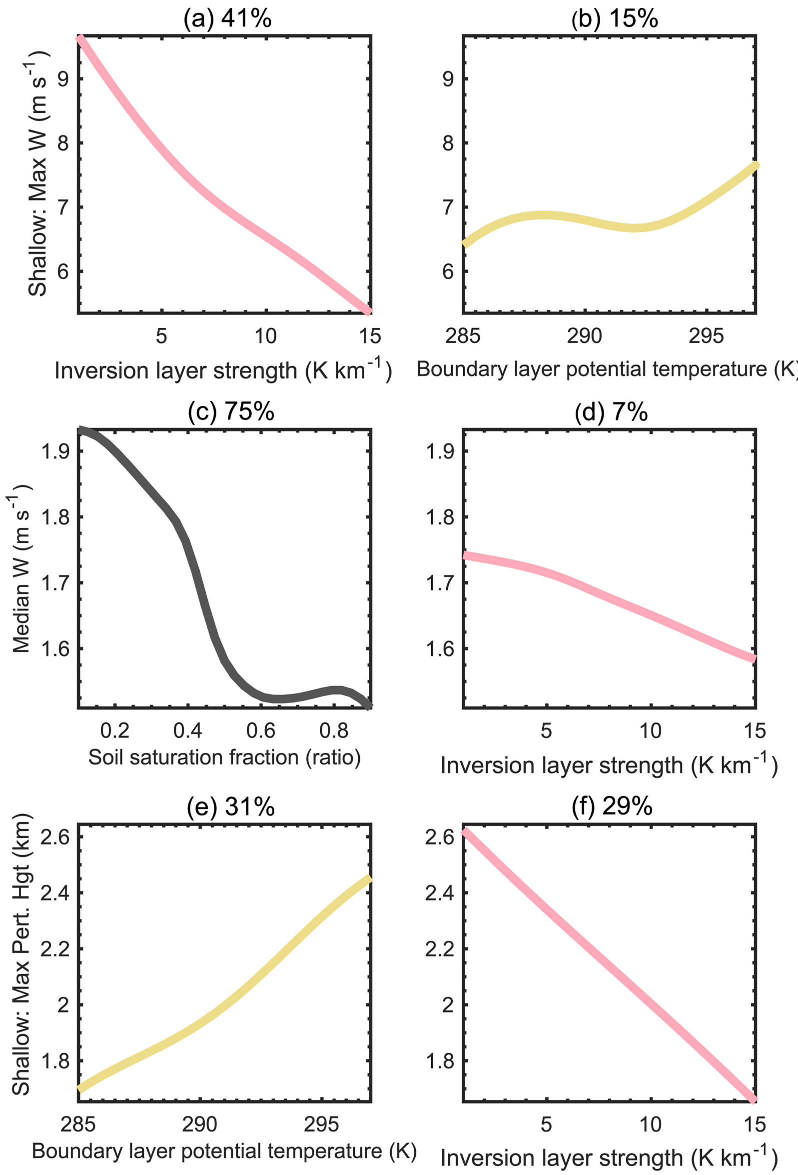

Figure 2.13. Mean responses of (a, b) the maximum updraft speed over the shallow convection regime, (c, d) median updraft speed, and (e, f) maximum tracer perturbation height to the top two parameters. Numbers at the top of each plot indicate the percentage contribution of each parameter to the output variance.

Over the shallow regime, the initial inversion layer strength is the most influential uncertainty source of the maximum updraft speed, explaining 41% of the output variance (first stacked bar graph in Figure 2.12). The emulated mean responses of the maximum updraft speeds increase when the initial inversion is weaker (Figure 2.13a), and this response is perhaps not surprising given the role of capping inversions in limiting convective activity. The pairwise scatterplot of the maximum updraft speed over the shallow regime versus the initial inversion layer strength clearly confirms that the emulator approach captures the updraft behavior over this regime (not shown).

The second-most-important parameter for the shallow regime maximum updraft speed is the initial boundary layer potential temperature, which accounts for 15% of the variance (first stacked bar graph in Figure 2.12). The warmer boundary layer favors stronger updrafts (Figure 2.13b). The warmer boundary layer enhances near-surface buoyancy and warms the near-surface air, thereby steepening the lapse rates of the lower troposphere. This enhanced low-level convective instability then can support the development of the boundary layer convection. The findings on the shallow regime are similar to those of Rousseau-Rizzi et al. (2017), who found that in a strongly inhibited environment, none of the initial parameters or the environmental conditions they considered are sufficient enough for the deep convection initiation along the mesoscale convergence line.

2.3.3.2 Median updraft speed

The height of the stacked bar graphs increase after the first one in Figure 2.12 and do not vary much, particularly from the 75th to 25th percentiles, thus indicating that parameter interactions do not play as large of a role in these updraft percentiles as in the case of the maximum updraft speeds. Moreover, the relative contributions of the parameters do not change between the median and the 25th percentiles. Therefore, we now only examine the responses of the median updraft speed to understand the sensitivity of the boundary layer convection.

For the median updraft speed, representative of the daytime boundary layer convection as discussed above, the key parameter is the soil saturation fraction, which explains 75% of the output variance, followed by the inversion layer strength which contributes 7% (third stacked bar graph in Figure 2.12). These two parameters are the most important in determining the average depth of the mixed layer ahead of the sea breeze (not shown), and hence the activity of the shallow convective mode (see Figure 2.5). The median updraft speed increases with lower soil saturation fraction and a weaker inversion (Figures 2.13c and 2.13d). Drier soil and weaker inversions promote turbulent mixing over the land during the daytime, thereby leading to stronger vertical motions in this convective mode.

2.3.4 Tracer redistribution

We now investigate the impact of the 10 environmental parameters on the convective transport of aerosol over the land. We utilize passive tracers to represent our aerosol transport and define the tracer perturbation field as the difference in the number concentration of tracers between sunset and sunrise.

Similar to Figures 2.5a and 2.5b, Figures 2.14a and 2.14b show examples of the percentage perturbation field for simulations where sea breeze-initiated convection is shallow and deep, respectively. Positive (negative) perturbations shaded with red (blue) indicate that tracer concentrations have been increased (decreased) relative to the sunrise concentration during the daytime. In both cases, negative perturbations exist near the surface with positive perturbations aloft.

The negative perturbations in both cases are stronger ahead of the sea breeze front at sunset (the location of which is shown using a pink star), where the diurnal boundary layer convection develops. During the daytime, boundary layer mixing over the land transports near-

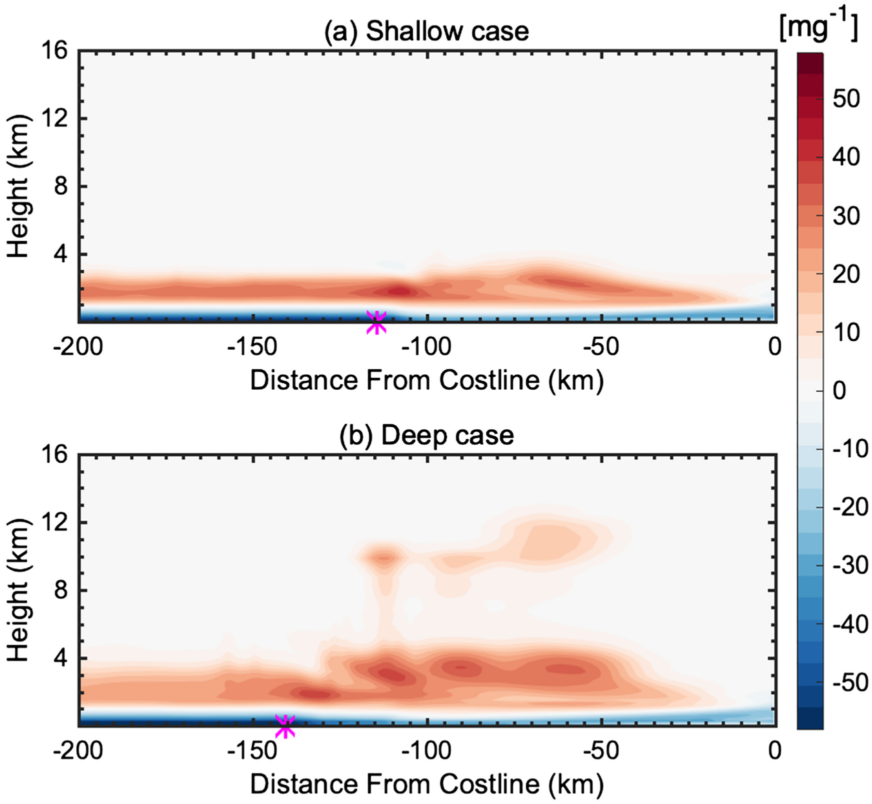

Figure 2.14. Examples of the tracer perturbation field (difference of the tracer concentration between sunset and sunrise) in a simulation where the sea breeze-initiated convection is (a) shallow (Test 80) and (b) deep (Test 59). The same simulations shown in Figure 2.5 are represented here. Pink asterisks along the *x* axis indicate the identified surface location of the sea breeze front at sunset in each case.

surface tracers to the boundary layer top, thereby producing the negative perturbation in the lower atmosphere and the positive perturbation aloft.

In the shallow case (Figure 2.14a), the positive perturbation above the boundary layer is impacted by the sea breeze front which assists in venting the aerosols out of the boundary layer, starting offshore. A similar structure has been documented in previous studies (e.g., IvJ18; Lu and Turco, 1994; Verma et al., 2006). In the deep case (Figure 2.14b), the tracers are transported further upward in the presence of the more vigorous updrafts and deeper cloud extent. As for the maximum updraft speed, the emulator predictions are poor where deep convection develops in the presence of the sharp regime shift (Figures 2.2d and 2.11a). Therefore, we conduct the variance-based sensitivity analysis for the maximum tracer perturbation height over the shallow convection regime only (i.e., uncertainty range of the initial boundary layer is 285–297 K), where the emulator performs well.

Behind the sea breeze at sunset, weaker negative perturbations relative to those ahead of the sea breeze are observed. IvJ18 separated these two negative tracer perturbation plumes into one associated with boundary layer mixing and the other from horizontal sea breeze advection. However, in our ensembles, due to the complicated moist convective processes occurring over land, such plume separation is not feasible.

2.3.4.1 Convective transport intensity

We now look at the maximum positive perturbation height as an indicator of the intensity of the convective aerosol redistribution in the sea breeze regime. We determine this height by finding the height where the positive perturbation reaches its maximum value. The surface concentration behind the sea breeze at sunset, which is examined by IvJ18, is excluded here since it is difficult to obtain a statistically robust emulator.

Over the deep regime, the maximum perturbation height dramatically increases with increasing boundary layer potential temperature (Figure 2.11d). The similar responses from the maximum updraft and the maximum cloud top over the deep regime imply that stronger updraft accomplishes the maximum aerosol venting, a result that is to be expected.

Over the shallow regime, the variance-based sensitivity analysis reveals that two parameters explain approximately 60% of the output variance: boundary layer potential temperature (31%) and inversion layer strength (29%). A warmer boundary layer and a weaker inversion layer lead to higher maximum perturbation heights (Figures 2.13e and 2.13f). These two parameters, which impact the lower tropospheric convective instability, are the same parameters that are key to the maximum updraft speed in the shallow regime. However, the relative importance of the boundary layer potential temperature here is similar to that of the inversion layer strength. It appears that the warmer and unstable boundary layer air that encounters the sea breeze-initiated convective updraft becomes more buoyant, ascends to a higher location, and transports the tracers to a higher height.

In IvJ18, soil saturation fraction is found to be the controlling parameter for the maximum location of the positive aerosol perturbation (45%) in an arid regime. In the moist regime examined here, sea breeze frontal uplift and boundary layer mixing are the primary processes responsible for the vertical redistribution of the tracers. In the presence of vigorous moist sea breeze-initiated convection, convective updrafts transport the tracer further aloft than the frontal uplift alone. Therefore, parameters contributing to the updraft strength variability also contribute to the variability in the vertical redistribution of tracer concentrations.

2.4 Summary and discussion

In this study, the relative importance of 10 different environmental parameters to the following characteristics of simulated tropical sea breeze convection is assessed: (1) the inland extent and characteristics of the sea breeze, (2) the intensity of convective updrafts over the land, and (3) the vertical redistribution of aerosols. Six atmospheric and four surface parameters, which describe the initial conditions of idealized sea breeze simulations, are perturbed simultaneously. A perturbed parameter ensemble of 130 sea breeze simulations is carried out using a high-resolution cloud-resolving model coupled to a two-way interactive land-surface model. Using statistical emulators, we conduct variance-based sensitivity analysis on each model output, thus decomposing the model output variance into contributions from the individual parameters and their interactions. This study builds upon IvJ18, which is the first study in the literature to examine the multidimensional sensitivity of the sea breeze characteristics and associated aerosol transport in a dry coastal desert environment.

In contrast to IvJ18, the current study considers moist convective processes and the role of interactive vegetation. The maximum inland extent of the sea breeze is mainly controlled by initial wind speed in both dry and moist regimes. In both regimes, the soil saturation fraction is found to be the predominant parameter for the sea breeze acceleration followed by the initial wind speed. Unlike the dry environment, the inversion layer strength and boundary layer height are identified to be significant for the sea breeze acceleration in the moist environment, possibly due to the susceptibility of sea breeze to the entrainment and turbulence of the ambient flow.

Our results also show that the mixed layer depth after the passage of the sea breeze is influenced by boundary layer height, initial wind speed, inversion layer strength, soil saturation fraction, and the sea-air temperature difference. Only boundary layer height, inversion layer strength, and sea-air temperature difference were important for the sea breeze mixed layer depth in the dry environment. The two additional parameters found to be important in the moist environment are (1) the soil saturation fraction, which influences the formation of convective clouds over land that then affect the boundary layer development and surface flux partitioning, and (2) the initial wind speed, which interacts with the vegetation canopy and influences the boundary layer turbulence.

The most vigorous convection, and the accompanying deepest clouds and strong updrafts, are localized along the sea breeze. In our ensemble we find two distinct regimes of this sea breeze-initiated convection: a shallow and a deep convection regime. Over the shallow regime, where the CAPE is limited, the initial inversion layer strength and boundary layer temperature are revealed as the main contributors to the intensity of the updraft speed, since they modulate the convective instability in the lower troposphere. In the deep regime, the primary control of the updraft speed is the initial boundary layer potential temperature, which is also a primary driver of the CAPE.

Ahead of the sea breeze, diurnal boundary layer convection develops. While the daytime boundary layer convection and accompanying weaker updrafts are not initiated by sea breeze forcing, they could play a substantial role in the preconditioning of the sea breeze convection. The boundary layer convection updraft speeds increase when boundary layer mixing is active due to drier soil or a weaker inversion.

To assess environmental parameters contributing to the variability in the potential vertical redistribution of the aerosol via convection, the change in the number concentration of the microphysically and radiatively inactive tracers between sunrise and sunset is examined. Whereas the aerosol venting is associated primarily with the frontal lift and the boundary layer mixing behind the sea breeze front in the dry regime, in this study of the moist environments, aerosols are vented higher aloft in the presence of the moist deep convective processes initiated along the sea breeze.

The results of this study also have the following implications for the improvement of operational weather and air quality forecasting in the sea breeze regime:

1. While the initial wind speed is found to be critical for coastal zones with both bare soil desert and tropical rainforests, different surface characteristics (e.g., vegetation canopy, surface roughness length, soil type) can significantly impact the wind flow via surface fluxes and associated turbulence, thereby altering the sea breeze structure. The impact of

surface characteristics on the sea breeze can be further convoluted over coastal urban regions with urban heat island and complex building geometry (Hu and Xue, 2016). Therefore, further sensitivity experiments of the sea breeze over coastal urban regions could be particularly beneficial for coastal megacities (e.g., Luanda, Panama, Kuala Lumpur). In summary, better representation of the near-surface wind fields (which current numerical weather prediction struggles with; e.g., Crook and Sun, 2004; Hong, 2003; Spark and Connor, 2004), and utilization of an interactive land-surface (e.g., Holtslag et al., 2013), are possible avenues for improving sea breeze forecasts.

2. Warmer boundary layer potential temperature leading to higher CAPE produces deep convection along the sea breeze whereas inversion layer strength has more of an impact on whether the convection remains primarily shallow. This result highlights the need to better represent convective instability of both near-surface and the entire tropospheric column if we are to predict coastal convection and resulting aerosol transport properly. In order to do this, attention should be given to improving both our representation of environmental specific humidity as well as surface processes.
3. Significant parameter interactions are found to be important to the maximum updraft in the shallow regime. This underscores the importance of further investigating the interactions between the environmental parameters that control the intensity of the sea breeze-initiated convection.

This study identifies the key parameters impacting tropical sea breeze and associated convective activities, and subsequently hints which properties warrant further investigation. To enhance the process-level understanding, future studies can build on this study focusing on the feedback mechanisms involving aerosol-cloud-land surface interactions.

CHAPTER 3: ENVIRONMENTAL MODULATION OF AEROSOL IMPACTS ON TROPICAL SEA BREEZE CONVECTION

3.1 Introduction

During the day, differential heating over land and ocean surfaces induces a thermally driven sea breeze circulation. Diurnally recurring sea breeze convection is a key contributor to rainfall in the tropics (e.g., Yang and Slingo, 2001; Laing et al., 2011; Wang and Sobel, 2017; Natoli and Maloney, 2019; Riley Dellaripa et al., 2020). Given increasing populations within coastal regions (United Nations Atlas of the Oceans http://www.oceansatlas.org) and the possible changes in precipitation in a changing climate (Chou et al., 2009; O'Gorman, 2012; Kendon et al., 2014; Tharammal et al., 2017), enhancing our understanding of the responses of sea breeze convection to various environmental parameters is critical. To this end, several extensive efforts have been made into determining those environmental factors that support and enhance the development of sea breeze convection (Crosman and Horel, 2010; Igel et al., 2018; Miltenberger et al., 2018a, 2018b; Park et al., 2020). However, as numerous environmental parameters coexist, covary, and interact with one another within sea breeze regimes, accurate representations of sea breeze convection within numerical weather prediction models remain challenging.

Collocated with a continuous increase in the coastal human population, a rise in aerosol emissions due to anthropogenic activities and biomass burning (Andreae et al., 2004; Reid et al., 2012; Wang et al., 2013) can further complicate the behavior of sea breeze convection through radiative, microphysical, and dynamical feedback processes. Firstly, some aerosol particles can serve as cloud condensation nuclei (CCN) depending on their size and composition. When the number concentration of CCN is increased, so is the competition for available water vapor among cloud droplets. As a result, a greater number of smaller cloud droplets are formed (Twomey and Squires, 1959), thereby increasing the cloud albedo (Twomey, 1974) and the longevity of the cloud (Albrecht, 1989), the so called first and second aerosol indirect effects.

It has been postulated in the literature that increased aerosol concentrations may strengthen deep convective updrafts through aerosol-induced convective invigoration. In these studies it has been proposed that as a greater number of smaller cloud droplets form under conditions of enhanced aerosol loading, the warm rain process is suppressed, and the cloud droplets are lifted above the freezing level. Once these droplets freeze, they release latent heating, thereby making clouds more buoyant and potentially strengthening updrafts. This process, which takes place in the mixed phase regions of clouds, is often referred to as cold phase invigoration and has been reported in both observational and modeling studies (e.g., Andreae et al., 2004; Khain et al., 2005; van den Heever et al., 2006; Rosenfeld et al., 2008). Under increased aerosol loading, the condensational growth rate of the population of more numerous smaller cloud droplets increases due to the increased exposed total droplet surface area, thereby releasing more latent heating and enhancing convective updrafts. These warm-phase aerosol-cloud dynamical feedbacks have collectively been termed condensational invigoration (Kogan and Martin, 1994; Seiki and Nakajima, 2014) or warm phase invigoration (Fan et al., 2018), and have been demonstrated in several warm-cloud studies (Kogan and Martin, 1994; Pinsky et al., 2013; Seiki and Nakajima, 2014; Koren et al., 2014; Saleeby et al., 2015; Sheffield et al., 2015). Several studies of deep convection have also reported condensational invigoration within warm-phase updrafts (Wang, 2005; Fan et al., 2007, 2018; Lee et al., 2008; Storer and van den Heever, 2013; Chen et al., 2017; Lebo, 2018).

While the convective invigoration theories have proposed stronger updrafts and heavier precipitation for convective clouds developing within enhanced aerosol loading environments, several studies have presented conflicting results. This lack of consensus of aerosol impacts on deep convection has been attributed to aspects including the cloud types (Seifert and Beheng, 2006; van den Heever et al., 2011), the storm life cycle (van den Heever et al., 2006), the covariation of aerosol properties with meteorological conditions (Varble et al., 2018; Posselt et al., 2019), and the different models (Stevens et al., 2018; Marinescu et al., 2020). Others also have found a modulation of aerosol impacts by the environment. Khain et al. (2008) showed that precipitation responses to enhanced aerosol loading vary depending on the relative humidity of the environment, as it affects the dominant terms between generation and the loss of the condensate mass. Tao et al. (2012) also demonstrated that precipitation may increase, decrease, or remain the same under enhanced aerosol loading due to environmental modulation. The impacts of a variety of environmental parameters on aerosol-cloud relationships have also been examined in both observational and modeling studies and include a focus on environmental conditions such as convectively available potential energy (CAPE, Lee et al., 2008; Storer and van den Heever, 2010), moisture (Grant and van den Heever, 2015; Khain et al., 2005, 2008; Tao et al., 2007), and wind shear (Fan et al., 2009; Lebo and Morrison, 2014; Marinescu et al., 2017).

Aerosol particles can also interact directly with radiation, through scattering and/or absorption, in what are referred to aerosol direct effects. As a result, surface energy budgets, including shortwave and longwave radiation, and the surface sensible and latent heat fluxes, can be impacted by the presence of aerosols. A number of modeling studies have highlighted the importance of considering both the radiative and microphysical effects of aerosol particles on interactive land surfaces and the resulting development of the boundary layer and convective clouds. For instance, Yu et al. (2002) found that reduced surface sensible heat fluxes due to scattering aerosols cool the lower troposphere, suppress the boundary layer development, and enhance the capping inversion. Niyogi et al. (2007) suggested that this aerosol-radiation-land surface feedback process reduces CAPE and thus suppresses precipitation. Saide et al. (2015) also reported the enhancement of the capping inversion, where the impacts of biomass burning smoke on tornadic environmental conditions were examined. Jiang and Feingold (2006) also considered a coupled aerosol-cloud-radiation-land surface framework in large-eddy simulations and found that shallow over-land convection becomes weaker as a result of aerosol direct effects. Their results suggest that neglecting aerosol-radiation-land surface interactions may result in the overestimation of aerosol impacts on over-land convection. From these studies, it is clear that there are intricate links between aerosol-radiation interactions, with potential subsequent feedbacks to the environment and developing convection.

Examining both the radiative and microphysical impacts of aerosol particles on convective updrafts and precipitation under a wide range of environmental conditions, including both those in the atmosphere and those governing the land surface, is therefore fundamental to bolstering our understanding of aerosols on cloud systems and the environments in which they form. The primary goals of this study are therefore twofold. The first goal is to investigate both direct and indirect effects of aerosols on the over-land convection developing in association with tropical sea breeze flow regimes. The second goal is to determine whether and how these convective responses to enhanced aerosol loading may vary as a function of the environment.

To achieve our stated goals, we need to examine these aerosol-cloud interactions within a fully interactive aerosol-radiation-cloud-land surface framework and under a wide range of different tropical sea breeze environments. This is accomplished through the use of idealized numerical simulations in which we investigate the impact of varying aerosol number concentrations on the characteristics of sea breeze convection that develops under 130 different initial environmental conditions. More specifically, we extend Park et al. (2020) in which we assessed the relative importance of ten different thermodynamic, wind, and surface properties on the sea breeze convection under a relatively pristine aerosol scenario, by including polluted conditions (where by "polluted" we simply mean increased aerosol loading and are not specifically referring to anthropogenic aerosols). Conducting the additional suite of 130 tropical sea breeze simulations under a relatively polluted scenario allows us to assess the role of radiatively and microphysically active aerosols on the sea breeze convection, and how these aerosol effects may vary as a function of the 130 different sea breeze environments represented here. We then explicitly investigate how the convective responses to enhanced aerosol loading change when aerosol direct effects are excluded by conducting two smaller ensembles, one polluted and one clean, that are comprised of the 12 initial conditions that produce deep convection in the original pristine ensemble, and in which aerosol-radiation interactions are now excluded.

Detailed experiment design, model configuration, and analysis methodologies are demonstrated in Section 3.2. Section 3.3 describes the development of sea breeze and over-land convection ahead of and along the sea breeze. The overall differences between pristine and polluted ensembles in terms of radiation and associated convective environments are then shown in Section 3.4. In Section 3.5, changes in convective responses represented by cloud top heights, updraft velocities, and surface precipitation with enhanced aerosol loading are discussed. The impacts of eliminating the aerosol direct effect on convective responses are explicitly addressed in Section 3.6. The environmental modulation of the various aerosol impacts on sea breeze convection is simultaneously examined throughout Sections 3.4, 3.5 and 3.6.

3.2 Experiment design and analysis methodologies

3.2.1 RAMS model configuration and experimental setup

Ensembles of idealized numerical simulations of tropical sea breezes are conducted using the Regional Atmospheric Modeling (RAMS) version 6.2.08 (Cotton et al., 2003; Saleeby and van den Heever, 2013). Idealized simulations are sufficiently complex to capture the systems of interest but sufficiently simple to allow for the isolation and evaluation of the critical physical processes at play, without the addition of unnecessary confounding factors in more complex case-study simulations. As our focus is on tropical sea breeze convection, the idealized simulations are initialized using conditions that are representative of equatorial coastal rainforest regions, such as the Cameroon rainforest region (Grant and van den Heever, 2014).

The RAMS model configuration is identical to that used in Park et al. (2020) and is summarized in Table 3.1. The three-dimensional non-rotating ($f = 0$ s^{-1}) domain is comprised of 150×1500×57 grid points. Since our focus is the sea breeze over equatorial tropics, the latitude which influences sea breeze's inland extent via its impact over the Coriolis parameter is not perturbed here as one of the parameters. The horizontal grid spacing is 1 km, and a 100-m vertical grid spacing near the surface is vertically stretched to 1 km near the model top. With this spatial resolution the structure of the sea breeze circulation and associated convective clouds are well represented. Each simulation is run from 0000 Local Time (LT) for 24 h using a 3-s time step. Output files are saved every 10 minutes. Lateral boundary conditions are open-radiative (Klemp and Wilhelmson, 1978) in the zonal direction and periodic in the meridional direction.

Convection is initiated through the use of random potential temperature perturbations of 0.1 K in amplitude that are initially introduced within the lowest 500 m of the atmosphere. We also employ Smagorinsky (1963) deformation-K closure turbulence parameterization with stability modifications by Lilly (1962) and Hill (1974).

Table 3.1. RAMS model configuration

Model Aspect		Setting
Grid		Arakawa C grid (Mesinger and Arakawa, 1976) Single grid 1500 points×150 points, $\Delta x = \Delta y =$1 km 57 vertical levels, $\Delta z =$100 m lowest level stretched to $\Delta z =$ 1 km aloft
Integration		24 hr, $\Delta t = 3$s
Boundary conditions		Zonally open-radiative (Klemp and Wilhelmson, 1978), meridionally periodic
Initialization		• 130 horizontally homogeneous thermodynamic and wind profiles where the following parameters are simultaneously perturbed within the indicated value ranges (Igel et al., 2018; Park et al., 2020): (1) boundary layer potential temperature, [285, 300] K (2) boundary layer relative humidity, [75, 95]% (3) boundary layer height, [100, 1000] m (4) inversion layer strength, [1, 15] K km^{-1} (5) inversion layer depth, [100, 1000] m (6) zonal wind speed without vertical shear, [-5, 5] m s^{-1} (7) temperature difference between the sea surface and the lowest model level atmosphere [-10, 10] K (8) horizontal gradient of sea surface temperature [-0.02, 0.02] K km^{-1} (9) temperature difference between the land surface and the lowest model level atmosphere [0, 10] K (10) soil saturation fraction, [0.1, 0.9] • Random potential temperature perturbations within the lowest 500 m of the domain with a maximum perturbation of 0.1 K at the surface are used to initiate convection
Radiation		• Two-stream, hydrometeor-sensitive (Harrington, 1997) • Updated every 60s
Turbulence		Smagorinsky (1963) deformation K with stability modifications (Hill, 1974)
Surface	Land	• Two-way interactive Land-Ecosystem-Atmosphere-Feedback version 3 (LEAF-3, Walko et al., 2000) • Evergreen broadleaf tree with 90% vegetation fraction • 11 vertical soil levels with sandy clay loam
	Ocean	Non-interactive, with fixed temperature and horizontal temperature gradient
Microphysics		Double-moment bin-emulating bulk scheme with eight hydrometeors (Walko et al., 1995; Meyers et al., 1997; Saleeby and Cotton, 2004; Saleeby and van den Heever, 2013)
Aerosol treatment		• Ammonium sulfate aerosols available to act as CCN (Saleeby and van den Heever, 2013) o Exponentially decreasing number concentration with height from the surface; pristine = 500 mg^{-1}, polluted = 2000 mg^{-1} o Single mode, log-normal distribution o Sources and sinks • DeMott et al. (2010) ice nucleation

RAMS is coupled to the Land-Ecosystem-Atmosphere Feedback version 3 (LEAF-3), a fully interactive soil-vegetation-atmosphere parameterization (Lee, 1992; Walko et al., 2000). To simulate an idealized sea breeze circulation, two different surfaces, one land and one ocean, are separated by a straight coastline located at the center of the domain. In our idealized setup, which is representative of tropical coastal rainforest similar to equatorial Africa, the western half of the domain is the land region and is specified to be a rainforest with evergreen broadleaf trees and sandy clay loam soil type (Grant and van den Heever, 2014). The eastern half of the domain is the ocean, and the horizontal gradient of the sea surface temperature is kept fixed throughout the simulation. The relative location of land and ocean is chosen arbitrarily and could have just as easily been the other way around.

RAMS contains a two-moment bulk microphysics parameterization (Meyers et al., 1997; Saleeby and Cotton, 2004, 2008; Saleeby and van den Heever, 2013) that prognoses the number concentration and mass mixing ratio of eight hydrometeor classes: cloud, drizzle, rain, pristine ice, snow, aggregates, graupel, and hail. Each hydrometeor class is represented by a generalized gamma distribution function. The RAMS microphysics emulates a bin microphysics parameterization for a number of different microphysical processes by utilizing lookup tables generated offline through the use of Lagrangian parcel bin model calculations, including aerosol activation (Saleeby and Cotton, 2004), droplet collection (Feingold et al., 1988), and sedimentation (Feingold et al., 1998). A two-stream radiation parameterization (Harrington, 1997), which interacts with hydrometeors, is called every 60 seconds.

All of the simulations are initialized with horizontally homogeneous thermodynamic and wind profiles. As described in Park et al. (2020), we make use of 130 different initial environmental conditions, where ten different lower-tropospheric thermodynamic, wind, and surface properties are simultaneously perturbed across a range of values representative of tropical, equatorial regions. These perturbed initial conditions are designed to investigate the impacts of different environmental parameters on the sea breeze structure and convective intensity. For the lower-tropospheric thermodynamic properties, five parameters defining the structure of the boundary layer and inversion layer are considered: (1) the boundary layer potential temperature; (2) boundary layer relative humidity; (3) boundary layer height; (4) inversion layer depth; and (5) the inversion layer strength. The upper tropospheric thermodynamic profiles above the boundary layer are identical for all 130 initial conditions. The initial zonal wind speed without vertical shear is also considered and represents the sixth environmental factor examined. Finally, sensitivity to the variations in the surface characteristics are also examined including: (7) the soil saturation fraction; (8, 9) the temperature difference between land/ocean surface and the atmospheric temperature at the lowest model level; and (10) the horizontal gradient of sea surface temperature. The ranges of the ten parameters tested are based on previous studies, are shown in Table 3.1 and are the same as those used by Igel et al. (2018) and Park et al. (2020). These ten parameters are perturbed using the maximin Latin Hypercube sampling method (Morris and Mitchell, 1995) to ensure optimal coverage of the 10-dimensional parameter space with a minimum number of parameter combinations and hence the minimum number of simulations (which is 130 simulations in each of the ensembles conducted here).

The aerosol type utilized in this study is restricted to single-mode, submicron, ammonium sulfate for simplicity, following Grant and van den Heever (2014). We chose ammonium sulfate due to its ubiquity in the atmosphere and its ability to serve as CCN due to its high solubility. While the vertically varying aerosol field is initialized horizontally homogeneously, aerosol particles are allowed to be redistributed via advection, convection, and nucleation following the initialization. Aerosol sources and sinks, including the return of aerosols to the environment following evaporation, are all incorporated (Saleeby and van den Heever, 2013), and heterogeneous nucleation of ice is parameterized following DeMott et al. (2010).

Four different ensembles of idealized simulations with different aerosol conditions are performed. The name and description of each of the ensembles are summarized in Table 3.2. Here, "r" refers to aerosol-radiation interactions, and "On" means aerosol particles are allowed to interact with radiation. The rOn-500 ensemble was the suite of simulations examined in Park et al. (2020).

First, to examine the impacts of increasing the aerosol loading on sea breeze convection, two initial aerosol number concentrations that exponentially decrease with height are carried out for relatively pristine and polluted scenarios. A maximum concentration of 500 mg^{-1} and 2000 mg^{-1} at the surface (Figure 3.1) represents the pristine conditions (also referred to as ensemble rOn-500) and the polluted (also referred to as ensemble rOn-2000) conditions, respectively. We shall use the terms “pristine” and “rOn-500”, and “polluted” and “rOn-2000” interchangeably throughout this manuscript to refer to these conditions. These aerosol concentrations are chosen based on observations made in equatorial Africa (Andreae et al., 1992; Kacarab et al., 2020). It is important to note that while 130 different initial conditions are implemented in each ensemble, that each ensemble utilizes the same 130 different initial conditions, thereby facilitating direct comparisons between the corresponding ensemble pairs.

Table 3.2. The naming convection and descriptions of four different ensembles.

Name	Aerosol loading	Aerosol-radiation interactions	Total number of simulations	Color
rOn-500	pristine, 500 mg^{-1}	On	130	Blue
rOn-2000	polluted, 2000 mg^{-1}		130	Red
rOff-500	pristine, 500 mg^{-1}	Off	12	Light blue
rOff-2000	polluted, 2000 mg^{-1}		12	Light red

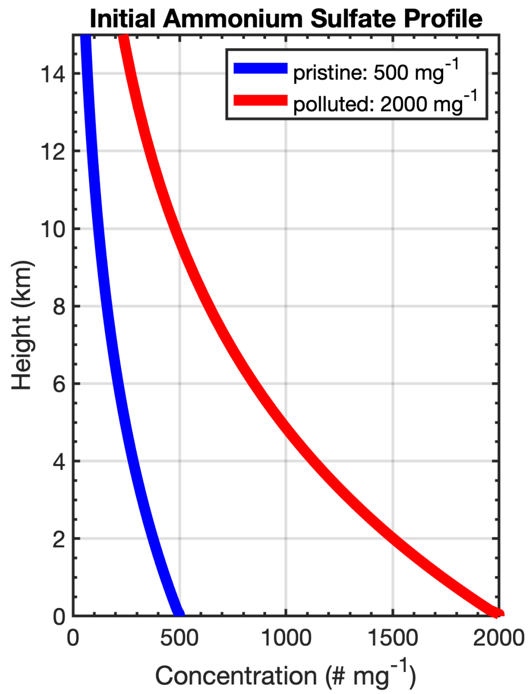

Figure 3.1. Initial number concentration of ammonium sulfate for the pristine (blue line, 500 mg^{-1} at the surface, rOn-500 and rOff-500) and polluted (red line, 2000 mg^{-1} at the surface, rOn-2000 and rOff-2000) model ensembles.

Secondly, to examine the impact of aerosol indirect effects on deep convective development, aerosol-radiation interactions are turned off for two additional, much smaller ensembles comprised only of those 12 simulations in rOn-500 that produce deep convection. These ensembles are referred to as rOff-500 and rOff-2000. While aerosol particles are allowed to interact with radiation in rOn-500 and rOn-2000, aerosol-radiation interactions are turned off for rOff-500 and rOff-2000. It is important to note that radiation is always fully interactive with the microphysics in all four of the ensembles analyzed here.

3.2.2 Analysis methodology

As with Park et al. (2020), we apply an advanced statistical algorithm developed by Lee et al. (2011) and Johnson et al. (2015) that includes statistical emulation (O'Hagan, 2006) and variance-based sensitivity analysis (Saltelli et al., 2000), over the ten-dimensional parameter input parameter space. Due to its computational efficiency, this advanced statistical algorithm has been utilized in several modeling studies (Feingold et al., 2016; Igel et al., 2018; Glassmeier et al., 2019; Marshall et al., 2019; Wellmann et al., 2018, 2020; Park et al., 2020) that quantify the sensitivity of numerical model responses to a range of input parameters.

This advanced algorithm incorporates the Gaussian process emulation (O'Hagan, 2006; Rasmussen and Williams, 2006) to build a statistical surrogate representation of complex cloud-resolving model responses of the parameters of interest. Over the ten-dimensional parameter space, the emulator estimates the cloud-resolving model responses at untried input parameter combinations, thereby densely sampling the output of interest and thus allowing us to understand the relationship between the perturbed input parameter and output responses without having to conduct simulations representative of each set of perturbed parameters. We can then quantify the relative importance of the perturbed input parameters on the output of interest via variance-base sensitivity analysis. Further details of how this approach was used to determine the predominant environmental factors impacting tropical equatorial sea breeze convection are included in Park et al. (2020). We now begin our analysis by examining the morphology of the convection that develops within the pristine and polluted ensemble of simulations in which aerosol-radiation interactions are turned on.

3.3 Basic description of the sea breeze simulations

In this section, an overview of the convective morphology and development within our tropical sea breeze simulations is provided. After sunrise (0600 LT), the sea breeze circulation becomes evident, and convergence along the leading edge of the sea breeze is evident at the coastline, where the highest land-sea thermal contrast is established. Throughout the daytime, and even shortly after sunset (1800 LT), the sea breeze continues to propagate further inland, in keeping with our knowledge of such baroclinic circulations. Lines of convective clouds form over land between 1200–1800 LT along the sea breeze convergence line (Figure 3.2). The sea breeze is observed to develop in all 260 simulations of the rOn-500 and rOn-2000 ensembles (130 simulations in each ensemble), the location of which is detected at every output timestep using an identification algorithm developed by Igel et al. (2018).

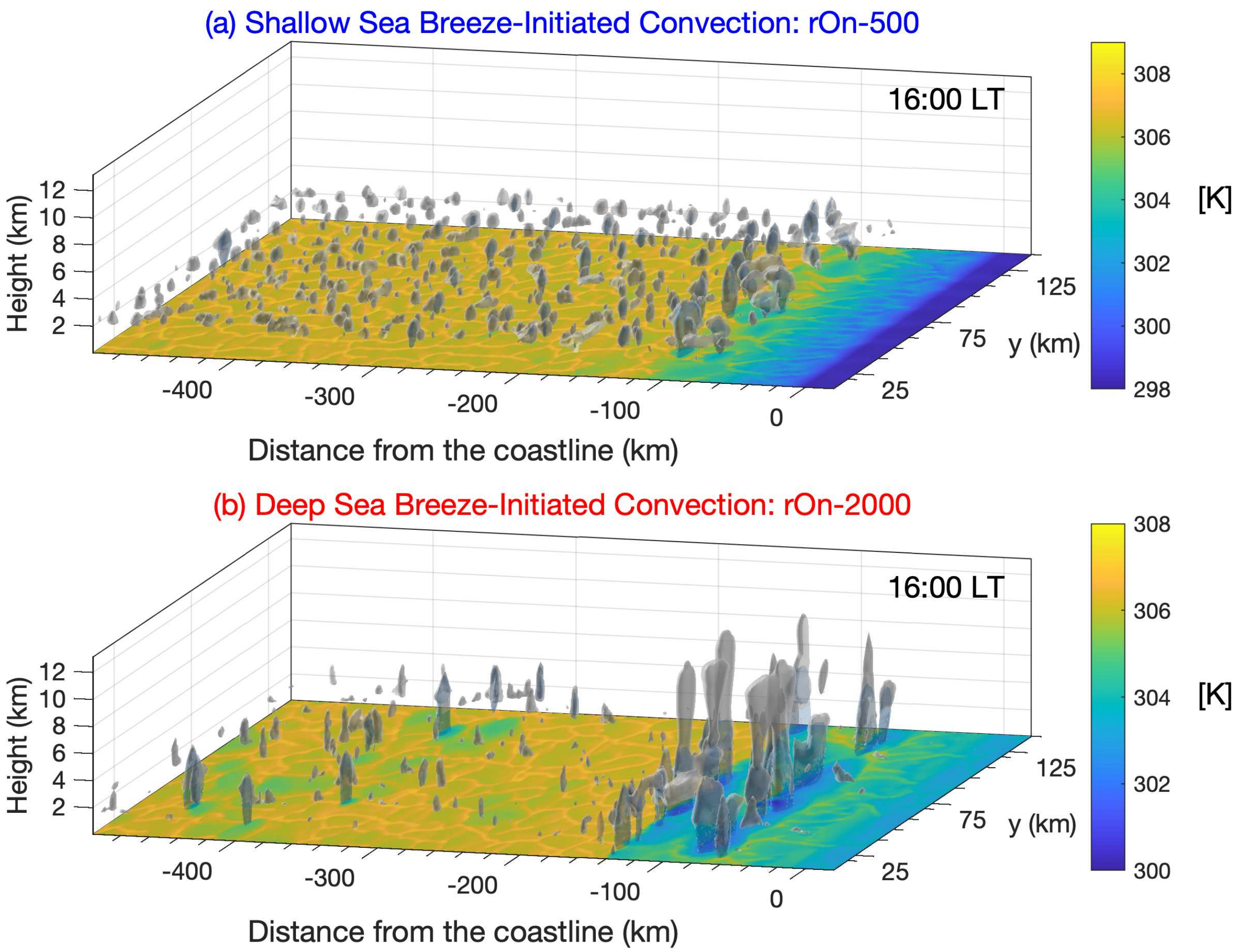

Figure 3.2. Examples of the convective morphologies observed in the rOn-2000 ensemble where the sea breeze-initiated convection is (a) shallow (Test 14) and (b) deep (Test 27) at 16:00 LT. White isosurfaces are where total condensate, with the exception of for rain, is 0.1 g kg^{-1}, and dark blue isosurfaces are where rain mixing ratio is 0.1 g kg^{-1}. The shaded contours at the

surface are density potential temperature (K; Emanuel, 1994) at the lowest model level. Only a 520 km×130 km subset of the domain is displayed here.

Two types of over-land convection are evident between 1200–1800 LT. Ahead of the leading edge of the sea breeze, boundary layer heating and mixing induce boundary layer convection, whereas along the leading edge of the sea breeze, where low-level air parcels get lifted to the level of free convection through low-level convergence, sea breeze-initiated convection occurs. Figures 3.2a display an example rOn-2000 simulation, where both the boundary layer convection ahead of the sea breeze, as well as shallow (cloud top heights < 4 km AGL) sea breeze-initiated convection are evident. In this case, while both of these modes of convection remain shallow, the sea-breeze initiated convection is characterized by slightly deeper clouds and stronger updrafts than the boundary layer convection forming ahead of this line. Deep convection (cloud top heights > 7 km AGL) may also form along the sea-breeze convergence zone (Figure 3.2b). In these cases, it is accompanied by significantly heavier precipitation and stronger updrafts than those associated with the sea breeze-induced shallow modes. These different modes of convection that develop depend on the 130 prescribed initial environmental conditions. We now turn our attention to the way in which aerosols may impact the convective environments and subsequent convective development.

3.4 Aerosol impacts on radiation and associated environmental characteristics

In order to examine the impacts of aerosols on the convective environment, we first examine the effects of varying aerosol concentrations on the surface radiation budget. Ammonium sulfate aerosols are expected to scatter radiation but not strongly absorb it (Atwood et al., 2017). Therefore, the longwave direct effect is expected to be minimal. The aerosol direct effects are therefore addressed by analyzing the differences in surface downwelling shortwave and upwelling longwave radiation between rOn-500 and rOn-2000 for clear-sky columns. For clear-sky columns, we have assumed that the total condensate mixing ratio is smaller than 0.01 g kg^{-1} at all vertical levels. For all 130 corresponding pairs of simulations of the rOn-500 and rOn-2000 ensembles, as the aerosol number concentrations are increased between the ensembles, the downwelling shortwave radiation decreases throughout the atmosphere over land (Figure 3.3a) and ocean (Figure 3.3b), with the maximum difference occurring at the surface (not shown). The daytime-averaged (0600–1800 LT) surface shortwave radiation difference between rOn-500 and rOn-2000 is 81.2 W m^{-2} for the ensemble average, with a standard deviation of 6.5 W m^{-2}.

The surface upwelling longwave radiation (Figures 3.3c and 3.3d) subsequently responds to the aerosol-induced changes in incoming solar radiation. Due to the much lower heat capacity of the land surface compared to the ocean surface, the longwave emission significantly decreases over the land surface as it rapidly responds to the reduction in shortwave radiation in the polluted ensemble. With less surface upwelling longwave radiation, the interactive land surface and the air above it, become cooler (Figure 3.3e) with enhanced aerosol loading. Over the ocean regions, the SST is fixed throughout the simulation. As such, the potential temperature of the lowest level air does not change significantly over the ocean since the longwave radiation remains almost the same (Figure 3.3f). However, even if the SST had been allowed to vary, the upwelling longwave radiation from the ocean surface would not respond as quickly to the aerosol-induced reduction in shortwave radiation as that over the land surface, given the higher heat capacity of the ocean. As a result, the ensemble-mean surface temperature difference between the ocean and the land

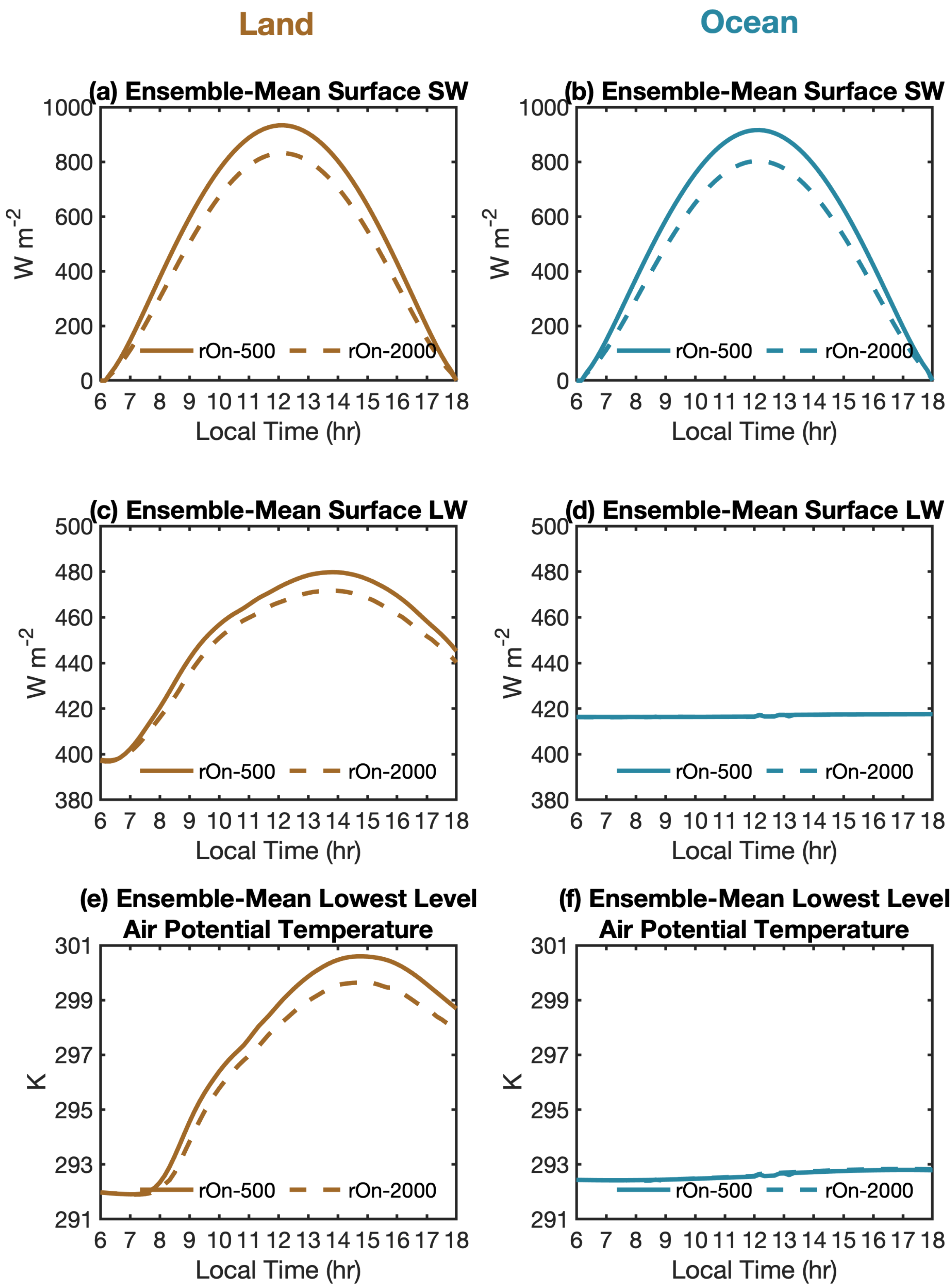

Figure 3.3. Time series of the ensemble-mean (a,b) surface downwelling shortwave radiation, (c,d) surface upwelling longwave radiation, and (e,f) lowest model level potential temperature over land (left column, brown lines) and ocean (right column, blue lines). Solid and dashed lines denote rOn-500, and rOn-2000, respectively.

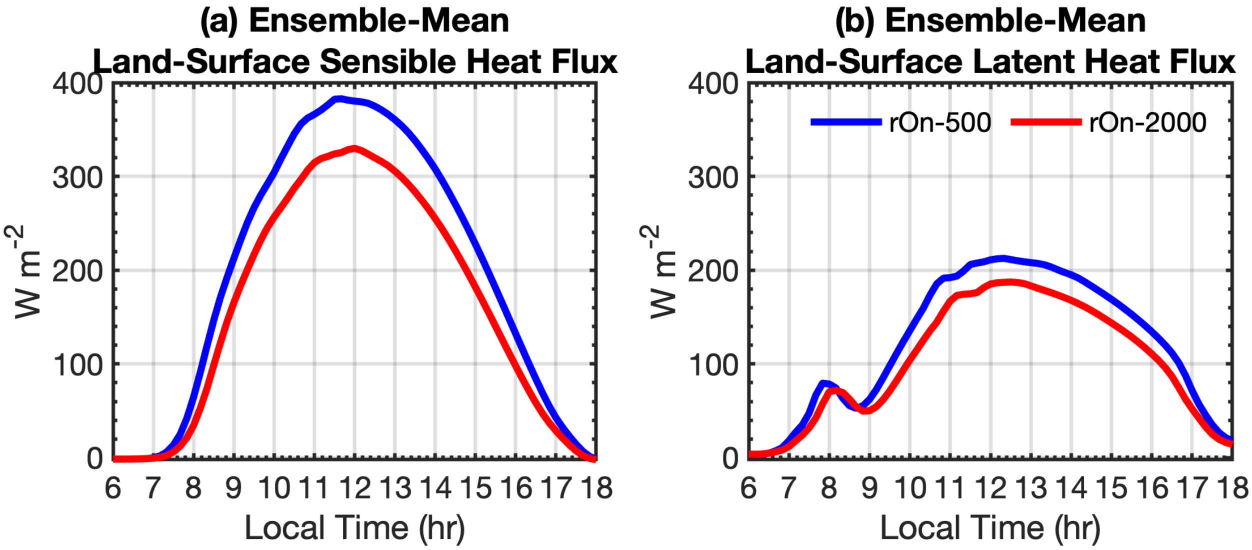

Figure 3.4. Time series of the ensemble-mean land surface (a) sensible heat flux and (b) latent heat flux, spatially averaged from western domain edge to the 50 km ahead of algorithm-identified sea breeze front, for the rOn-500 (blue) and rOn-2000 ensembles (red).

would therefore be less in the polluted case when compared with the pristine case (Figures 3.3e and 3.3f). This has implications for the land-sea temperature difference in pristine versus polluted conditions, and hence for the strength of the sea breeze circulation itself. The implications of this are discussed in more detail below.

The aerosol-induced reduction in incoming solar radiation reaching the surface also impacts the surface fluxes. Figure 3.4 displays the temporal evolution of the surface sensible and latent heat fluxes of the environment ahead of the sea breeze front, averaged over all 130 simulations in each ensemble. Both the ensemble-mean sensible (~19%) and latent (~15%) heat fluxes are reduced in rOn-2000 compared with rOn-500 due to the enhanced aerosol scattering throughout the 0600–1800 LT. This reduction in incoming solar radiation and associated surface fluxes responses due to enhanced aerosol loading is in good agreement with the findings from previous studies (Yu et al., 2002; Koren et al., 2004; Feingold et al., 2005; Jiang and Feingold, 2006; Zhang et al., 2008; Grant and van den Heever, 2014). Such a reduction in sensible and latent heating will, in turn, negatively impact the convective boundary layer by limiting the heating and moistening of this layer. The surface-based mixed layer depth, defined here as the level above the surface at which the vertical gradient of the potential temperature first exceeds 2 K km^{-1}, decreases in rOn-2000 due to the reduction in surface sensible heat flux and associated turbulent mixing. The percentage difference of the mean surface based-mixed layer depth ahead of the sea breeze front between rOn-500 and rOn-2000 is shown in Figure 3.5a, where it is evident that the mixed layer is shallower in the polluted ensemble by 1.6% to 23% when compared with the pristine ensemble.

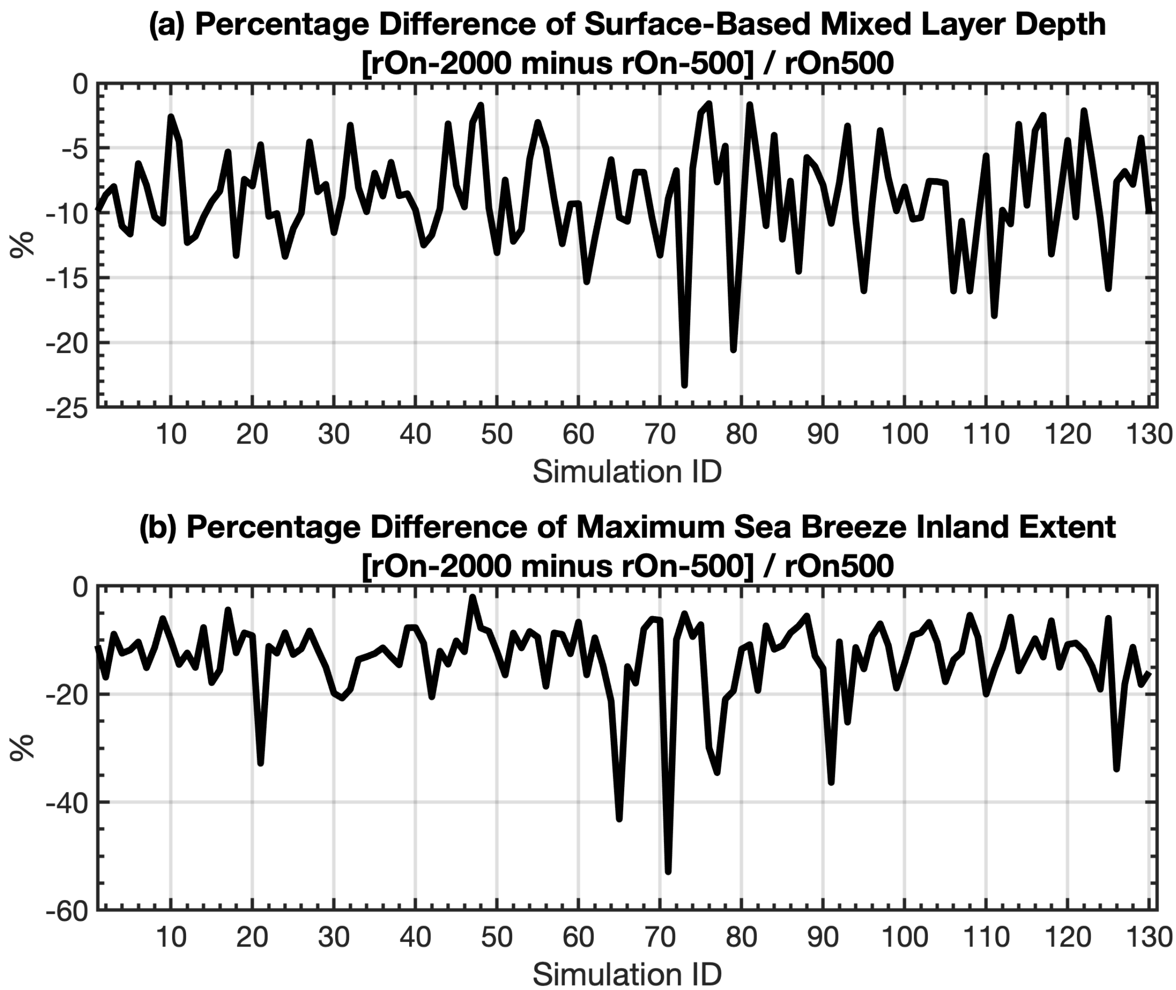

Figure 3.5. The percentage difference between the rOn-500 and rOn-2000 ensembles for (a) the surface-based mixed layer depth averaged from the western domain edge to 50 km ahead of the algorithm-identified sea breeze front between 1200–1800 LT and (b) the maximum sea breeze inland extent. The numbers on the horizontal axis refer to the arbitrarily identified simulation identities.

The results of this section indicate that two of the three convective (Doswell, 1987), lower-tropospheric moisture (as represented by the latent heat fluxes) and instability (as represented by the mixed layer depth), become less favorable for convective development in rOn-2000 compared with rOn-500, as a result of the aerosol-induced reduction of incoming solar radiation. The third convective ingredient is lift (Doswell, 1987), which in these simulations is provided by the differential heating over the land and ocean surfaces and the convergence along the sea breeze front. To first order, the faster the sea breeze moves, the further inland the sea breeze travels, the stronger the convergence along the sea breeze front, and hence the greater the lift. Here we therefore examine the maximum inland extent of sea breeze front as an indicator of sea breeze intensity and hence lift (Figure 3.5b). The maximum inland extent of the sea breeze front is identified as the last location of the sea breeze front detected by the sea breeze front algorithm (Igel et al., 2018). The percentage difference of the maximum sea breeze inland extent between the polluted and pristine ensembles varies from −2% to −53%, and it is evident from Figure 3.5b that the sea breeze extent is less in rOn-2000 than rOn-500 for each and every one of the ensemble pairs.

The weakening of the sea breeze circulation and associated inland extent is attributed to the reduced land-sea thermal contrast. As discussed above, the reduction in downwelling shortwave radiation at the surface and the subsequent changes in surface upwelling longwave radiation which regulates surface temperature, lead to the cooler land surface in the polluted ensemble. With fixed SSTs and hence near-surface temperatures in rOn-500 and rOn-2000, the lower land surface temperature in rOn-2000 results in a weaker thermal gradient between the land and ocean surfaces, producing weaker lifting via sea breeze convergence. As the thermal gradient between the land and ocean is the primary driver of sea breeze circulation, the baroclinic circulation weakens in the polluted ensemble, and hence the sea breeze extent, intensity and convergence all weaken as the aerosol loading is enhanced. It is therefore evident from these results that the third element of convection, lift, which is provided by the sea breeze convergence and thermal buoyancy, is also reduced in rOn-2000 when compared with rOn-500. As all three convective ingredients (moisture, instability, and lift) are reduced in the presence of enhanced aerosol loading due to the aerosol direct effect, we could therefore expect the presence of increased aerosol concentrations to reduce the intensity of the sea breeze deep convection in the absence of all other aerosol effects. We investigate this in more detail in the next section.

A similar result in which the three convective ingredients are reduced with enhanced aerosol loading was observed in Grant and van den Heever (2014). However, in that study, they only utilized one set of initial environmental conditions. Therefore, one might question whether such findings are applicable to other environmental conditions. Since rOn-500 and rOn-2000 each have 130 different initial conditions (remember that while the 130 initial conditions are different within each ensemble, each ensemble does have matching environmental pairs; see Section 3.2.1), these results suggest that the weakening of sea-breeze induced convection under enhanced aerosol loading observed by Grant and van den Heever (2014) is indeed robust in that the same results have been found to occur for the wide range of environmental conditions represented in these 130 pairs of pristine and polluted ensembles.

3.5 Impacts of enhanced aerosol loading on over-land convection

In the previous section, we demonstrated that the three convective ingredients, moisture, instability, and lift, are weakened near the surface in the polluted ensemble, when compared with the pristine ensemble, due to the direct impacts of the enhanced aerosol loading on incoming solar radiation. Now we seek evidence of the impacts of increased aerosol number concentrations on the intensity of over-land convection within tropical sea breeze flow regimes as a result of both the direct and indirect aerosol effects. More specifically, we investigate the impacts of enhanced aerosol loading on cloud top heights, convective updraft velocities, and precipitation, all of which are common indicators of convective intensity (e.g., Nesbitt and Zipser, 2003).

3.5.1 Cloud top heights

First, we examine the impacts of aerosol loading on cloud top height by analyzing the following: (1) the frequency distribution of the low (cloud top height < 4 km AGL), middle (4–7 km AGL), and deep (> 7 km AGL) clouds and (2) the maximum cloud top height. To identify cloud top heights, we start at the top of each model column and sample downwards until reaching the first level where the cloud water mixing ratio (the summation of cloud liquid water and pristine ice) exceeds 0.1 g kg^{-1}. This level is then regarded as the convective cloud top height, and as such, we do not take into account those situations in which there may be multiple different cloud levels in a column. The cloud top heights are sampled over land between 1200–1800 LT. As presented in Park et al. (2020) and displayed in Figure 3.6a, the vast majority of ensemble members in the rOn-500 ensemble are dominated by low clouds (cloud tops less than 4 km AGL). This low cloud dominance is also observed for the rOn-2000 ensemble (Figure 3.6b). Low clouds are the only mode to develop in 104 and 111 of 130 simulations in rOn-500 and rOn-2000, respectively. It is also interesting to note that there are two cases in rOn-2000 where no clouds develop (Test58 and Test61). The absence of cloud water with enhanced aerosol loading in these two cases appears to be due to their stronger (14.5 and 12.7 K km^{-1}) and deeper (965 and 714 m) inversion layers and cooler (289.7 and 286.0 K), drier (78.9 and 77.7%), and shallower (239 and

309 m) boundary layers in the initial conditions (fifth row in Table 3.1). While initial conditions are identical between rOn-500 and rOn-2000, with enhanced aerosol scattering, the low-level atmosphere is less unstable in rOn-2000, as discussed in Section 3.4. The aerosol enhanced stability in these cases appear to be sufficient to offset the initial environmental instability, resulting in no moist convective cloud development.

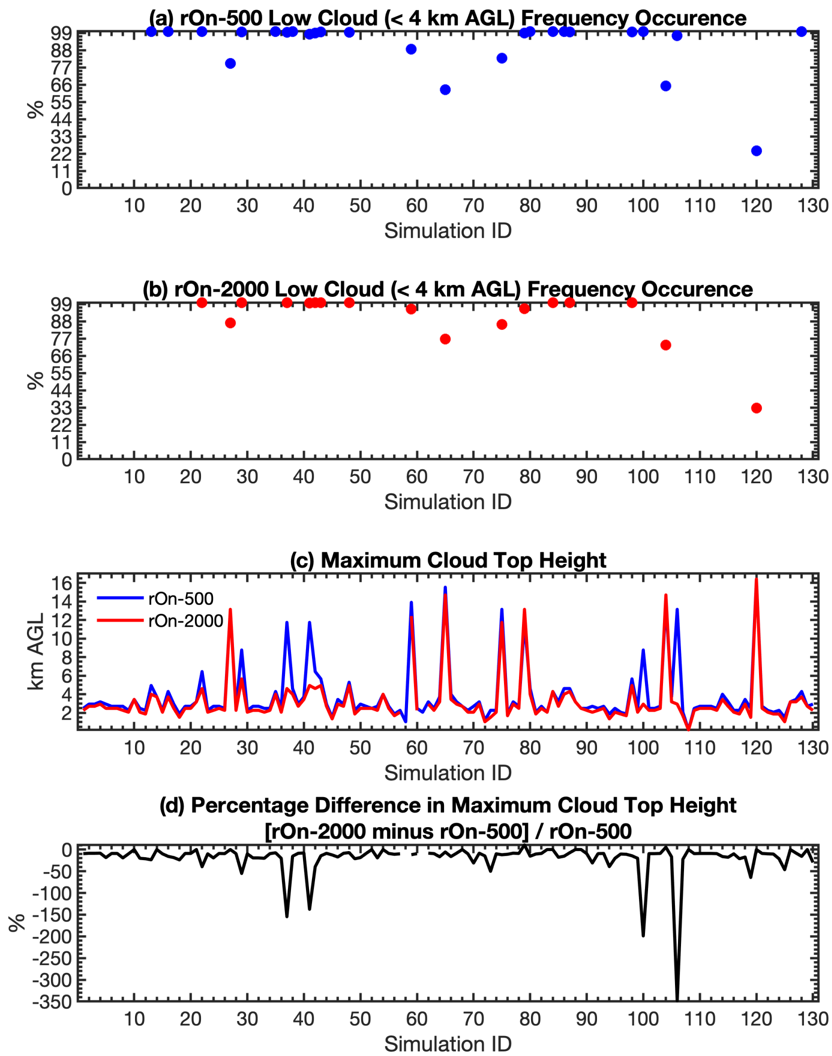

Figure 3.6. Cumulative frequency of low cloud (cloud top heights < 4 km AGL) occurrence in (a) rOn-500 and (b) rOn-2000; (c) maximum cloud top height (km) between 1200–1800 LT over land; (d) percentage differences of maximum cloud top height between rOn-500 and rOn-2000. Note that simulations with 100% low cloud frequency (recalling that these are cumulative frequencies) are not indicated in (a) and (b) for the sake of clarity and that those columns without dots are therefore those simulations which only have clouds with cloud tops less than 4 km AGL.

The overall suppression of over-land convection in rOn-2000 when compared with rOn-500 is evident in the maximum (Figure 3.6c) cloud top heights, as well as the percentage difference in the maximum cloud top height (Figure 3.6d), where the maximum cloud heights are always less in rOn-2000 than in rOn-500, except for two deep convective cases (Test79 and Test104). Furthermore, Figure 3.6c demonstrates that while there are 12 cases with deep convection in rOn-500, only 7 of these 12 cases have deep convection when the aerosol loading is enhanced in rOn-2000. This suppression of deep convection in rOn-2000 also directly corresponds with the cases where the low cloud fraction in rOn-2000 is higher than in rOn-500 (Figure 3.6a). The reasons for the suppression of deep convection will be further discussed in Section 3.6.1.

As mentioned above, Test79 and Test104, are the only two cases in which the maximum cloud top heights are higher in the polluted ensemble compared with their corresponding counterparts in the pristine ensemble. In these two cases, updrafts become stronger with enhanced aerosol loading above the freezing level, as will be discussed in Section 3.6.2 below.

3.5.2 Convective updraft velocities

In order to better understand the dynamical response of convection to enhanced aerosol loading, updrafts developing between 1200 and 1800 LT over land with velocities greater than 1 and 5 m s^{-1} are analyzed. The maximum updraft velocity (Figure 3.7a) represents the intensity of the most vigorous over-land convection. The strongest updrafts in all of the simulations of both ensembles are always found along the sea breeze front, irrespective of whether the convection is shallow or deep in this region. The mean (Figure 3.7b) and lower percentiles (25^{th}, 50^{th}, 75^{th}, 95^{th}) of the updraft velocities (Figure 3.7c–f), on the other hand, include the boundary layer convection signal. As demonstrated by Park et al. (2020), the 50th percentile (median) updraft velocities is an appropriate metric with which to differentiate between the sea breeze convection and the boundary layer convection, and we therefore employ that approach here too.

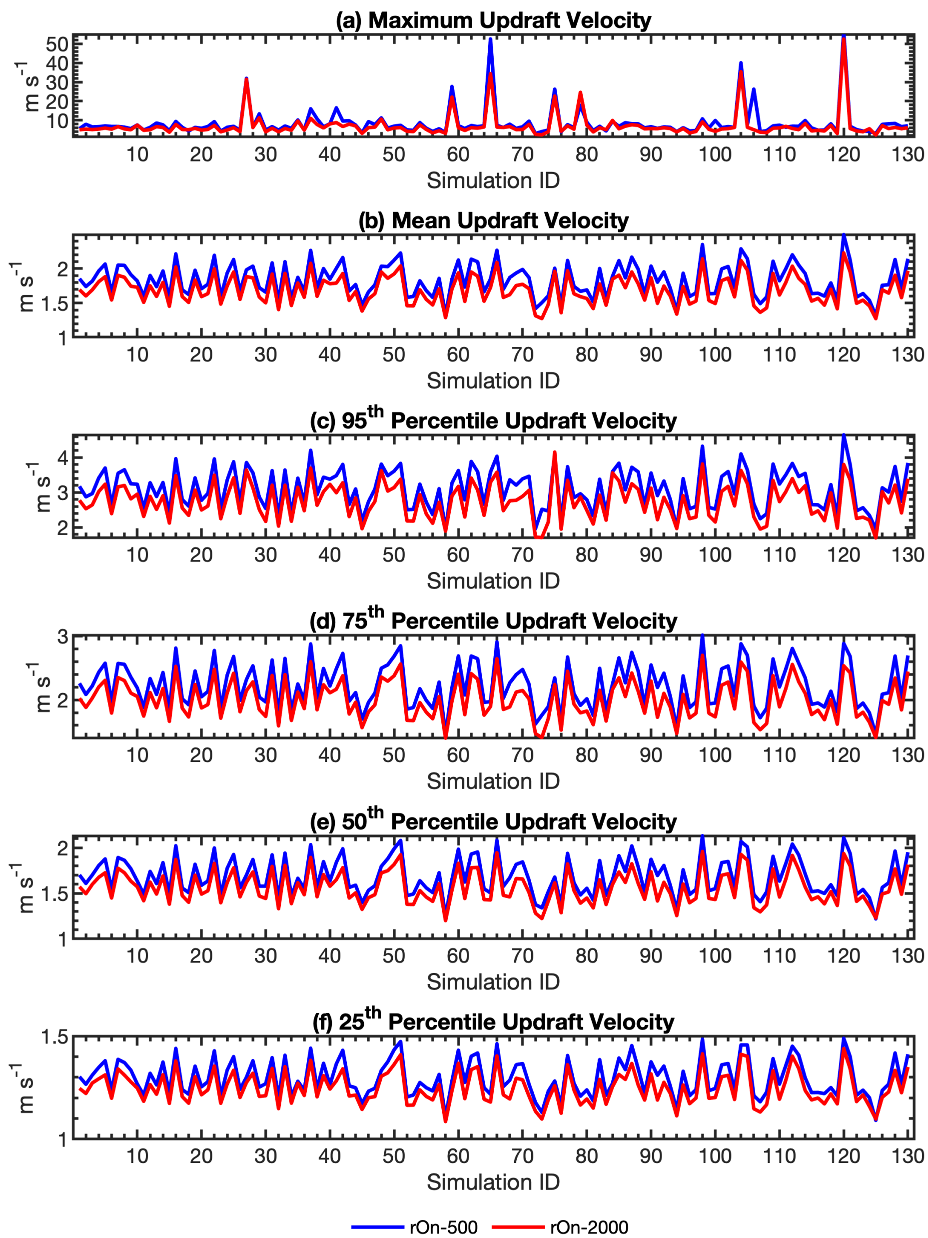

Figure 3.7. The (a) maximum, (b) mean, (c–f) 95, 75, 50, and 25th percentile of updrafts velocities greater than 1 m s^{-1} over land between 1200–1800 LT in rOn-500 (blue) and rOn-2000 (red) ensembles.

In the following subsections, we seek to determine whether the key environmental parameters identified in Park et al. (2020) as the predominant parameters driving the convective updrafts in rOn-500 are impacted by aerosol loading, and if so, why that is the case. We first examine the shallow and deep convective modes of the sea breeze-initiated convection, followed by the shallow boundary layer convection developing ahead of the sea breeze front. We examine these two modes separately as they are driven by different processes, with convergence along the sea breeze front being critical to the sea breeze induced convection, and boundary layer mixing driving the convection developing ahead of the sea breeze.

3.5.2.1 Sea breeze-initiated convective updrafts

When examining rOn-500, Park et al. (2020) found a sharp transition between the shallow and deep sea breeze-initiated convection, marked by large gradients in the maximum updraft velocity, which are a strong function of the initial boundary layer potential temperature. Due to the abrupt vertical velocity gradients between the shallow and deep convective modes, constructing a statistically robust emulator for the maximum updraft velocities was unfortunately not feasible. The same was found to be true here for the rOn-2000 simulation, and thus we have had to rely on other methods of analysis for the convective updraft velocities along the sea breeze front.

As shown in Figure 3.8a, the shallow and deep convective regimes are separated by initial boundary layer potential temperatures of 297 K for rOn-500. In other words, all of the deep convection simulations in the pristine ensemble have an initial boundary layer potential temperature greater than or equal to 297 K as a common characteristic. This temperature threshold is related to the control of the initial boundary layer potential temperature on mixed-layer CAPE (Park et al., 2020). Examining the same transition between the shallow and deep modes in the polluted ensemble, the transition is still evident (Figure 3.8b). However, the deep convection in the polluted ensemble now only occurs when the initial boundary layer potential temperature is greater than 299 K, 2 K greater than those in rOn-500. As demonstrated above, the surface temperatures are reduced in the presence of enhanced aerosol loading in the rOn-2000 ensemble. Therefore, greater initial boundary layer potential temperatures are necessary to offset the aerosol-induced surface cooling in the polluted ensemble, as this provides sufficient environmental CAPE to support the production of deep convection along the sea breeze front.

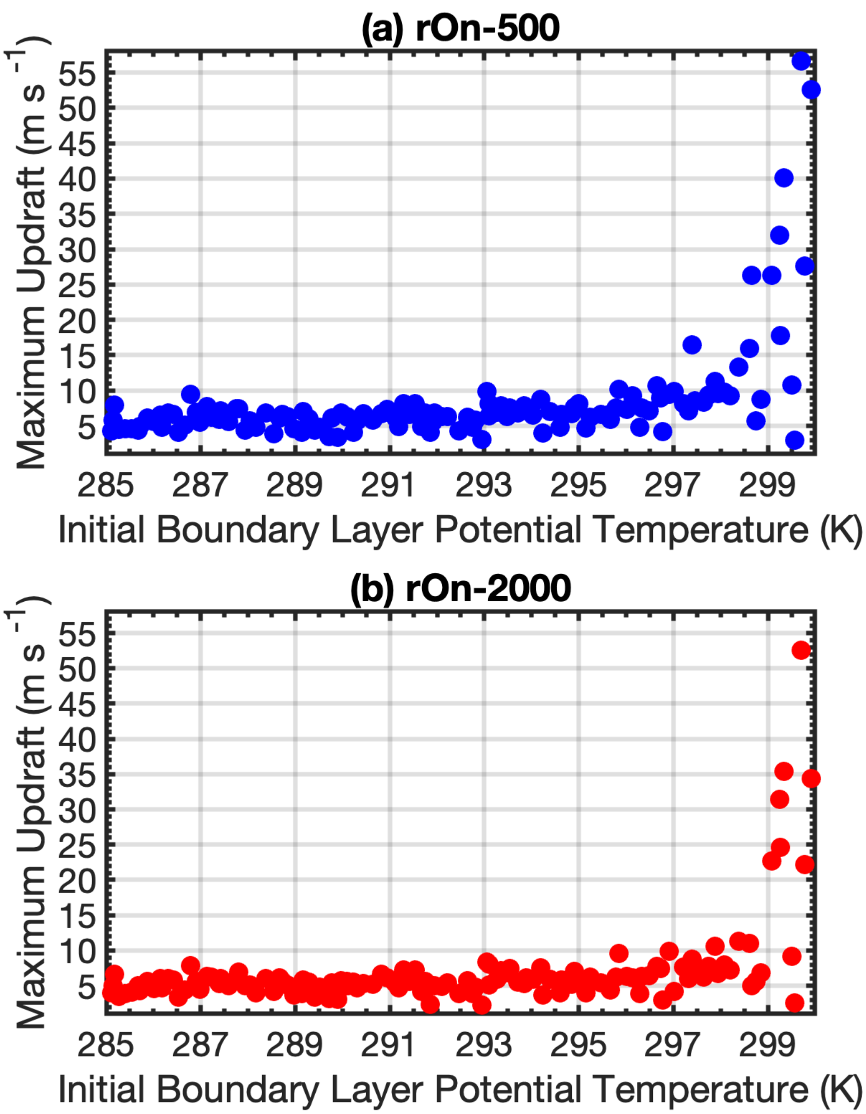

Figure 3.8. Pairwise scatterplots of the maximum updraft velocities versus the initial boundary layer potential temperature for the sea breeze induced convection for (a) rOn-500 and (b) rOn-2000

3.5.2.2 Boundary layer convective updrafts

The boundary layer convective clouds developing ahead of the sea breeze are now examined. Unlike the sea breeze-initiated convective updrafts, constructing a robust emulator was possible for the mean updraft velocities of the boundary layer convection, and we can therefore draw on the emulator results in our analysis of the cloud updrafts. The bar graphs in Figures 3.9a (rOn-500) and 3.9b (rOn-2000) indicate how much of the variance in the median updraft velocity is explained by individual perturbations to the ten environmental parameters tested. Each stacked bar graph's height refers to the summation of first-order contributions from the ten parameters to the median updraft velocity. Any blank space remaining above the bar indicates the contributions made by higher-order nonlinear interactions involving multiple parameters.

It is evident from the first bar graph (labelled "Overall") in Figures 3.9a and 3.9b that the same two parameters, the soil saturation fraction (dark gray) and the inversion layer strength (pink), are the predominant contributors to the updraft velocities in rOn-500 and rOn-2000, although their percentage contributions differ. We first examine the role of these two parameters on the boundary layer convection in rOn-500 before analyzing the impacts of aerosol loading. Figures 3.9c and 3.9d present the mean responses of the emulator-predicted median updraft velocities to the soil saturation fraction and inversion layer strength. It is clear from these figures that drier soils and a weaker inversion layer promote more vigorous boundary layer convection.

Interestingly, the sensitivity of the median updraft velocities to the soil saturation fraction (Figure 3.9c) shows three distinctive regimes: (1) moderate velocity changes for soil saturation fractions between 0.1–0.4; (2) large velocity changes for soil saturation fractions between 0.4–0.6; and (3) neutral velocity responses for soil saturation fractions between 0.6–0.9. We will refer to these three regimes as the DRY, MID, and WET soil moisture regimes, respectively. The corresponding variance-based sensitivity analyses for the boundary layer convection over these three different soil regimes are also presented in Figures 3.9a and b (second to fourth bar graphs).

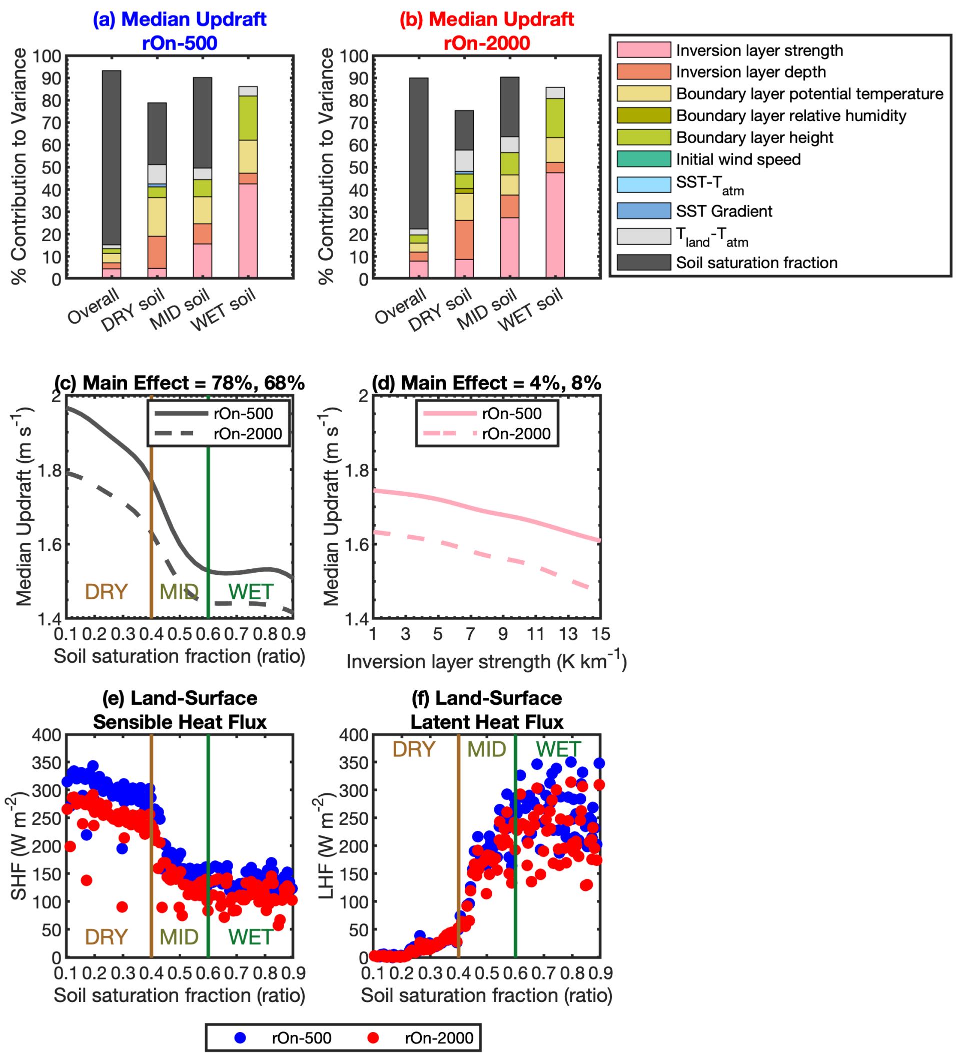

Figure 3.9. Percentage contribution to the variance of median updraft velocities in (a) rOn-500 and (b) rOn-2000, caused by each of the 10 environmental parameters of interest over the entire parameter space range (first stacked bar graphs), and then over the DRY, MID, WET soil regimes (second to fourth stacked bar graphs). Mean responses of the median updraft velocities to the two-most important parameters, (c) soil saturation fraction and (d) inversion layer strength. Solid and dashed lines in (c) and (d) indicate mean responses of median updraft velocities of rOn-500 and rOn-2000, respectively. The numbers at the top of each plot in (c) and (d) indicate the percentage contribution of each parameter to the output variance. (e) Pairwise scatter plots of land-averaged surface sensible heat flux between 1200–1800 LT (W m^{-2}) and soil saturation fraction. Blue and red colors indicate rOn-500 and rOn-2000, respectively. (f) is the same as (e) but for land-averaged latent heat flux (W m^{-2}). Note that 130 data points in (e) and (f) have different values for the ten perturbed environmental parameters.

In order to understand the updraft velocity responses in the soil moisture regimes, one needs to note that the soil saturation fraction value of 0.4, which separates the DRY and MID soil moisture regimes, corresponds to the permanent wilting point (the minimum amount of soil moisture that a plants' roots require in order not to wilt) of sandy clay loam soil. Below the permanent wilting point, the vegetation becomes stressed, resulting in a suppression of transpiration and hence the release of moisture. Therefore, in the DRY soil regime (0.1–0.4), where the soil moisture falls below that of the permanent wilting point, the surface latent heat flux is suppressed, while the surface sensible heat flux increases as more of the surface heating goes into the sensible heat fluxes. The relatively strong sensible heat fluxes in the DRY regime contributes to the stronger updraft velocities observed in this regime (Figure 3.9e).

Over the WET soil regime (0.6–0.9), the abundant evaporation and transpiration, the surface sensible heat flux is reduced and the surface latent heat flux is enhanced (Figures 3.9e and 3.9f). Furthermore, the surface sensible heat flux is no longer sensitive to the soil saturation fraction, as is evident in the flat gradient of the curve in Figure 3.9c, as well as in the absence of the soil saturation fraction contributions to the WET regime in Figures 3.9a and 3.9b (fourth bar graph ("WET soil").

In the MID soil regime, both the sensible and latent heat fluxes show the most sensitive response to the soil saturation fraction (Figure 3.9e and 3.9f). While the curves of median updraft velocities (Figure 3.9c) and surface sensible heat flux (Figure 3.9d) are similar in trend to those over the DRY soil regime, the slopes are steeper in the MID soil regime. As such, the relative importance of the soil saturation fraction is greatest in the MID soil regimes compared with the DRY or WET soil regimes (second to fourth bar graphs in Figures 3.9a and 3.9b). Such nonlinear convective responses to soil saturation fraction have also been discussed in Drager et al. (2020).

We now turn to the impacts of enhanced aerosol loading on the roles of the soil saturation fraction and the inversion layer strength. When comparing Figure 3.9a with 3.9b, the relative percentage contribution of soil saturation fraction decreases with enhanced aerosol loading from 78% to 68%, whereas that of the inversion layer strength increases from 4% to 8%. The soil saturation fraction plays an important role in boundary layer convection through its control of the magnitude of the surface sensible and latent heat fluxes, as well as the partitioning between them. As discussed in Section 3.3.4, the reduction in surface downwelling shortwave radiation in the polluted ensemble reduces the surface longwave emission and associated surface sensible and latent heat fluxes and the mixed layer depth. The reduction in the percentage contributions of the soil saturation fraction to the updraft velocities in the polluted ensemble therefore reflects this reduced role of the surface fluxes and boundary layer mixing in driving the updrafts.
Comparing the emulator-predicted median updraft in rOn-500 and rOn-2000 (Figures 3.9c and 3.9d), and hence between the pristine and polluted conditions, the trends in the relationship between the soil saturation fraction and the updraft velocities are the same, but median updrafts are stronger in rOn-500 due to the stronger sensible heat fluxes. From rOn-500 to rOn-2000, the relative importance of soil saturation fraction on the median updraft is reduced in the DRY and MID soil regimes while it is absent in WET soil regimes regardless of aerosol loading.

3.5.3 Surface accumulated precipitation

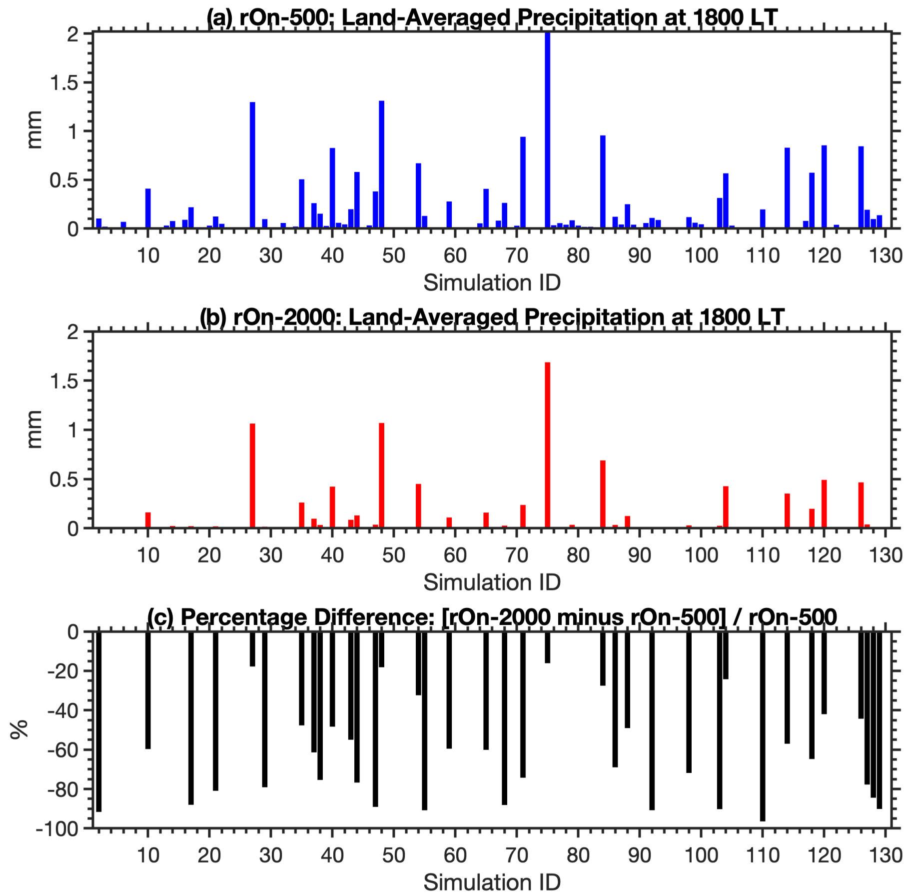

Figure 3.10. (a) Land-averaged surface accumulated precipitation at sunset (1800 LT) from 130 ensemble members from rOn-500 (blue bars) and (b) rOn-2000 (red bars); and (c) percentage difference between rOn-500 and rOn-2000 for simulations that produce at least 0.1 mm of the land-averaged accumulated precipitation in rOn-500.

The changes in surface accumulated precipitation as a function of increased aerosol loading are now analyzed. Figures 3.10a and 3.10b display land-averaged surface accumulated precipitation at 1800LT in rOn-500 and rOn-2000, respectively. The impact of enhanced aerosol loading on precipitation is represented by the percentage differences between rOn-2000 from rOn-500 (Figure 3.10c). The percentage differences are only determined for those simulations that produce at least 0.1 mm of the land-averaged accumulated precipitation in rOn-500 (36 out of 130 simulations). Only 19 simulations produced more than 0.1 mm of precipitation in both rOn-500 and rOn-2000. No simulation in rOn-2000 produces more than 0.1 mm of precipitation that does not produce more than 0.1 mm of precipitation in rOn-500. It is clear from Figure 3.10 that the accumulated precipitation is reduced in all 36 simulations of the rOn-2000 simulations when compared with their corresponding counterparts in rOn-500, with the percentage differences varying from 16% (Test75) through 97% (Test110).

Examining the most noticeable differences in the initial conditions of these two extreme cases provides some insights into the environmental controls. Test75, which demonstrates the least reduction in precipitation between the pristine and polluted cases, has a very moist, warm and deep lower troposphere that develops in association with the soil saturation fraction of 0.89, boundary layer relative humidity of 89.8% and boundary layer potential temperature of 299 K. On the other hand, Test104, which shows the greatest difference between the pristine and polluted cases, has only moderately moist and warm initial conditions with soil saturation fraction of 0.44, boundary layer relative humidity of 84.2%, and boundary layer potential temperature of 288 K. The warmer, moister conditions in Test75 will more effectively limit the impacts of evaporation on the aerosol-induced shifts to more numerous, smaller cloud and rain drops, therefore reducing the impacts of aerosols on the surface accumulated precipitation in this test.

The results from these two extensive ensembles with 130 different initial conditions, each being representative of the range in conditions commonly associated with tropical sea breeze systems, therefore suggest that enhanced aerosol loading results in decreasing the precipitation produced by sea breeze convection irrespective of the environmental conditions, but that the magnitude of the aerosol-induced precipitation reduction varies from one member pair to the next member pair, and hence is a function of the environment. Therefore, while the decreasing trend of precipitation as a result of enhanced aerosol loading is robust, independent of environment, the magnitude of the reduction is environmentally modulated.

3.6 Impacts of eliminating aerosol-radiation interactions

In this final section, we now investigate the impacts of aerosol indirect effects on the deep convective development independently, by examining rOff-500 and rOff-2000 in which aerosol-radiation interactions have been eliminated. As described earlier, 12 ensemble members of rOn-500, with 12 different initial environments produced deep convection in association with the sea breeze convergence. Also, as previously noted, rOn-500 and rOn-2000 differ only in their aerosol loading, and the aerosol particles are both radiatively and microphysically active. The 12 ensemble members of rOff-500 and rOff-2000 correspond to those of rOn-500 and rOn-2000, respectively, except that the aerosol particles in the former two ensembles cannot interact with radiation. Comparing the 12 corresponding deep convection simulations in these four smaller ensembles of different aerosol conditions, therefore, allows us to examine convective cloud responses to aerosol loading, and to aerosol direct and indirect effects.

3.6.1 Suppressed deep convective development in rOn-2000

Of the 12 deep convective cases in rOn-500 (Tests 27, 29, 37, 41, 59, 65, 75, 59, 100, 104, 106, and 120), 5 of the corresponding cases of rOn-2000 (Tests 29, 37, 41, 100, and 106) do not form deep convection. Figure 3.11 displays the updraft velocities greater than 1 m s^{-1} averaged over land between 1200–1800 LT. It is evident from Figures 3.11a–e that no updrafts develop above 7 km AGL in rOn-2000 (as indicated by the red lines). This is in keeping with the absence of deep convective clouds (cloud top height > 7 km) for the same 5 cases (Figure 3.12d).

This also suggests that the enhanced aerosol loading in rOn-2000 has suppressed the development of deep convection. The question now is whether this is due to aerosol direct effects, aerosol indirect effects, or some combination of both, and how the environment may impact or modulate these responses?

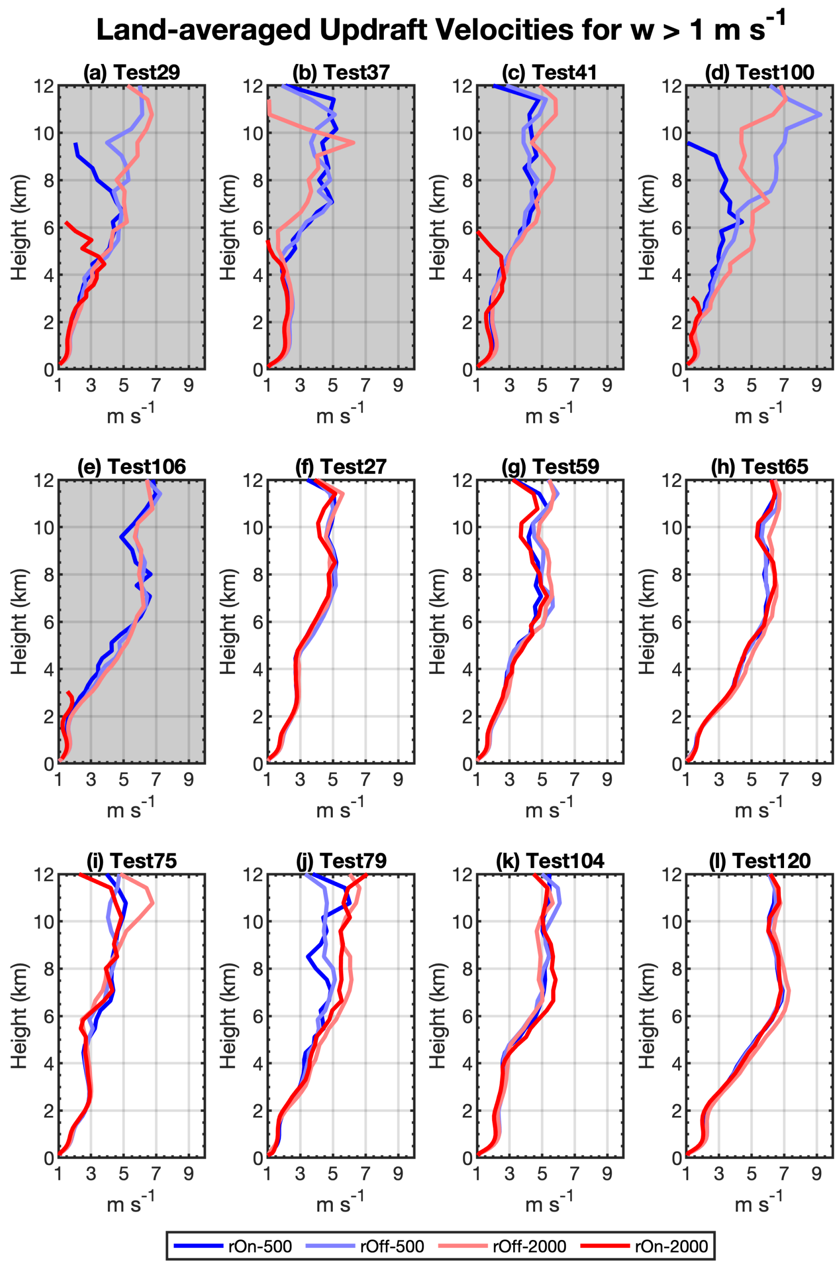

Figure 3.11. Vertical profiles of updraft velocities greater than 1 m s^{-1}, averaged over land during 1200–1800 LT. The gray shading indicates those ensemble members where deep convection does not develop in rOn-2000 (red lines).

To understand the potential role played by the environment for those simulations that fail to produce deep convection in rOn-2000, we start by examining the initial conditions of the 12 deep convective simulations. Table 3.3 displays the values of the ten environmental parameters that comprise the initial conditions for the 12 deep convective cases in rOn-500. The table is grouped so that those simulations that do not produce deep convection in rOn-2000 are listed in the table's top section. It is worth remembering that the initial conditions are the same for each corresponding pair of simulations in rOn-500 and rOn-2000, with the only differences being the aerosol loading. It is evident from Table 3.3, that deep convection only develops in rOn-2000 when the initial boundary layer potential temperature (fourth column in Table 3.3) is warmer than 299 K, whereas deep convection develops in rOn-500 when the initial boundary layer potential temperature is greater than 297 K. This is in keeping with our findings in Section 3.5.2.1. Other than the initial boundary layer potential temperature, there are no other apparent trends in the differences of the initial conditions. It therefore appears that the failure to produce deep convection in ensemble members 29, 37, 41, 100, and 106 is directly related to the initial boundary layer potential temperature.

Table 3.3. Ten input environmental parameter value combinations for 12 cases producing deep clouds (i.e., cloud top height > 7 km) in rOn-500.

Deep convection?		Parameter / ID	Boundary layer			Inversion layer		Wind	Land surface		Sea surface	
rOn-500	rOn-2000		Potential temperature	Relative humidity	Height	Strength	Depth	Speed	$T_{land} - T_{atm}$	Soil saturation fraction	SST$-T_{atm}$	SST Gradient
Yes	No	29	298.4	87.9	272.1	5.4	339.4	−0.50	0.9	0.71	6.5	−0.0103
		37	298.6	89.2	874.0	11.5	222.3	−0.37	7.2	0.27	6.3	0.0067
		41	297.4	80.0	248.2	9.0	610.7	−4.07	1.6	0.28	5.7	0.009
		100	297.0	87.5	579.7	10.9	906.2	−3.10	2.2	0.48	9.7	−0.013
		106	298.6	79.9	115.1	9.2	821.5	1.82	2.0	0.47	4.0	−0.0086
	Yes	27	299.2	82.6	701.7	4.2	392.9	−3.72	7.8	0.68	4.4	0.0081
		59	299.8	76.2	381.2	4.8	781.9	−1.12	3.4	0.57	−4.6	−0.0064
		65	299.9	84.0	160.3	5.7	900.2	4.95	2.3	0.84	7.8	−0.0046
		75	299.1	89.8	786.4	2.3	503.6	0.02	6.5	0.89	−9.2	−0.0196
		79	299.3	89.3	134.0	14.3	119.3	4.68	0.2	0.73	−1.6	−0.0036
		104	299.3	88.5	780.1	14.4	290.7	−3.53	5.9	0.26	4.6	−0.0191
		120	299.7	92.4	423.6	12.6	463.9	−4.98	8.8	0.41	−4.9	0.0006

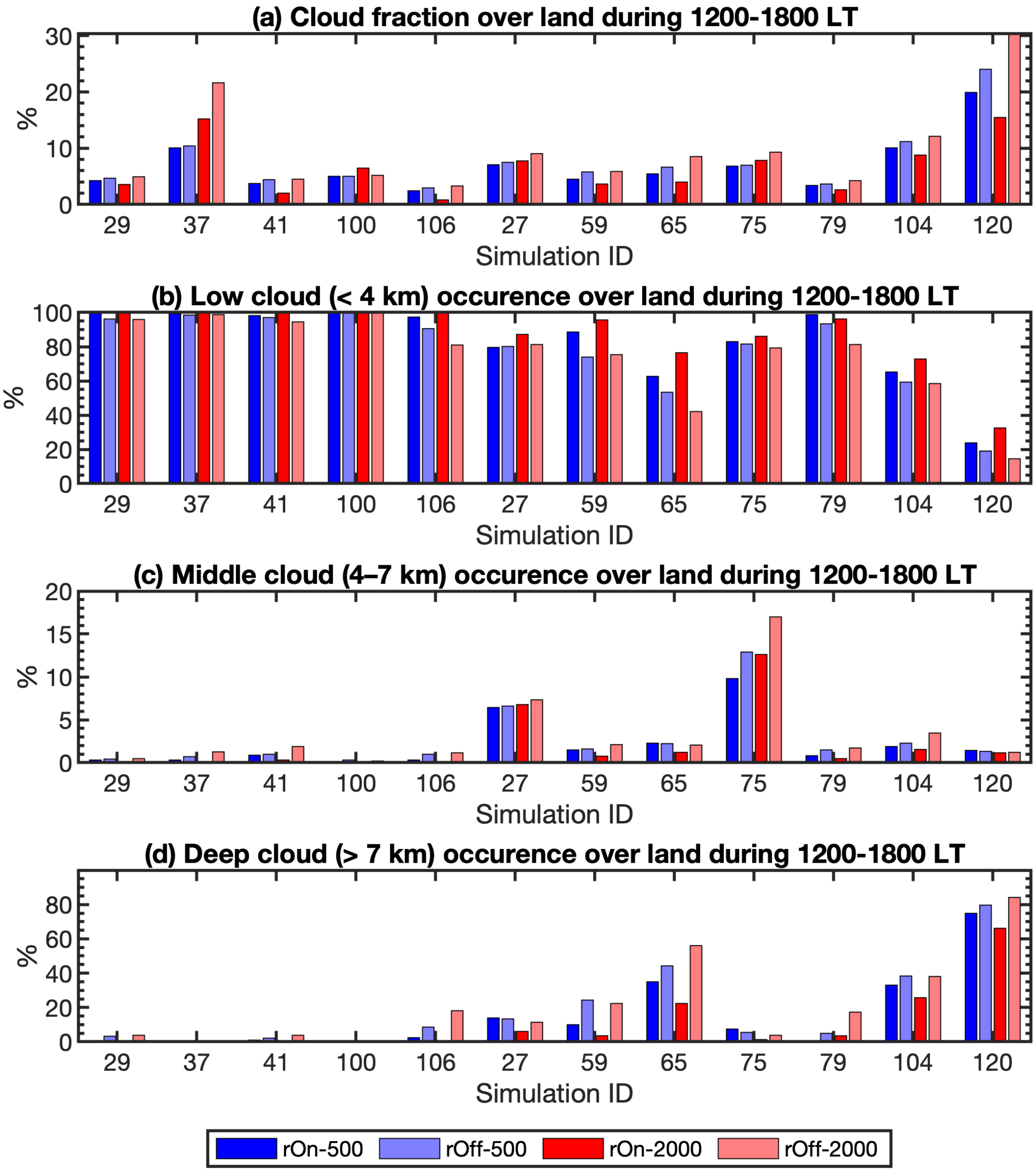

Figure 3.12. Cloud frequency distribution for the 12 ensemble members of rOn-500 that produce deep convection (blue), and their corresponding simulations in rOn-2000 (red), rOff-500 (light blue), and rOff-2000 (light red).

3.6.2 Impacts of enhanced aerosol loading on convective updrafts

In this section, we now examine the impacts of enhanced aerosol loading on the updraft velocities by comparing the averaged updraft velocity responses from (1) rOn-500 versus rOn-2000 and (2) rOff-500 versus rOff-2000. The former comparison presents the synergistic impacts of aerosol direct and indirect effects, while the latter enables us to isolate the role of aerosol indirect effects. Figures 3.11 through 3.14 facilitate these comparisons. In Figure 3.11, the land-averaged updrafts for all 4 ensembles (using only the 12 deep convection simulations in rOn-500 and rOn-2000) are computed for grid points where the vertical velocities are greater than 1 m s^{-1} between 1200–1800 LT. Figure 3.12 shows the cloud frequency distribution for each ensemble member from the four ensembles. Figure 3.13 and Figure 3.14 demonstrate the percentage differences between the land-averaged updraft velocities for the 12 members from rOn-500 and rOn-2000 and from rOff-500 and rOff-2000, respectively.

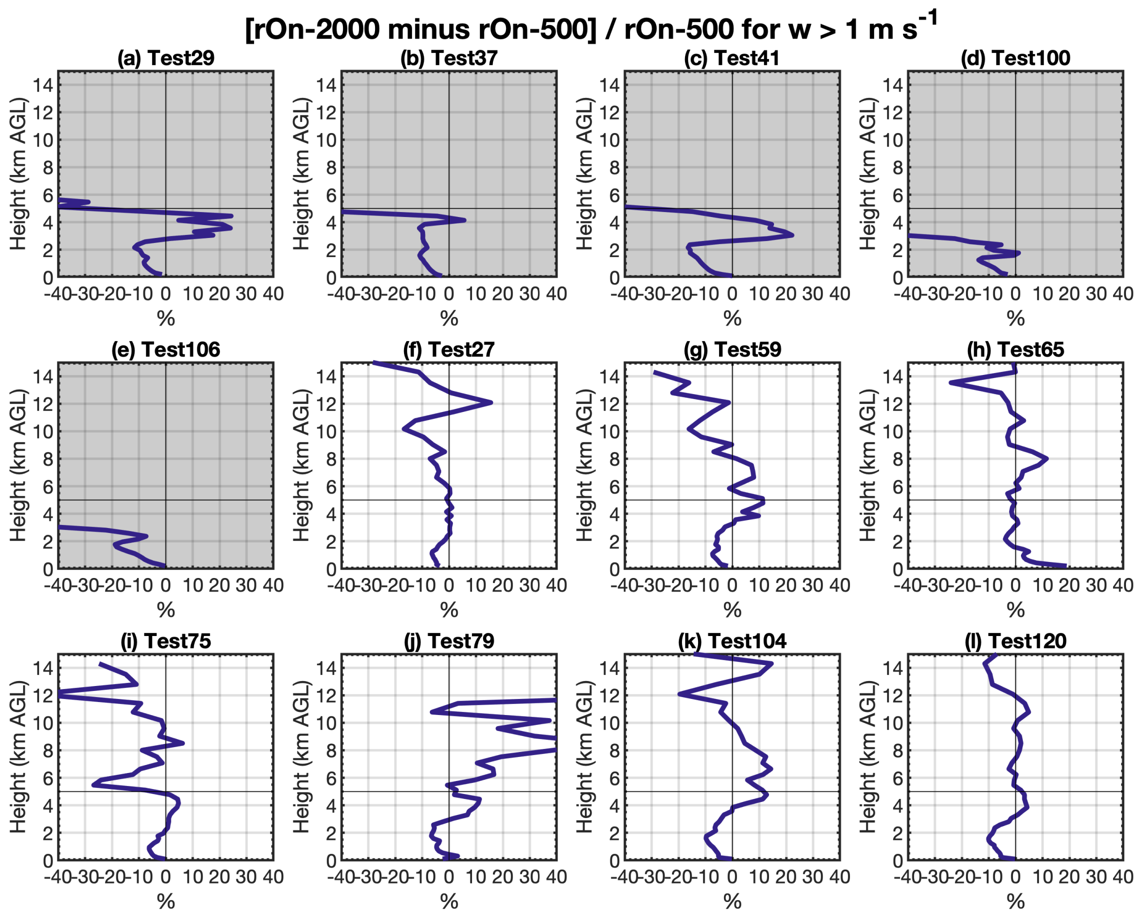

Figure 3.13. Vertical profiles of the percent difference between the convective updraft velocities in rOn-500 and rOn-2000, where the updraft velocities are averaged over land for updrafts greater than 1 m s^{-1}. Gray shadings indicate those simulations where deep convection does not develop in rOn-2000. Horizontal black lines indicate the location of the freezing level. Vertical black lines represent 0% difference between the convective updraft velocities in rOn-500 and rOn-2000. Note that the x-axis scale is limited between −40 and 40% to show the differences in the warm phase regions (below 5 km AGL).

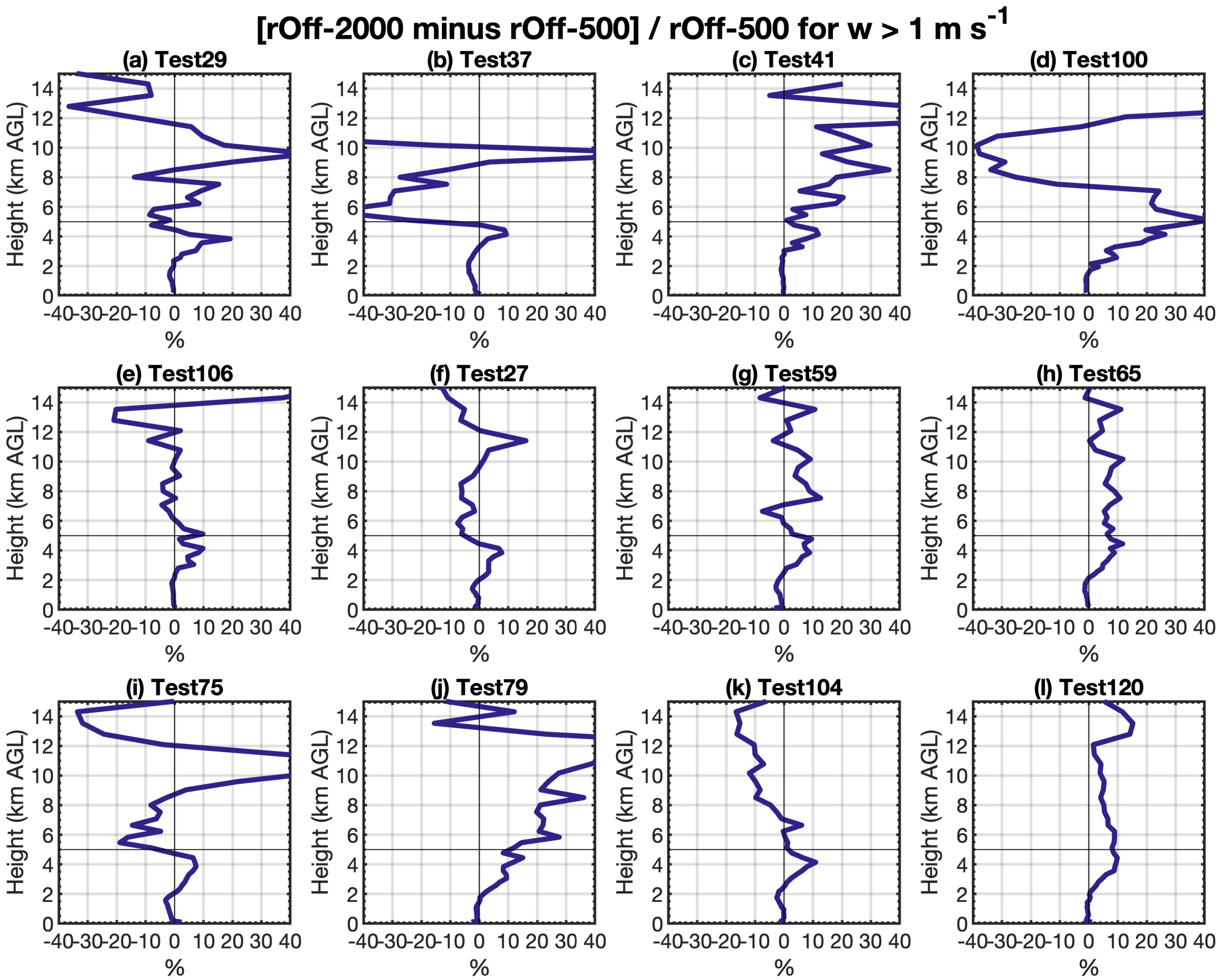

Figure 3.14. Same as Figure 13 but for rOff-500 and rOff-2000.

When comparing the impacts of aerosol loading on convective updrafts with aerosol-radiation effects turned on, the absence of deep convective updrafts in 5 of the 12 simulations of rOn-2000 when compared with rOn-500 is evident in Figure 3.13a–e. For the remaining 7 cases that do produce deep convective updrafts in both rOn-500 and rOn-2000, the vertical profiles of the percentage differences in updraft velocities above the freezing level as a function of aerosol loading vary from case to case, with some showing negative percentages while others have positive percentage differences (Figure 3.13f–l).

Similarly, below the freezing level, mixed responses in aerosol loading impacts on the updraft velocities are also evident. This lack of consistent trends in updraft velocities is therefore true both for condensational or warm phase invigoration (1–5 km AGL) and for the cold phase invigoration, and is evident for both the 1m s^{-1} and 5 m s^{-1} (not shown) thresholds. This result implies that when both direct and indirect aerosol effects are accounted for, which is the situation most representative of reality, that increases in aerosol loading may either increase, decrease or produce little response in the convective updrafts, and that warm and cold phase convective invigoration, or the lack thereof, is modulated by the environment. It should be pointed out that convection here refers to the overall sea breeze convection and includes both the shallow and deep convective modes.

Now comparing rOff-500 and rOff-2000, in which the aerosol-radiation interactions are turned off, the direct aerosol effect has been eliminated, thus allowing us to assess the extent of the aerosol indirect effects on the sea breeze convection. Several interesting trends are evident:

1. All 12 simulations in both rOff-500 and rOff-2000 produce deep convection (light blue and light red lines, Figure 3.11). Also, comparing the corresponding simulations in rOn-2000 (red lines, Figure 3.11a–e) and rOff-2000 (light red lines, Figure 3.11a–e), the 5 simulations that did not deep convection in rOn-2000 do generate deep convection in rOff-2000 when aerosol-radiative interactions are turned off. This demonstrates the importance of the aerosol direct effects, which, as we have already seen, can produce suboptimal convective conditions in environments that might otherwise be marginally supportive of convection. The environment therefore modulates the potential severity of the impacts of the direct effects on sea breeze convection. These results also highlight the importance of allowing the radiation to interact directly with both aerosol particles and microphysical hydrometeors, and hence including both the direct and indirect effect when examining aerosol impacts on deep convection.

2. It is evident from Figure 3.14 that in the warm phase regions (below 5 km AGL) of the convection, the updrafts are stronger in every one of the 12 rOff-2000 simulations compared with their corresponding counterparts in rOff-500, showing 7% through 42% velocity enhancements. In other words, in the absence of aerosol-radiative effects, the enhanced aerosol loading within rOff-2000 produces stronger updrafts than those in rOff-500 within the warm phase regions of the convection, irrespective of the initial environmental conditions. These warm phase trends remain consistent when the updrafts are thresholded by 5 m s^{-1}, although the differences are smaller in magnitude (not shown). The associated aerosol-induced changes to the mass and number concentrations of cloud water, averaged over land between 1200–1800 LT for grid points where updraft velocities are greater than 1 m s^{-1}, are shown in Figure 3.15. In all 12 cases, rOff-2000 produces a greater number of cloud droplets and more cloud water mass below the freezing level, in keeping with the current theories on aerosol indirect effects. Accordingly, more latent heating via enhanced condensation rates occurs in the warm phase for all 12 simulations of rOff-2000 (Figure 3.16), clouds become more buoyant, and the updrafts within the warm phase become invigorated. Given that 12 cases have different environmental conditions, our results suggest that condensational or warm-phase invigoration of the updrafts are robust in the absence of aerosol direct effects, occurring independent of the environment, and hence are not environmentally modulated within these multiple tropical sea breeze environments.
3. The updraft velocity responses above 5 km AGL to enhanced aerosol loading vary between the pairs of rOff-500 and rOff-2000 simulations (Figure 3.14), being at times weaker and at other times stronger with enhanced aerosol loading. The lack of consistent

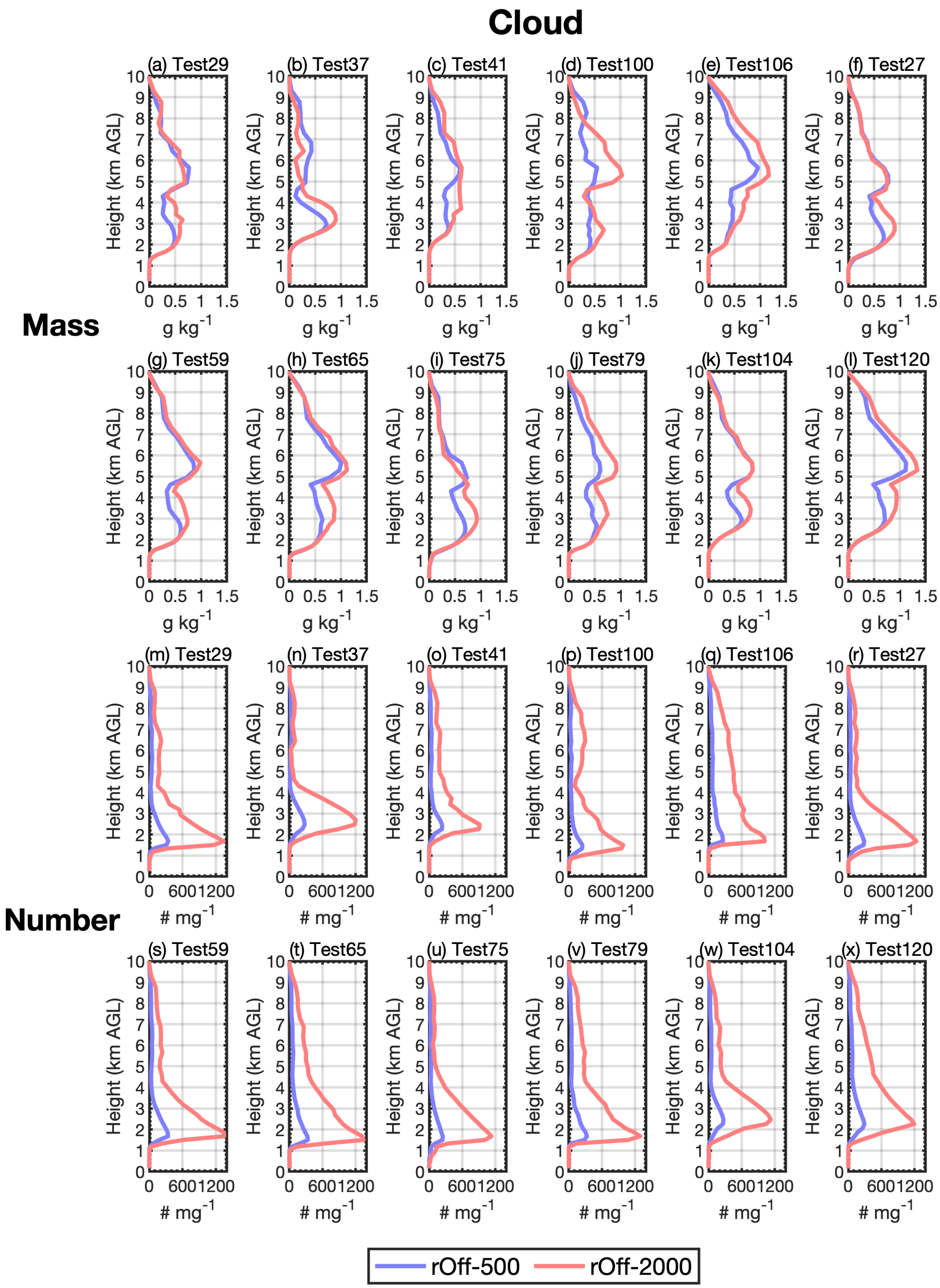

Figure 3.15. Vertical profiles of the mixing ratios (g/kg) of cloud mass (top two rows) and number concentration (mg^{-1})(bottom two rows), averaged over land during the afternoon for grid points where updraft velocities > 1 m s^{-1}, for rOff-500 (light blue) and rOff-2000 (light red).

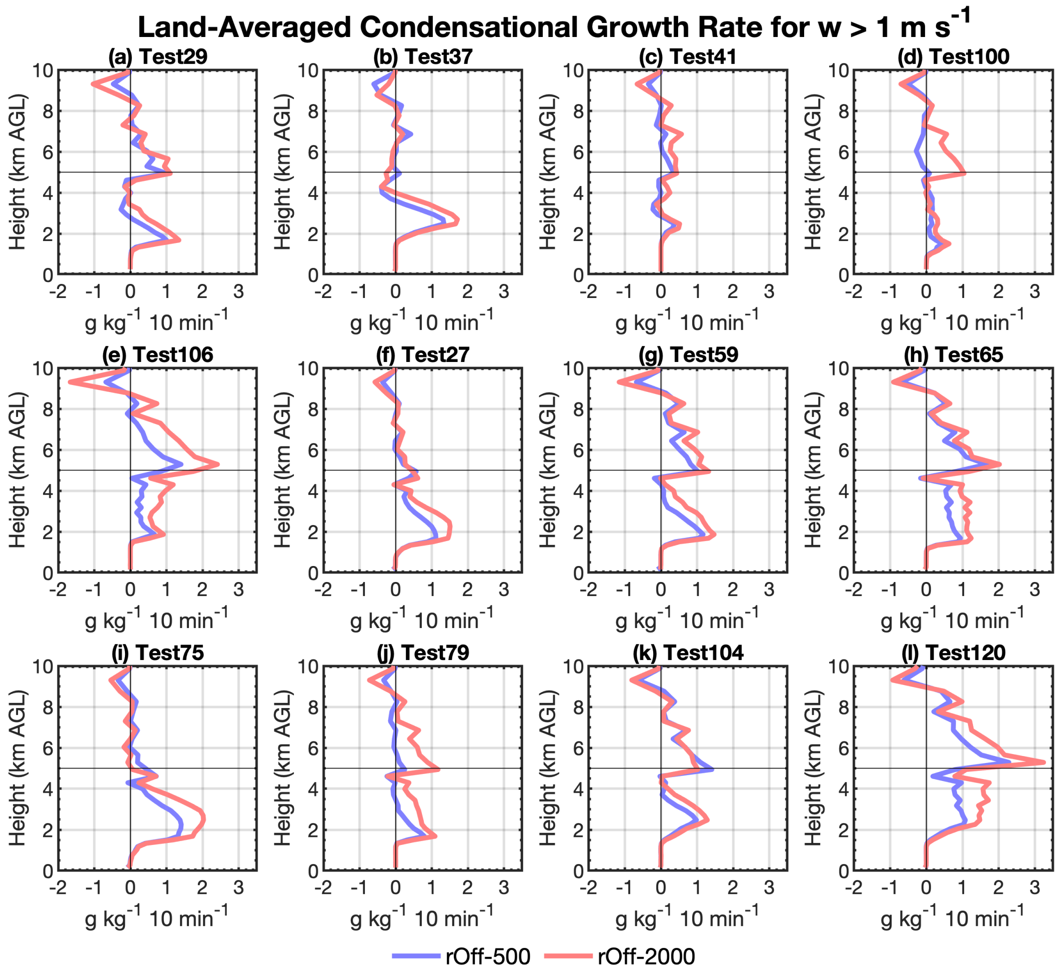

Figure 3.16. Vertical profiles of the net evaporation and condensation growth rates (g kg^{-1} 10 min^{-1}), averaged over land during the afternoon for grid points where updraft velocities > 1 m s^{-1}, for rOff-500 (light blue) and rOff-2000 (light red).

trends in the updraft velocities in the mixed-phase regions is also evident in the trends in the mass mixing ratios of the dense (graupel and hail) and less dense (pristine ice, snow, and aggregates) (Figure 3.17) ice species. Therefore, while increased aerosol loading may be associated with stronger mean updraft velocities under some conditions, the mean updraft velocities may be weaker or show little change under other environmental conditions. These results therefore imply that the environmental conditions modulate the impacts of increased aerosol loading on updraft velocities within the mixed phase regions of the cloud when aerosol-radiation interactions are turned off, and that the updrafts may be weaker, stronger, or show little change depending on the environment. This environmental modulation of the impacts of enhanced aerosol loading on cold phase invigoration therefore occurs whether aerosols are allowed to interact with radiation (as discussed above) or whether they are not, as shown here.

3.6.3 Precipitation

Figures 3.18a, b, d, and e show the land-averaged accumulated surface precipitation at sunset (1800 LT) for each of the 12 simulations in rOn-500, rOn-2000, rOff-500, and rOff-2000, respectively. We have already discussed above (Section 3.5.3) the reduction in precipitation from rOn-500 to rOn-2000 due to enhanced aerosol scattering of the radiation, and which is once again also evident the limited subset of 12 simulations shown here (Figures 3.18a and 3.18b). A similar reduction in precipitation with enhanced aerosol loading is not found in the comparison between rOff-500 and rOff-2000 when radiation is not allowed to interact with aerosols (Figures 3.18d and 3.18e). In some cases, the accumulated precipitation is enhanced, while in other cases it is reduced or remains neutral, when the aerosol loading is increased. These results indicate two

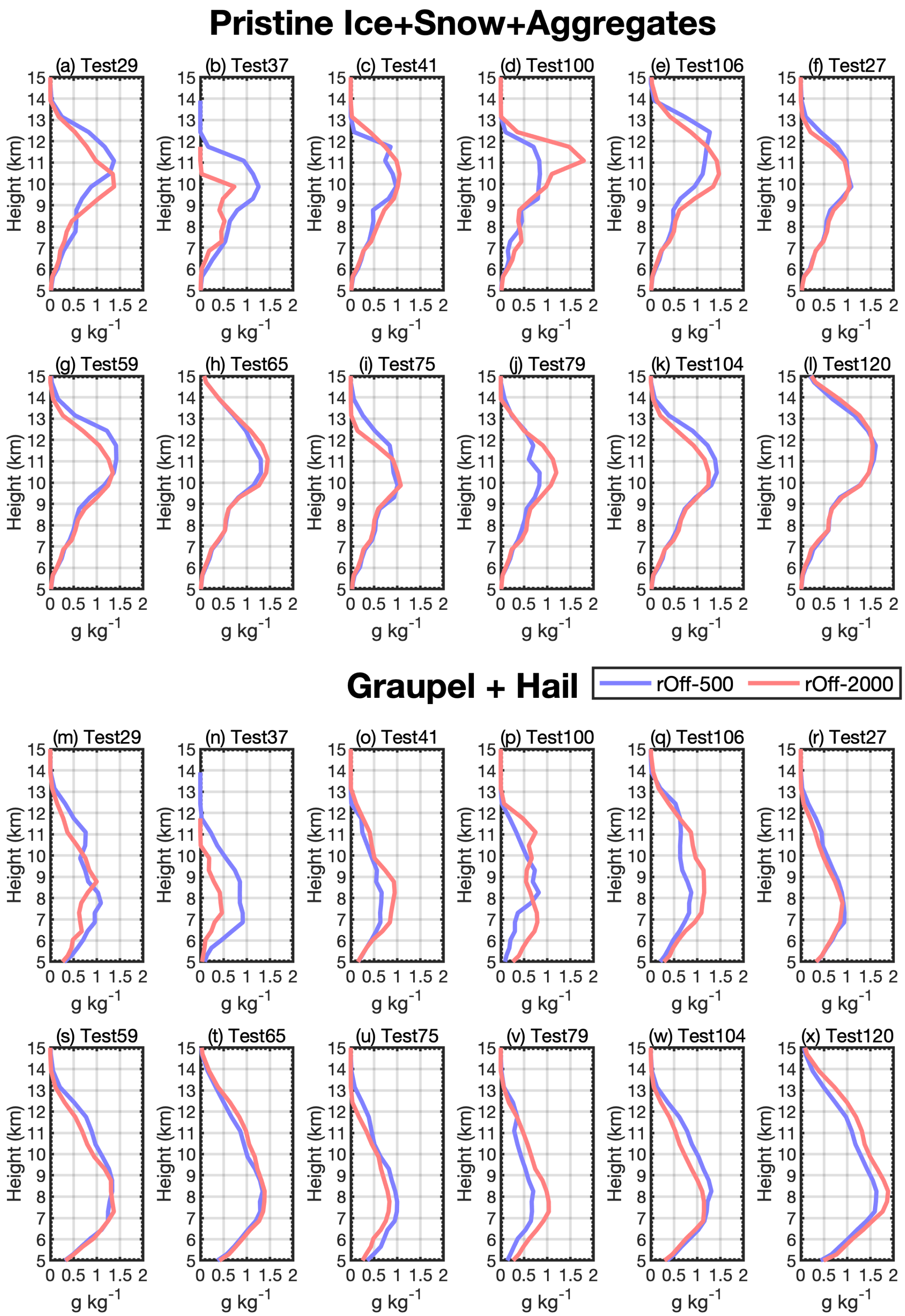

Figure 3.17. Vertical profiles of mass mixing ratios of less dense (top two panels; pristine ice, snow, and aggregates) and dense (bottom two panels; graupel and hail) averaged over land during the afternoon for grid points where updraft velocities > 1 m s^{-1}, for rOff-500 (light blue) and rOff-2000 (light red).

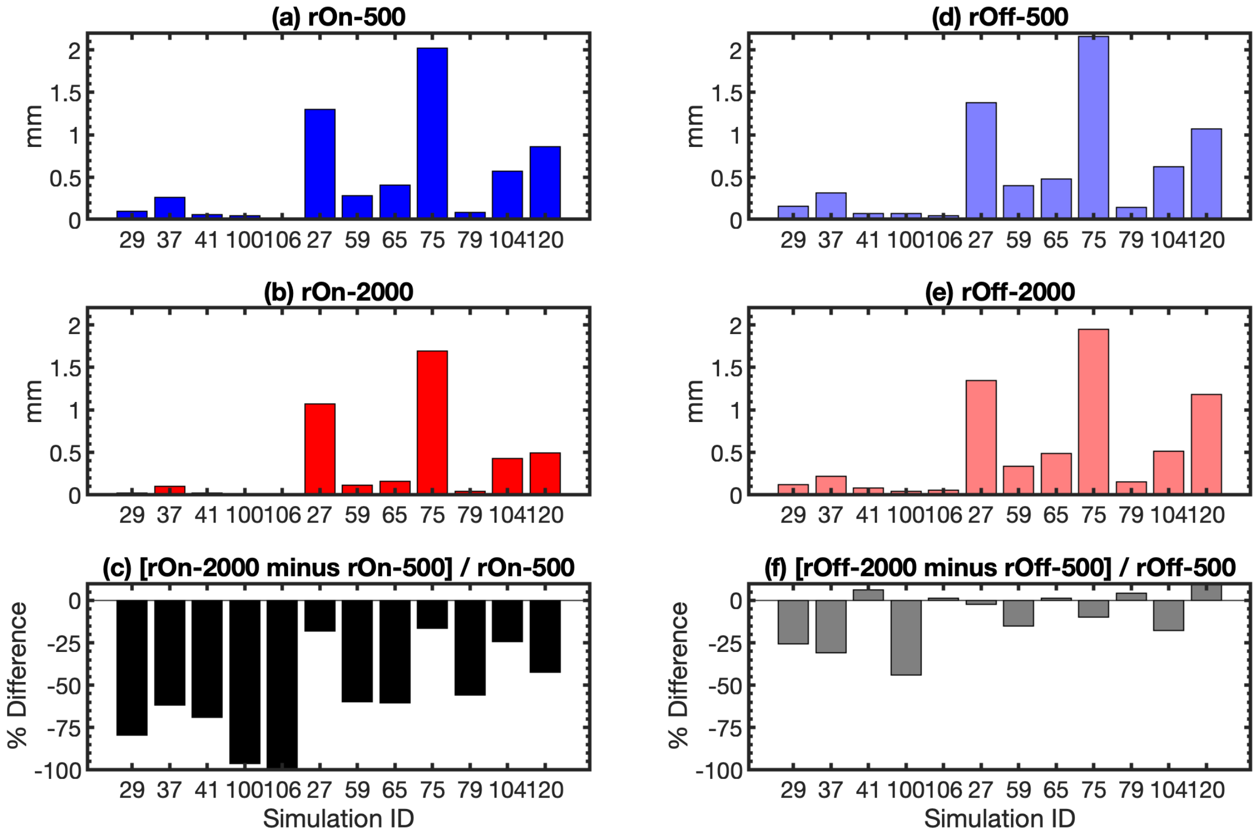

Figure 3.18. Surface accumulated precipitation at sunset (1800 LT) averaged over land for 12 selected cases from (a) rOn-500 (blue), (b) rOff-500 (light blue), (d) rOn-2000 (red), and (e) rOff-2000 (light red). Percentage differences between (c) rOn-2000 and rOn-2000 are in black and those (f) between rOff-2000 and rOff-500 are in grey.

important points. Firstly, that in the absence of aerosol direct effects, the impacts of enhanced aerosol loading on surface precipitation is modulated by the environmental conditions, with increases, decreases and neutral responses all possible under different sea breeze environments. Secondly, when aerosols are allowed to interact with the radiation, while the percentage reduction in surface precipitation is impacted by the environment, the presence of the aerosol direct effects produces a consistent reduction in surface precipitation with increasing aerosol loading, a trend which is not only evident in the 12 simulations shown in Figure 3.18, but also in all 130 pairs of the rOn-500 and rOn-2000 ensembles (Section 3.5.3). It is important to remember that the accumulated precipitation includes the contributions both from the shallow and deep convective modes and these results are therefore applicable to the whole sea breeze convective system, as opposed to just one mode of convection.

Finally, with fixed aerosol loading, the accumulated surface precipitation is greater when aerosol-radiation interactions are absent, i.e., the accumulated precipitation is less in rOn-500 compared with rOff-500, and in rOn-2000 compared with rOff-2000. As discussed in Section 3.4, enhanced aerosol scattering of radiation weakens three convective ingredients, thereby bringing less convectively favorable convective environments and a weakened precipitation response. These results also imply that the precipitation response may be overestimated when aerosol-radiation interactions are not properly accounted for.

3.7 Summary and discussion

The primary goals of this study have been to investigate how microphysically and radiatively active aerosol particles influence tropical over-land convection developing under a wide range of tropical sea breeze flow regimes, and to determine how the environment modulates these aerosol impacts. In order to achieve our goals, we conducted and compared four simulation ensembles: rOn-500, rOn-2000, rOff-500, and rOff-2000. The first two ensembles, rOn-500 and rOn-2000, differed in their aerosol loading and allowed aerosol particles to interact with both radiation and microphysics. They were designed to address the impacts of the enhanced loading of aerosols on tropical over-land convection. Each of these two ensembles contained 130 members initialized with 130 different initial conditions, where ten thermodynamic, wind, and surface properties were simultaneously perturbed. The next two ensembles, rOff-500 and rOff-2000, were carried out to isolate aerosol indirect effects by eliminating the interactions between aerosol particles and radiation (i.e., the aerosol direct effect). Utilizing 12 initial conditions that supported deep convection in rOn-500, we performed an additional 24 simulations, 12 with pristine and 12 with polluted conditions in which aerosol direct effects were turned off. By comparing these four model ensembles, we were able to analyze the aerosol direct and indirect effects on tropical sea breeze convection, as well as the role of the environment in modulating these effects.

We first compared rOn-500 and rOn-2000. The analysis demonstrated that the increased scattering of incoming solar radiation due to enhanced aerosol loading results in less shortwave radiation reaching the surface. Subsequently, the longwave emission from the land surface also decreases, producing a cooler land surface and a smaller land-sea thermal contrast. In turn, the surface sensible and latent heat fluxes, the surface-based mixed layer depth, and the sea breeze inland extent were all reduced. Therefore, the three ingredients of moist convection: moisture, instability, and lift (Doswell, 1987), were reduced in the presence of aerosol direct effects. Consequently, an overall suppression of over-land convection was observed, as evidenced by reduced cloud top height distribution, updraft velocities, and surface accumulated precipitation in the polluted rOn-2000 ensemble.

Both the initial boundary layer potential temperature and the soil saturation fraction were shown to have interesting implications for the convective development and the subsequent aerosol impacts on this development. Firstly, deep convection was only observed in those polluted ensemble simulations in which the initial boundary layer potential temperatures were greater than 299 K, compared with 297 K in rOn-500. With enhanced aerosol loading inducing cooler and more stable near-surface environments in rOn-2000 than rOn-500, the warmer initial boundary layer potential temperatures were necessary to facilitate deep convection through higher CAPE. Secondly, with the aerosol-induced reduction in surface fluxes, the relative importance of the soil saturation fraction on the land-surface sensible heat flux, boundary layer mixing, and boundary layer convective updrafts ahead of the sea breeze were decreased. A nonlinear sensitivity of boundary layer updraft velocities to soil saturation fraction was also found, in which the greatest convective updraft response was observed in the MID soil saturation fraction regime, followed by a moderate response in the DRY soil saturation fraction regime, and no response in the WET regime. The trends were similar in both the pristine and polluted ensembles, although the updraft velocities were consistently greater in pristine ensembles, again due to the warmer surfaces and greater sensible heat fluxes in these cases. Nonlinear responses of over-land tropical convective precipitation have also recently been observed by Drager et al. (2020).

The overall aerosol-induced reduction in the maximum cloud top height, the surface accumulated precipitation, and updraft velocity percentiles occurred despite the multitudinous environments produced from the 130 different initial conditions. Hence, these findings appear to be robust, occurring independent of the sea breeze environment. As such, they extend those of Grant and van den Heever (2014) in which a similar sensitivity of tropical sea breeze convection to aerosol loading was demonstrated for only one set of initial conditions. When aerosol-radiation interactions (i.e., aerosol direct effects) were turned off, aerosol-induced reduction in convective intensity was not apparent. Therefore, our results also underscore the potential underestimation of convective responses to enhanced aerosol loading without considering aerosol direct effects, as has been pointed out in previous studies which did not consider various environments (e.g., Yu et al., 2002; Jiang and Feingold, 2006; Grant and van den Heever, 2014). Given that many of the previous studies on aerosol-induced deep convective invigoration have excluded aerosol direct effects, our results suggest that future studies should consider both aerosol direct and indirect effects to fully understand aerosol impacts on daytime convection, in particular.

To assess the role of both aerosol direct and indirect effects, and as to how the environment modulates these effects, we compared the land-averaged updraft velocities and surface accumulated precipitation for two groups of smaller model ensembles: rOn-500 versus rOn-2000 in which aerosol-radiation interactions were allowed, and rOff-500 versus rOff-2000 in which aerosol-radiation interactions were turned off. While 5 out of 12 initial conditions did not produce deep convection in rOn-2000, deep convection developed in all 12 of the simulations in rOff-2000, thereby demonstrating that the presence of aerosol direct effects ultimately produces unfavorable conditions for deep convection in those environments that are initially suboptimal for convection.

In both comparisons of rOn-500 with rOn-2000 and rOff-500 with rOff-2000, updraft responses above the freezing level to enhanced aerosol loading differed depending on the initial conditions, suggesting that the environment modulates cold phase updraft responses to enhanced aerosol loading. Below the freezing level, rOff-500 and rOff-2000 showed consistent enhancement of the updraft velocities and condensational growth rates in response to enhanced aerosol loading, independent of the 130 different sea breeze environments, and as such, provide robust support of the existing theories of condensational or warm-phase invigoration (e.g., Kogan and Martin, 1994; Seiki and Nakajima, 2014; Sheffield et al., 2015) when aerosol-radiation interactions were excluded. However, in the presence of aerosol direct effects, updrafts in the warm phase regions of simulations with different initial conditions showed a variety of negative, neutral, and positive changes, implying that warm phase invigoration is environmentally modulated when aerosol direct effects are included. Finally, surface precipitation responses to enhanced aerosol loading varied without aerosol-radiation interactions, in contrast to the robust aerosol-induced suppression of precipitation found to occur when aerosol-radiation interactions were included. This discrepancy not only implies environmental modulation of the aerosol impacts on precipitation but also suggests the potential overestimation of precipitation responses when aerosol direct effects were excluded.

In summary, when aerosol direct effects are excluded, warm phase aerosol-induced invigoration of the updrafts is found to be robust and independent of environmental modulation, whereas cold invigoration is found to be environmentally modulated. The condensational invigoration results are therefore in keeping with previous results in which the direct effects have been excluded. However, the same cannot be said for the trends in cold-phase invigoration which are found to depend on environmental conditions. Also, surface precipitation responses to enhanced aerosol loading are found to be consistent and independent of environmental modulation when aerosol directs effects are included. However, as including the interactions between aerosols and radiation is the closest representation of reality, we are left to conclude that a robust reduction of surface precipitation in response to enhanced aerosol loading is therefore evident, which is in keeping with Tao et al. (2012) while aerosol-induced convective invigoration of tropical continental convection, be it warm-phase or cold-phase invigoration, is modulated by the environment.

Future studies should consider examining how the microphysical processes and associated dynamical feedback processes involving latent heating changes vary as a function of specific environments. In this study, we only tested a single aerosol species, ammonium sulfate, a strong scatterer, but a poor absorber of radiation. It is worth noting that absorbing aerosols such as mineral dust or smoke, are also substantial contributors to aerosol emissions in equatorial

Africa (Adams et al., 2012; Chakraborty et al., 2015). The potential importance of the interactions of absorbing aerosol with radiation and microphysics has been reported in previous modeling studies. For instance, Saide et al. (2015) analyzed the impacts of biomass burning smoke on environmental conditions that resulted in a higher likelihood of tornado occurrence. They found that smoke absorption tends to either burn off clouds or enhance the capping inversion, depending on the smoke's location. Such radiation absorption in the presence of other aerosol species may therefore produce different effects on sea breeze convection. The perturbed parameter ensemble approach used in this study could easily be extended to such studies considering absorbing aerosol species.

We conclude that the results of this study underscore the importance of considering both aerosol direct and indirect effects when examining the impacts of enhanced aerosol loading on tropical convection. Furthermore, the environmental modulation of the aerosol direct and indirect effects on dynamical, microphysical, and precipitation characteristics of the tropical over-land convection simulated here demonstrates the need to examine aerosol impacts on convection for the wide range of convective environments supporting the same type of convective system.

CHAPTER 4: CONCLUDING REMARKS

4.1 Summary of studies

Sea breeze circulations are one of the most ubiquitous flow regimes in coastal regions. During the daytime, sea breezes propagate inland, thereby driving convective initiation and facilitating aerosol redistribution and processing. Although the fundamental dynamics of sea breeze circulation have been well understood for some time, accurately forecasting sea breeze convection has remained challenging. This is due in part to the uncertainties in the role played by environmental conditions and the covariance and interaction of various meteorological and surface parameters. Given that nearly half of the world's human population resides along the coastlines, it is critical to provide reliable forecasts of sea breeze convection. The overarching goals of this dissertation have therefore been to advance our understanding of tropical sea breeze convection as a function of environmental and aerosol conditions, thereby contributing to enhanced forecasts of such systems. The goals were achieved by conducting four ensembles of cloud-resolving model simulations of tropical sea breeze convection, where five thermodynamic (boundary layer potential temperature, relative humidity, and height; inversion layer strength and depth), one wind (zonal wind speed), four surface (soil saturation fraction, land/ocean surface-atmosphere temperature difference, horizontal gradient of sea surface temperature), and two aerosol loading (pristine and polluted) characteristics, previously identified to be important in the literature, were simultaneously perturbed.

The primary objective of the first study (Chapter 2) was to identify predominant environmental parameters that exert the greatest control over changes in (1) the sea breeze inland characteristics; (2) the over-land updraft velocities developing ahead of and along the sea breeze front; and (3) the vertical redistribution of aerosol. These goals were addressed using idealized cloud-resolving model simulations combined with an advanced multivariate sensitivity analysis algorithm. Using the Regional Atmospheric Modeling System (RAMS) coupled to an interactive land-surface model, an ensemble of 130 tropical sea breeze simulations over coastal rainforest environments were conducted. Statistical emulation and variance-based sensitivity analysis techniques were then applied to identify the key parameters over the ten-dimensional parameter space being explored. This study extended a previous study conducted by Igel et al (2017) which explored the impacts of various parameters on sea breeze characteristics in arid environments devoid of moist convection. A number of conclusions were reached regarding the predominant factors governing the sea breeze circulation characteristics and convective intensity including the following:

1. The cross-coast wind speed was identified as the main contributor to the inland extent of the sea breeze front, and is thus similar to the findings of the arid environment study conducted by Igel et al. (2018). However, the relative importance of surface properties on the inland extent was found to be less significant in the moist environment, where land-surface heating can be suppressed via moist convective processes and vegetation-atmosphere interactions and feedbacks.
2. A shallow and deep convective mode were identified. For the shallow regime, where convective available potential energy was limited, the inversion layer strength was found to be the primary control of the convective intensity. Over the deep regime, the boundary layer temperature was found to exert a robust control over the convective available potential energy and hence the convective intensity.

3. The predominant factors impacting the vertical redistribution of aerosols was closely related to those impacting the convective intensity.

Identifying the predominant factors governing the characteristics of the sea breeze circulation, its convective intensity, and its ability to redistribute aerosols, provide useful insights into where future observational efforts should be concentrated in order to improve model initialization data, and hence the forecasting of convective precipitation and air quality within coastal regions.

Chapter 3 focused on the impacts of microphysically and radiatively active aerosol particles on the intensity of tropical sea breeze convection under a wide range of environments. First, a pristine and a polluted ensemble, each comprised of 130 simulations with different environmental conditions, were conducted. Second, to examine the impact of aerosol indirect effects on deep convective development, aerosol-radiation interactions were turned off for two additional, much smaller ensembles comprised only of those 12 simulations that produced deep convection in the large pristine ensemble. The key findings of Chapter 3 are as follows:

1. In polluted scenarios, due to the enhanced scattering of incoming radiation and the resulting reduction in surface fluxes, all three ingredients of moist convection: moisture, instability, and lift were reduced. Overall, the intensity of the sea breeze convection, represented by updraft velocities and accumulated precipitation, decreased due to aerosol direct effects.
2. Aerosol indirect effects were also looked into by deactivating aerosol-radiation interactions. Regardless of the initial conditions, and thus the local environment, condensational invigoration was found to occur irrespective of the environment, and hence is not environmentally modulated. On the other hand, cold phase invigoration was found to depend

on the initial conditions, implying the environmental modulation of aerosol effects on deep convection.

3. Surface precipitation responses to enhanced aerosol loading were found to increase, decrease or remain the same when aerosol-radiation interactions were excluded, in contrast to the robust aerosol-induced suppression of precipitation that was found to occur when aerosol-radiation interactions were included. This not only suggests environmental modulation of the aerosol impacts on precipitation when aerosol directs are not included, but also suggests the potential overestimation of precipitation responses when aerosol-radiation interactions were excluded.

Findings of Chapter 3 highlight the significance of considering aerosol direct and indirect effects on aerosol-cloud interaction studies and investigating aerosol impacts under a wide range of environments that support the same type of convective system. In particular, the results of Chapter 3 guide future aerosol-cloud interactions studies since the majority of previous studies have investigated aerosol impacts on convection without aerosol direct effects under only a narrow range of environments.

4.2 Future work

The results from the two studies presented in this dissertation have advanced our understanding of tropical sea breeze convection as a function of environmental and aerosol conditions through the use of a fully interactive aerosol-environment-convection framework. Furthermore, the perturbed parameter ensemble simulation approach combined with statistical emulation and variance-based sensitivity analyses have shown promising results in identifying key parameters on sea breeze convection over the multi-parameter space employed here. To that end, the results from the two studies presented in this dissertation provide a number of avenues for future research.

Firstly, one challenge in applying the Gaussian process emulation and variance-based sensitivity analysis was in attempting to study extreme value outliers, such as those that were produced in association with the sea breeze induced deep convection. While the majority of the simulations produced shallow and moderate convection, more than 90% of the ensemble members did not produce deep convection. The simulations which generated deep convection behaved very differently from the majority of simulations. As such, construction of a statistical emulator for the intensity of sea breeze-initiated convection (e.g., maximum cloud top height, maximum updraft velocity, precipitation rate) was infeasible. Recently, two deep convective studies using the same statistical approach have been published (Wellmann et al., 2018, 2020). They successfully employed Gaussian process emulation with initial atmospheric conditions that favored the development of deep convection (e.g., the potential temperature at the ground between 299–301 K), and one of the parameters tested was CCN concentration (100–4000 cm^{-3}). Future studies could apply the approaches of Wellman et al (2020), thereby building additional ensembles of tropical sea breeze deep convection. Chapter 2 and Chapter 3 provide which parameters, and thus which environments, guarantee the development of deep convection. Expanding the current range of initial boundary layer potential temperature uncertainties (285–300 K), adding tropical sea breeze simulations to the training set in which the initial boundary layer potential temperature higher than 297 K to ensure more number of deep convective simulations, while the rest of environmental parameters and aerosol loading conditions still are perturbed, would be worthwhile to trying.

Secondly, collisions of cold pools produced by the convection along the sea breeze with the sea breeze front itself have been observed in simulations used in this dissertation work but were not the focus of this analysis. The interactions between the cold pool gust fronts and the thermally driven breeze circulation have been examined to better understand the convective initiation processes (Carbone et al., 2000; Rieck et al., 2015; Rochetin et al., 2016). While different phases of interactions have been identified in previous studies, the sensitivity of convective characteristics resulting from the collision to a range of environments and aerosol conditions has remained unanswered. It would be interesting to analyze these simulations to examine these collisions. Of course, the perturbed parameter ensemble simulations may need to be rerun using higher spatial resolution more suitable for representing cold pool dynamics (Grant and van den Heever, 2016), however, the current set of four ensembles would be a useful place to start such an analysis. Furthermore, precipitation infiltration into the soil and subsequent two-way interactive land-atmosphere processes (e.g., land surface cooling through precipitation and resulting stabilization of the low-level) have not been included in the previous cold pool-sea breeze collision studies mentioned above, and hence could be examined here.

Thirdly, the responses of surface accumulated precipitation to enhanced aerosol loading to the perturbations of the soil saturation fraction need to be further examined. To that end, this study should be extended by considering different vegetation, soil types and aerosol species (e.g., mineral dust). Such extensions would allow for further examination of the synergy between soil saturation fraction and aerosol loading under a wide range of land representations, from the bare desert with sandy soil where dust lofting can occur through to urban areas with buildings, a large fraction of cement surfaces, and anthropogenic aerosol.

Fourthly, this study could be extended from the current focus on tropical equatorial Africa to include additional geographic regions. Having initial conditions representative of different geographical coastal regions of interest would be feasible and interesting, and would help to enhance NWP forecasts of sea breeze convection around the world.

Lastly, this study has been conducted using only one numerical modeling platform. Extending the study to other numerical models could illuminate more generic issues pertaining to cloud-resolving models. Also, including the forecast error ranges of specific forecasting models into the parameter uncertainty ranges (Wellman et al., 2020) could be very useful in this endeavor.

Nonetheless, the findings learned from this suite of extensive perturbed parameter ensemble simulations of tropical sea breeze circulations and their association convection as a function of environment and aerosol condition, have provided a number of insights into sea breeze convective processes, the role of predominant environmental factors, and the impacts of aerosols, and as such, how to improve sea breeze forecasting, and which parameters warrant further investigation.

REFERENCES

Albrecht, B. A. (1989). Aerosols, cloud microphysics, and fractional cloudiness. Science, **245**(4923), 1227–1230. https://doi.org/ 10.1126/science.245.4923.1227

Andreae, M. O., Chapuis, A., Cros, B., Fontan, J., Helas, G., Justice, C., ... & Nganga, D. (1992). Ozone and Aitken nuclei over equatorial Africa: Airborne observations during DECAFE 88. *Journal of Geophysical Research: Atmospheres*, **97**(D6), 6137–6148. https://doi.org/10.1029/91JD00961

Andreae, M. O., Rosenfeld, D., Artaxo, P., Costa, A. A., Frank, G. P., Longo, K. M., & Silva-Dias, M. D. (2004). Smoking rain clouds over the Amazon. *Science*, **303**(5662), 1337–1342. https://doi.org/10.1126/science.1092779

Antonelli, M., & Rotunno, R. (2007). Large-eddy simulation of the onset of the sea breeze. *Journal of the Atmospheric Sciences*, **64**(12), 4445–4457. https://doi.org/10.1175/2007JAS2261.1

Arritt, R. W. (1993). Effects of the large-scale flow on characteristics features of the sea breeze. Journal of Applied Meteorology, **32**(1), 116–125. https://doi.org/10.1175/1520-0450(1993)032<0116:EOTLSF>2.0.CO;2

Atkins, N. T., Wakimoto, R. M., & Weckwerth, T. M. (1995). Observations of the sea breeze front during CaPE. Part II: Dual-Doppler and Aircraft Analysis. Monthly Weather Review, **123**, 944–969. https://doi.org/10.1175/1520-0493(1995)123<0944:OOTSBF>2.0.CO;2

Atwood, S. A., Reid, J. S., Kreidenweis, S. M., Blake, D. R., Jonsson, H. H., Lagrosas, N. D., ... & Simpas, J. B. (2017). Size-resolved aerosol and cloud condensation nuclei (CCN) properties in the remote marine South China Sea–Part 1: Observations and source classification. *Atmospheric Chemistry and Physics*, **17**(2), 1105–1123.

Azorin-Molina, C., & Chen, D. (2009). A climatological study of the influence of synoptic-scale flows on sea breeze evolution in the Bay of Alicante (Spain). *Theoretical and Applied Climatology*, **96**(3–4), 249–260. https://doi.org/10.1007/s00704-008-0028-2

Baker, R. D., Lynn, B. H., Boone, A., Tao, W. K., & Simpson, J. (2001). The influence of soil moisture, coastline curvature, and land-breeze circulations on sea-breeze-initiated precipitation. *Journal of Hydrometeorology*, **2**(2), 193–211. https://doi.org/10.1175/1525-7541(2001)002<0193:TIOSMC>2.0.CO;2

Banta, R. M., Olivier, L. D., & Levinson, D. H. (1993). Evolution of the Monterey Bay sea-breeze layer as observed by pulsed Doppler lidar. *Journal of the Atmospheric Sciences*, **50**(24), 3959–3982. https://doi.org/10.1175/1520-0469(1993)050<3959:EOTMBS>2.0.CO;2

Banta, R. M., Senff, C. J., Alvarez, R. J., Langford, A. O., Parrish, D. D., Trainer, M. K., Darby, L. S., Michael Hardesty, R., Lambeth, B., & Andrew Neuman, J. (2011). Dependence of daily peak O3 concentrations near Houston, Texas on environmental factors: Wind speed, temperature, and boundary-layer depth. *Atmospheric Environment*, **45**(1), 162–173. https://doi.org/10.1016/j.atmosenv.2010.09.030

Blumenthal, D. L., White, W. H., & Smith, T. B. (1978). Anatomy of a Los Angeles smog episode: Pollutant transport in the daytime sea breeze regime. *Atmospheric Environment*, **12**(4), 893–907. https://doi.org/10.1016/0004-6981(78)90028-8

Boybeyi, Z., & Raman, S. (1992). A three-dimensional numerical sensitivity study of convection over the Florida peninsula. *Boundary-Layer Meteorology*, **60**(4), 325–359. https://doi.org/10.1007/BF00155201

Caicedo, V., Rappenglueck, B., Cuchiara, G., Flynn, J., Ferrare, R., Scarino, A. J., Berkoff, T., Senff, C., Langford, A., & Lefer, B. (2019). Bay breeze and sea breeze circulation impacts on the planetary boundary layer and air quality from an observed and modeled DISCOVER-AQ Texas case study. *Journal of Geophysical Research: Atmospheres*, **124**, 7359–7378. https://doi.org/10.1029/2019JD030523

Chakraborty, S., Fu, R., Wright, J. S., & Massie, S. T. (2015). Relationships between convective structure and transport of aerosols to the upper troposphere deduced from satellite observations. *Journal of Geophysical Research: Atmospheres*, **120**(13), 6515–6536. https://doi.org/10.1002/2015JD023528

Chen, G., Iwai, H., Ishii, S., Saito, K., Seko, H., Sha, W., & Iwasaki, T. (2019). Structures of the sea-breeze front in dual-Doppler lidar observation and coupled mesoscale-to-LES modeling. *Journal of Geophysical Research: Atmospheres*, **124**(5), 2397–2413. https://doi.org/10.1029/2018JD029017

Chen, Q., Koren, I., Altaratz, O., Heiblum, R. H., Dagan, G., & Pinto, L. (2017). How do changes in warm-phase microphysics affect deep convective clouds? *Atmospheric Chemistry and Physics*, **17**(15). 9585–9598. https://doi.org/10.5194/acp-17-9585-2017

Chou, C., Neelin, J. D., Chen, C. A., & Tu, J. Y. (2009). Evaluating the "rich-get-richer" mechanism in tropical precipitation change under global warming. *Journal of Climate*, **22**(8), 1982–2005.

Clarke, R. H. (1983). Fair weather nocturnal inland wind surges and atmospheric bores: Part I nocturnal wind surges. *Australian Meteorological Magazine*, **31**, 133–145.

Cotton, W. R., Alexander, G. D., Hertenstein, R., Walko, R. L., McAnelly, R. L., & Nicholls, M. (1995). Cloud venting—A review and some new global annual estimates. *Earth-Science Reviews*, **39**(3–4), 169–206. https://doi.org/10.1016/0012-8252(95)00007-0

Cotton, W. R., Pielke, R. A., Walko, R. L., Liston, G. E., Tremback, C. J., Jiang, H., McAnelly, R. L., Harrington, J. Y., Nicholls, M. E., Carrio, G. G., & McFadden, J. P. (2003). RAMS

2001: Current status and future directions. *Meteorology and Atmospheric Physics*, **82**(1–4), 5–29. https://doi.org/10.1007/s00703-001-0584-9

Crook, N. A., & Sun, J. (2004). Analysis and forecasting of the low-level wind during the Sydney 2000 Forecast Demonstration Project. *Weather and Forecasting*, **19**(1), 151–167. https://doi.org/10.1175/1520-0434(2004)019<0151:AAFOTL>2.0.CO;2

Crosman, E. T., & Horel, J. D. (2010). Sea and lake breezes: A review of numerical studies. *Boundary-Layer Meteorology*, **137**(1), 1–29. https://doi.org/10.1007/s10546-010-9517-9

Darby, L. S., Banta, R. M., & Pielke, R. A. Sr. (2002). Comparisons between mesoscale model terrain sensitivity studies and Doppler lidar measurements of the sea breeze at Monterey Bay. *Monthly Weather Review*, **130**(12), 2813–2838. https://doi.org/10.1175/1520-0493(2002)130<2813:CBMMTS>2.0.CO;2

DeMott, P. J., Prenni, A. J., Liu, X., Kreidenweis, S. M., Petters, M. D., Twohy, C. H., ... & Rogers, D. (2010). Predicting global atmospheric ice nuclei distributions and their impacts on climate. *Proceedings of the National Academy of Sciences*, **107**(25), 11217–11222. https://doi.org/10.1073/pnas.0910818107

Ding, A., Wang, T., Zhao, M., Wang, T., & Li, Z. (2004). Simulation of sea-land breezes and a discussion of their implications on the transport of air pollution during a multi-day ozone episode in the Pearl River Delta of China. *Atmospheric Environment*, **38**(39), 6737–6750. https://doi.org/10.1016/j.atmosenv.2004.09.017

Doswell III, C. A. (1987). The distinction between large-scale and mesoscale contribution to severe convection: A case study example. *Weather and Forecasting*, **2**(1), 3–16. https://doi.org/10.1175/1520-0434(1987)002<0003:TDBLSA>2.0.CO;2

Drager, A. J., Grant, L. D., & van den Heever, S. C. Cold Pool Responses to Changes in Soil Moisture. *Journal of Advances in Modeling Earth Systems*, **12,** e2019MS001922. https://doi.org/10.1029/2019MS001922

Drobinski, P., Rotunno, R., & Dubos, T. (2011). Linear theory of the sea breeze in a thermal wind. *Quarterly Journal of the Royal Meteorological Society*, **137**(659), 1602–1609. https://doi.org/10.1002/qj.847

Edinger, J. G., & Helvey, R. A. (1961). The San Fernando convergence zone. *Bulletin of the American Meteorological Society*, **42**(9), 626–637. https://doi.org/10.1175/1520-0477-42.9.626

Emanuel, K. A. (1994). *Atmospheric Convection*. New York: Oxford University Press.

Estoque, M. A. (1962). The sea breeze as a function of the prevailing synoptic situation. *Journal of the Atmospheric Sciences*, **19**(3), 244–250. https://doi.org/10.1175/1520-0469(1962)019<0244:TSBAAF>2.0.CO;2

Fan, J., Rosenfeld, D., Ding, Y., Leung, L. R., & Li, Z. (2012). Potential aerosol indirect effects on atmospheric circulation and radiative forcing through deep convection. *Geophysical Research Letters*, **39**(9). https://doi.org/10.1029/2012GL051851

Fan, J., Rosenfeld, D., Zhang, Y., Giangrande, S. E., Li, Z., Machado, L. A., ... & Barbosa, H. M. (2018). Substantial convection and precipitation enhancements by ultrafine aerosol particles. *Science*, **359**(6374), 411–418. https://doi.org/10.1126/science.aan8461

Fan, J., Yuan, T., Comstock, J. M., Ghan, S., Khain, A., Leung, L. R., ... & Ovchinnikov, M. (2009). Dominant role by vertical wind shear in regulating aerosol effects on deep convective clouds. *Journal of Geophysical Research: Atmospheres*, **114**(D22). https://doi.org/10.1029/2009JD012352

Fan, J., Zhang, R., Li, G., & Tao, W. K. (2007). Effects of aerosols and relative humidity on cumulus clouds. *Journal of Geophysical Research: Atmospheres*, **112**(D14). https://doi.org/10.1029/2006JD008136

Fankhauser, J. C., Crook, N. A., Tuttle, J., Miller, L. J., & Wade, C. G. (1995). Initiation of deep convection along boundary layer convergence lines in a semitropical environment. *Monthly Weather Review*, **123**(2), 291–314. https://doi.org/10.1175/1520-0493(1995)123<0291:IODCAB>2.0.CO;2

Feingold, G., Jiang, H., & Harrington, J. Y. (2005). On smoke suppression of clouds in Amazonia. *Geophysical Research Letters*, **32**(2). https://doi.org/10.1029/2004GL021369

Feingold, G., McComiskey, A., Yamaguchi, T., Johnson, J. S., Carslaw, K. S., & Schmidt, K. S. (2016). New approaches to quantifying aerosol influence on the cloud radiative effect. *Proceedings of the National Academy of Sciences*, **113**(21), 5812–5819. https://doi.org/10.1073/pnas.1514035112

Feingold, G., Tzivion, S., & Leviv, Z. (1988). Evolution of raindrop spectra. Part I: Solution to the stochastic collection/breakup equation using the method of moments. *Journal of the atmospheric sciences*, **45**(22), 3387–3399. https://doi.org/10.1175/1520-0469(1988)045<3387:EORSPI>2.0.CO;2

Feingold, G., Walko, R. L., Stevens, B., & Cotton, W. R. (1998). Simulations of marine stratocumulus using a new microphysical parameterization scheme. *Atmospheric research*, **47**, 505–528. https://doi.org/10.1016/S0169-8095(98)00058-1

Finkele, K. (1998). Inland and offshore propagation speeds of a sea breeze from simulations and measurements. *Boundary-Layer Meteorology*, **87**(2), 307–329. https://doi.org/10.1023/A:1001083913327

Fovell, R. (2005). Convective initiation ahead of the sea-breeze front. *Monthly Weather Review*, **133**(1), 264–278. https://doi.org/10.1175/MWR-2852.1

Freitas, E. D., Rozoff, C. M., Cotton, W. R., & Silva Dias, P. L. (2006). Interactions of an urban heat island and sea-breeze circulations during winter over the metropolitan area of São

Paulo, Brazil. *Boundary-Layer Meteorology*, **122**(1), 43–65. https://doi.org/10.1007/s10546-006-9091-3

Glassmeier, F., Hoffmann, F., Johnson, J. S., Yamaguchi, T., Carslaw, K. S., & Feingold, G. (2019). An emulator approach to stratocumulus susceptibility. *Atmospheric Chemistry and Physics*, **19**(15), 10191–10203. https://doi.org/10.5194/acp-19-10191-2019

Grant, L. D., & van den Heever, S. C. (2014). Aerosol-cloud-land surface interactions within tropical sea breeze convection. *Journal of Geophysical Research: Atmospheres*, **119**, 8340–8361. https://doi.org/10.1002/2014JD021912

Grant, L. D., & van den Heever, S. C. (2015). Cold pool and precipitation responses to aerosol loading: Modulation by dry layers. *Journal of the Atmospheric Sciences*, **72**(4), 1398–1408. https://doi.org/10.1175/JAS-D-14-0260.1

Harrington, J. Y. (1997). The effects of radiative and microphysical processes on simulated warm and transition season Arctic stratus (Doctoral dissertation). Fort Collins, CO: Colorado State University.

Hill, G. E. (1974). Factors controlling the size and spacing of cumulus clouds as revealed by numerical experiments. *Journal of the Atmospheric Sciences*, **31**(3), 646–673. https://doi.org/10.1175/1520-0469(1974)031<0646:FCTSAS>2.0.CO;2

Holtslag, A. A. M., Svensson, G., Baas, P., Basu, S., Beare, B., Beljaars, A. C. M., Bosveld, F. C., Cuxart, J., Lindvall, J., Steeneveld, G. J., Tjernstrom, M., & van de Wiel, B. J. H. (2013). Stable atmospheric boundary layers and diurnal cycles: Challenges for weather and climate models. *Bulletin of the American Meteorological Society*, **94**(11), 1691–1706. https://doi.org/10.1175/BAMS-D-11-00187.1

Hong, J. S. (2003). Evaluation of the high-resolution model forecasts over the Taiwan area during GIMEX. *Weather and Forecasting*, **18**(5), 836–846. https://doi.org/10.1175/1520-0434(2003)018<0836:EOTHMF>2.0.CO;2

Hu, X. M., & Xue, M. (2016). Influence of synoptic sea-breeze fronts on the urban heat island intensity in Dallas–Fort Worth, Texas. *Monthly Weather Review*, **144**(4), 1487–1507. https://doi.org/10.1175/MWR-D-15-0201.1

Igel, A. L., van den Heever, S. C., & Johnson, J. S. (2018). Meteorological and land surface properties impacting sea breeze extent and aerosol distribution in a dry environment. *Journal of Geophysical Research: Atmospheres*, **123**, 22–37. https://doi.org/10.1002/2017JD027339

Iwai, H., Murayama, Y., Ishii, S., Mizutani, K., Ohno, Y., & Hashiguchi, T. (2011). Strong updraft at a sea-breeze front and associated vertical transport of near-surface dense aerosol observed by doppler lidar and ceilometer. *Boundary-Layer Meteorology*, **141**(1), 117–142. https://doi.org/10.1007/s10546-011-9635-z

Jiang, H., & Feingold, G. (2006). Effect of aerosol on warm convective clouds: Aerosol-cloud-surface flux feedbacks in a new coupled large eddy model. *Journal of Geophysical Research: Atmospheres*, **111**(D1). https://doi.org/10.1029/2005JD006138

Johnson, J. S., Cui, Z., Lee, L. A., Gosling, J. P., Blyth, A. M., & Carslaw, K. S. (2015). Evaluating uncertainty in convective cloud microphysics using statistical emulation. *Journal of Advances in Modeling Earth Systems*, **7**, 162–187. https://doi.org/10.1002/2014MS000383

Kacarab, M., Thornhill, K. L., Dobracki, A., Howell, S. G., O'Brien, J. R., Freitag, S., ... & Nenes, A. (2020). Biomass burning aerosol as a modulator of the droplet number in the southeast Atlantic region. *Atmospheric Chemistry and Physics*, **20**(5). https://doi.org/10.5194/acp-20-3029-2020

Kala, J., Lyons, T. J., Abbs, D. J., & Nair, U. S. (2010). Numerical simulations of the impacts of land-cover change on a southern sea breeze in south-west Western Australia. *Boundary-Layer Meteorology*, **135**(3), 485–503. https://doi.org/10.1007/s10546-010-9486-z

Kendon, E. J., Roberts, N. M., Fowler, H. J., Roberts, M. J., Chan, S. C., & Senior, C. A. (2014). Heavier summer downpours with climate change revealed by weather forecast resolution model. *Nature Climate Change*, **4**(7), 570–576. https://doi.org/10.1038/nclimate2258

Khain, A. P., BenMoshe, N., & Pokrovsky, A. (2008). Factors determining the impact of aerosols on surface precipitation from clouds: An attempt at classification. *Journal of the Atmospheric Sciences*, **65**(6), 1721–1748. https://doi.org/10.1175/2007JAS2515.1

Khain, A., Pokrovsky, A., Pinsky, M., Seifert, A., & Phillips, V. (2004). Simulation of effects of atmospheric aerosols on deep turbulent convective clouds using a spectral microphysics mixed-phase cumulus cloud model. Part I: Model description and possible applications. *Journal of the Atmospheric Sciences*, **61**(24), 2963–2982. https://doi.org/10.1175/JAS-3350.1

Khain, A., Rosenfeld, D., & Pokrovsky, A. (2005). Aerosol impact on the dynamics and microphysics of deep convective clouds. *Quarterly Journal of the Royal Meteorological Society*, **131**(611), 2639–2663. https://doi.org/10.1256/qj.04.62

Kingsmill, D. E. (1995). Convection initiation associated with a sea-breeze front, a gust front, and their collision. *Monthly Weather Review*, **123**(10), 2913–2933. https://doi.org/10.1175/1520-0493(1995)123<2913:CIAWAS>2.0.CO;2

Klemp, J. B., & Wilhelmson, R. B. (1978). The simulation of three-dimensional convective storm dynamics. *Journal of the Atmospheric Sciences*, **35**(6), 1070–1096. https://doi.org/10.1175/1520-0469(1978)035<1070:TSOTDC>2.0.CO;2

Kogan, Y. L., & Martin, W. J. (1994). Parameterization of bulk condensation in numerical cloud models. *Journal of the Atmospheric Sciences*, **51**(12), 1728–1739. https://doi.org/10.1175/1520-0469(1994)051<1728:POBCIN>2.0.CO;2

Koren, I., Dagan, G., & Altaratz, O. (2014). From aerosol-limited to invigoration of warm convective clouds. *Science*, **344**(6188), 1143–1146. https://doi.org/10.1126/science.1252595

Koren, I., Kaufman, Y. J., Remer, L. A., & Martins, J. V. (2004). Measurement of the effect of Amazon smoke on inhibition of cloud formation. *Science*, **303**(5662), 1342–1345. https://doi.org/10.1126/science.1089424

Koren, I., Martins, J. V., Remer, L. A., & Afargan, H. (2008). Smoke invigoration versus inhibition of clouds over the Amazon. *Science*, **321**(5891), 946–949. https://doi.org/10.1126/science.1159185

Laing, A. G., Carbone, R. E., & Levizzani, V. (2011). Cycles and propagation of deep convection over equatorial Africa. *Monthly Weather Review*, **139**(9), 2832–2853. https://doi.org/10.1175/2011MWR3500.1

Lebo, Z. (2018). A numerical investigation of the potential effects of aerosol-induced warming and updraft width and slope on updraft intensity in deep convective clouds. *Journal of the Atmospheric Sciences*, **75**(2), 535–554. https://doi.org/10.1175/JAS-D-16-0368.1

Lebo, Z. J., & Morrison, H. (2014). Dynamical effects of aerosol perturbations on simulated idealized squall lines. *Monthly Weather Review*, **142**(3), 991–1009. https://doi.org/10.1175/MWR-D-13-00156.1

Lee, L. A., Carslaw, K. S., Pringle, K. J., Mann, G. W., & Spracklen, D. V. (2011). Emulation of a complex global aerosol model to quantify sensitivity to uncertain parameters. *Atmospheric Chemistry and Physics*, **11**(23), 12253–12273. https://doi.org/10.5194.acp-11-12253-2011

Lee, L. A., Pringle, K. J., Reddington, C. L., Mann, G. W., Stier, P., Spracklen, D. V., Pierce, J. R., & Carslaw, K. S. (2013). The magnitude and causes of uncertainty in global model simulations of cloud condensation nuclei. *Atmospheric Chemistry and Physics*, **13**(17), 8879–8914. https://doi.org/10.5194/acp-13-8879-2013

Lee, S. S., Donner, L. J., Phillips, V. T., & Ming, Y. (2008). Examination of aerosol effects on precipitation in deep convective clouds during the 1997 ARM summer experiment. *Quarterly Journal of the Royal Meteorological Society*, **134**(634), 1201–1220. https://doi.org/10.1002/qj.287

Lee, T. J. (1992). The impact of vegetation on the atmospheric boundary layer and convective storms (Doctoral dissertation). Fort Collins, CO: Colorado State University.

Lilly, D. K. (1962). On the numerical simulation of buoyant convection. *Tellus*, **14**(2), 148–172. https://doi.org/10.1111/j.2153-3490.1962.tb00128.x

Liu, H., Chan, J. C., & Cheng, A. Y. (2001). Internal boundary layer structure under sea-breeze conditions in Hong Kong. *Atmospheric Environment*, **35**(4), 683–692. https://doi.org/10.1016/S1352-2310(00)00335-6

Lombardo, K., Sinsky, E., Edson, J., Whitney, M. M., & Jia, Y. (2018). Sensitivity of offshore surface fluxes and sea breezes to the spatial distribution of sea-surface temperature. *Boundary-Layer Meteorology*, **166**(3), 475–502. https://doi.org/10.1007/s10546-017-0313-7

Loughner, C. P., Allen, D. J., Pickering, K. E., Zhang, D. L., Shou, Y. X., & Dickerson, R. R. (2011). Impact of fair-weather cumulus clouds and the Chesapeake Bay breeze on pollutant transport and transformation. *Atmospheric Environment*, 45(24), 4060–4072. https://doi.org/10.1016/j.atmosenv.2011.04.003

Loughner, C. P., Tzortziou, M., Follette-Cook, M., Pickering, K. E., Goldberg, D., Satam, C., Weinheimer, A., Crawford, J. H., Knapp, D. J., Montzka, D. D., Diskin, G. S., & Dickerson, R. R. (2014). Impact of bay-breeze circulations on surface air quality and boundary layer export. *Journal of Applied Meteorology and Climatology*, **53**(7), 1697–1713. https://doi.org/10.1175/JAMC-D-13-0323.1

Lu, R., & Turco, R. P. (1994). Air pollutant transport in a coastal environment. Part I: Two-dimensional simulations of sea-breeze and mountain effects. *Journal of the Atmospheric Sciences*, **51**(15), 2285–2308. https://doi.org/10.1175/1520-0469(1994)051<2285:APTIAC>2.0.CO;2

Lynn, B. H., Tao, W. K., & Abramopoulos, F. (2001). A parameterization for the triggering of landscape-generated moist convection. Part I: Analysis of high-resolution model results. *Journal of the atmospheric sciences*, **58**(6), 575–592. https://doi.org/10.1175/1520-0469(2001)058<0575:APFTTO>2.0.CO;2

Lyons, W. A., Pielke, R. A., Tremback, C. J., Walko, R. L., Moon, D. A., & Keen, C. S. (1995). Modeling impacts of mesoscale vertical motions upon coastal zone air pollution dispersion. *Atmospheric Environment*, **29**(2), 283–301. https://doi.org/10.1016/1352-2310(94)00217-9

Marinescu, P. J. (2020). Observations of aerosol particles and deep convective updrafts and the modeling of their interactions (Doctoral dissertation). Fort Collins, CO: Colorado State University.

Marinescu, P. J., van den Heever, S. C., Saleeby, S. M., Kreidenweis, S. M., & DeMott, P. J. (2017). The microphysical roles of lower-tropospheric versus midtropospheric aerosol particles in mature-stage MCS precipitation. *Journal of the Atmospheric Sciences*, **74**(11), 3657–3678. https://doi.org/10.1175/JAS-D-16-0361.1

Melas, D., & Kambezidis, H. D. (1992). The depth of the internal boundary layer over an urban area under sea-breeze conditions. *Boundary-Layer Meteorology*, **61**(3), 247–264. https://doi.org/10.1007/BF02042934

Meyers, M. P., Walko, R. L., Harrington, J. Y., & Cotton, W. R. (1997). New RAMS cloud microphysics parameterization. Part II: The two-moment scheme. *Atmospheric Research*, **45**(1), 3–39. https://doi.org/10.1016/S0169-8095(97)00018-5

Miao, J. F., Kroon, L. J. M., de Arellano, J. V. G., & Holtslag, A. A. M. (2003). Impacts of topography and land degradation on the sea breeze over eastern Spain. *Meteorology and Atmospheric Physics*, **84**(3–4), 157–170. https://doi.org/10.1007/s00703-002-0579-1

Miller, S. T. K., Keim, B. D., Talbot, R. W., & Mao, H. (2003). Sea breeze: Structure, forecasting, and impacts. *Reviews of Geophysics*, **41**(3), 1011. https://doi.org/10.1029/2003RG000124

Miller, S. T., & Keim, B. D. (2003). Synoptic-scale controls on the sea breeze of the central New England coast. *Weather and Forecasting*, **18**(2), 236–248. https://doi.org/10.1175/1520-0434(2003)018<0236:SCOTSB>2.0.CO;2

Miltenberger, A. K., Field, P. R., Hill, A. A., Rosenberg, P., Shipway, B. J., Wilkinson, J. M., ... & Blyth, A. M. (2018). Aerosol-cloud interactions in mixed-phase convective clouds-Part 1: Aerosol perturbations. *Atmospheric Chemistry and Physics*, **18**(5), 3119–3145. https://doi.org/10.5194/acp-18-3119-2018

Miltenberger, A. K., Field, P. R., Hill, A. A., Shipway, B. J., & Wilkinson, J. M. (2018). Aerosol-cloud interactions in mixed-phase convective clouds-Part 2: Meteorological ensemble. *Atmospheric Chemistry and Physics*, **18**(14), 10593–10613. https://doi.org/10.5194/acp-18-10593-2018

Moncrieff, M. W., & Liu, C. (1999). Convection initiation by density currents: Role of convergence, shear, and dynamical organization. *Monthly Weather Review*, **127**(10), 2455–2464. https://doi.org/10.1175/1520-0493(1999)127<2455:CIBDCR>2.0.CO;2

Morris, M. D., & Mitchell, T. J. (1995). Exploratory designs for computational experiments. *Journal of Statistical Planning and Inference*, **43**(3), 381–402. https://doi.org/10.1016/0378-3758(94)00035-T

Muppa, S. K., Anandan, V. K., Kesarkar, K. A., Rao, S. V. B., & Reddy, P. N. (2012). Study on deep inland penetration of sea breeze over complex terrain in the tropics. *Atmospheric Research*, **104**, 209–216. https://doi.org/10.1016/j.atmosres.2011.10.007

Natoli, M. B., & Maloney, E. D. (2019). Intraseasonal variability of the diurnal cycle of precipitation in the Philippines. *Journal of the Atmospheric Sciences*, **76**(11), 3633–3654. https://doi.org/10.1175/JAS-D-19-0152.1

Nesbitt, S. W., & Zipser, E. J. (2003). The diurnal cycle of rainfall and convective intensity according to three years of TRMM measurements. *Journal of Climate*, **16**(10), 1456–1475. https://doi.org/10.1175/1520-0442(2003)016<1456:TDCORA>2.0.CO;2

Niyogi, D., Chang, H. I., Chen, F., Gu, L., Kumar, A., Menon, S., & Pielke, R. A. (2007). Potential impacts of aerosol–land–atmosphere interactions on the Indian monsoonal rainfall characteristics. *Natural Hazards*, **42**(2), 345–359. https://doi.org/10.1007/s11069-006-9085-y

NOAA (National Oceanic and Atmospheric Administration). (2013). National coastal population report: Population trends from 1970 to 2020.

O'Hagan, A. (2006). Bayesian analysis of computer code outputs: A tutorial. *Reliability Engineering & System Safety*, **91**(10–11), 1290–1300. https://doi.org/10.1016/j.ress.2005.11.025

O'Gorman, P. A. (2012). Sensitivity of tropical precipitation extremes to climate change. *Nature Geoscience*, **5**(10), 697–700. https://doi.org/10.1038/ngeo1568

Ogawa, S., Sha, W., Iwasaki, T., & Wang, Z. (2003). A numerical study on the interaction of a sea-breeze front with convective cells in the daytime boundary layer. *Journal of the Meteorological Society of Japan*, **81**(4), 635–651. https://doi.org/10.2151/jmsj.81.635

Park, J. M., van den Heever, S. C., Igel, A. L., Grant, L. D., Johnson, J. S., Saleeby, S. M., ... & Reid, J. S. (2020). Environmental controls on tropical sea breeze convection and resulting aerosol redistribution. *Journal of Geophysical Research: Atmospheres*, **125**(6), e2019JD031699. https://doi.org/10.1029/2019JD031699

Physick, W. L., & Smith, R. K. (1985). Observations and dynamics of sea-breezes in northern Australia. *Australian Meteorological Magazine*, **33**(2), 51–63.

Pinsky, M., Mazin, I. P., Korolev, A., & Khain, A. (2013). Supersaturation and diffusional droplet growth in liquid clouds. *Journal of the Atmospheric Sciences*, **70**(9), 2778–2793. https://doi.org/10.1175/JAS-D-12-077.1

Porson, A., Steyn, D. G., & Schayes, G. (2007). Formulation of an index for sea breezes in opposing winds. *Journal of Applied Meteorology and Climatology*, **46**(8), 1257–1263. https://doi.org/10.1175/JAM2525.1

Posselt, D. J., He, F., Bukowski, J., & Reid, J. S. (2019). On the relative sensitivity of a tropical deep convective storm to changes in environment and cloud microphysical parameters. *Journal of the Atmospheric Sciences*, **76**(4), 1163–1185. https://doi.org/10.1175/JAS-D-18-0181.1

Pujol, G., Iooss, B., & Janon, A. (2013). Sensitivity: Sensitivity analysis, R package version 1.7.

R Core Team (2017). *R: A language and environment for statistical computing*. Vienna, Austria: R Foundation for Statistical Computing.

Rajeswari, J. R., Srinivas, C. V., Rao, T. N., & Venkatraman, B. (2020). Impact of land surface physics on the simulation of boundary layer characteristics at a tropical coastal station. *Atmospheric Research*, **238**, 104888.

Rasmussen, C. E., and C. K. I. Williams (2006), *Gaussian Processes for Machine Learning*, MIT Press, London, U. K.

Reible, D. D., Simpson, J. E., & Linden, P. F. (1993). The sea breeze and gravity-current frontogenesis. *Quarterly Journal of the Royal Meteorological Society*, **119**(509), 1–16. https://doi.org/10.1002/qj.49711950902

Reid, J. S., Xian, P., Hyer, E. J., Flatau, M. K., Ramirez, E. M., Turk, F. J., ... & Maloney, E. D. (2012). Multi-scale meteorological conceptual analysis of observed active fire hotspot activity and smoke optical depth in the Maritime Continent. *Atmospheric Chemistry and Physics*, **12**(4), 2117–2147. https://doi.org/10.5194/acp-12-2117-2012

Reynolds, R. W., Smith, T. M., Liu, C., Chelton, D. B., Casey, K. S., & Schlax, M. G. (2007). Daily high-resolution-blended analyses for sea surface temperature. *Journal of Climate*, **20**(22), 5473–5496. https://doi.org/10.1175/2007JCLI1824.1

Rieck, M., Hohenegger, C., & Gentine, P. (2015). The effect of moist convection on thermally induced mesoscale circulations. *Quarterly Journal of the Royal Meteorological Society*, **141**(691), 2418–2428. https://doi.org/10.1002/qj.2532

Riley Dellaripa, E. M., Maloney, E. D., Toms, B. A., Saleeby, S. M., & van den Heever, S. C. (2020). Topographic effects on the Luzon diurnal cycle during the BSISO. *Journal of the Atmospheric Sciences*, **77**(1), 3–30. https://doi.org/10.1175/JAS-D-19-0046.1

Rochetin, N., Couvreux, F., & Guichard, F. (2017). Morphology of breeze circulations induced by surface flux heterogeneities and their impact on convection initiation. *Quarterly Journal of the Royal Meteorological Society*, **143**(702), 463–478. https://doi.org/10.1002/qj.2935

Rosenfeld, D., Lohmann, U., Raga, G. B., O'Dowd, C. D., Kulmala, M., Fuzzi, S., ... & Andreae, M. O. (2008). Flood or drought: How do aerosols affect precipitation?. *Science*, **321**(5894), 1309–1313. https://doi.org/ 10.1126/science.1160606

Rotunno, R. (1983). On the linear theory of the land and sea breeze. *Journal of the Atmospheric Sciences*, **40**(8), 1999–2009. https://doi.org/10.1175/1520-0469(1983)040<1999:OTLTOT>2.0.CO;2

Rousseau-Rizzi, R., Kirshbaum, D. J., & Yau, M. K. (2017). Initiation of deep convection over an idealized mesoscale convergence line. *Journal of Atmospheric Science*, **74**(3), 835–853. https://doi.org/10.1175/JAS-D-16-0221.1

Roustant, O., Ginsbourger, D., & Deville, Y. (2012). DiceKriging, DiceOptim: Two R packages for the analysis of computer experiments by kriging-based metamodeling and optimization. *Journal of Statistical Software*, **51**(1), 1–55.

Saide, P. E., Thompson, G., Eidhammer, T., Da Silva, A. M., Pierce, R. B., & Carmichael, G. R. (2016). Assessment of biomass burning smoke influence on environmental conditions for multiyear tornado outbreaks by combining aerosol-aware microphysics and fire emission constraints. *Journal of Geophysical Research: Atmospheres*, **121**, 10294–10311. https:/doi.org/10.1002/2016JD025056

Saleeby, S. M., & Cotton, W. R. (2004). A large-droplet mode and prognostic number concentration of cloud droplets in the Colorado State University Regional Atmospheric Modeling System (RAMS). Part I: Module descriptions and supercell test simulations. *Journal of Applied Meteorology*, **43**(1), 182–195. https://doi.org/10.1175/1520-0450(2004)043<0182:ALMAPN>2.0.CO;2

Saleeby, S. M., & Cotton, W. R. (2008). A binned approach to cloud-droplet riming implemented in a bulk microphysics model. Journal of applied meteorology and climatology, **47**(2), 694–703. https://doi.org/10.1175/2007JAMC1664.1

Saleeby, S. M., & van den Heever, S. C. (2013). Developments in the CSU-RAMS aerosol model: Emissions, nucleation, regeneration, deposition, and radiation. *Journal of Applied Meteorology and Climatology*, **52**(12), 2601–2622. https://doi.org/10.1175/jamc-d-12-0312.1

Saleeby, S. M., Herbener, S. R., van den Heever, S. C., & L'Ecuyer, T. (2015). Impacts of cloud droplet–nucleating aerosols on shallow tropical convection. *Journal of the Atmospheric Sciences*, **72**(4), 1369–1385. https://doi.org/10.1175/JAS-D-14-0153.1

Saltelli, A., Chan, K., & Scott, E. M. (2000). *Sensitivity Analysis*. New York: John Wiley.

Saltelli, A., Tarantola, S., & Chan, K. S. (1999). A quantitative model-independent method for global sensitivity analysis of model output. *Technometrics*, **41**(1), 39–56. https://doi.org/10.1080/00401706.1999.10485594

Santner, T. J., Williams, B. J., Notz, W. I., & Williams, B. J. (2003). *The design and analysis of computer experiments* (Vol. 1). New York: Springer.

Seifert, A., & Beheng, K. D. (2006). A two-moment cloud microphysics parameterization for mixed-phase clouds. Part 2: Maritime vs. continental deep convective storms. *Meteorology and Atmospheric Physics*, **92**(1–2), 67–82. https://doi.org/10.1007/s00703-005-0113-3

Seiki, T., & Nakajima, T. (2014). Aerosol effects of the condensation process on a convective cloud simulation. *Journal of the Atmospheric Sciences*, **71**(2), 833–853. https://doi.org/10.1175/JAS-D-12-0195.1

Seroka, G., Fredj, E., Khout, J., Dunk, R., Miles, T., & Glenn, S. (2018). Sea breeze sensitivity to coastal upwelling and synoptic flow using Lagrangian methods. *Journal of Geophysical Research: Atmospheres*, **123**, 9443–9461. https://doi.org/10.1029/2018JD028940

Sheffield, A. M., Saleeby, S. M., & van den Heever, S. C. (2015). Aerosol-induced mechanisms for cumulus congestus growth. *Journal of Geophysical Research: Atmospheres*, **120**(17), 8941–8952. https://doi.org/10.1002/2015JD023743

Shen, L., Sun, J., & Yuan, R. (2018). Idealized large-eddy simulation study of interaction between urban heat island and sea breeze circulations. *Atmospheric Research*, **214**, 338–347. https://doi.org/10.1016/j.atmosres.2018.08.010

Simpson, J. E. (1994). *Sea breeze and local winds*. Cambridge: Cambridge University Press.

Simpson, J. E., Mansfield, D. A., & Milford, J. R. (1977). Inland penetration of sea-breeze fronts. *Quarterly Journal of the Royal Meteorological Society*, **103**(435), 47–76. https://doi.org/10.1002/qj.49710343504

Smagorinsky, J. (1963). General circulation experiments with the primitive equations: I. The basic experiment. *Monthly Weather Review*, **91**(3), 99–164. https://doi.org/10.1175/1520-0493(1963)091<0099:GCEWTP>2.3.CO;2

Soderholm, J., McGowan, H., Richter, H., Walsh, K., Weckwerth, T., & Coleman, M. (2016). The Coastal Convective Interactions Experiment (CCIE): Understanding the role of sea breezes for hailstorm hotspots in eastern Australia. *Bulletin of the American Meteorological Society*, **97**(9), 1687–1698. https://doi.org/10.1175/BAMS-D-14-00212.1

Song, J. L. (1986). A numerical investigation of Florida's sea breeze - cumulonimbus interactions (Doctoral dissertation). Fort Collins, CO: Colorado State University.

Spark, E., & Connor, G. J. (2004). Wind forecasting for the sailing events at the Sydney 2000 Olympic and Paralympic Games. *Weather and Forecasting*, **19**(2), 181–199. https://doi.org/10.1175/1520-0434(2004)019<0181:WFFTSE>2.0.CO;2

Steele, C. J., Dorling, S. R., Von Glasow, R., & Bacon, J. (2013). Idealized WRF model sensitivity simulations of sea breeze types and their effects on offshore windfields. *Atmospheric Chemistry and Physics*, **13**(1), 443. https://doi.org/10.5194/acp-13-443-2013

Stein, U., & Alpert, P. (1993). Factor separation in numerical simulations. *Journal of the Atmospheric Sciences*, **50**(14), 2107–2115. https://doi.org/10.1175/1520-0469(1993)050<2107:FSINS>2.0.CO;2

Stevens, R. G., Loewe, K., Dearden, C., Dimitrelos, A., Possner, A., Eirund, G. K., ... & Romakkaniemi, S. (2018). A model intercomparison of CCN-limited tenuous clouds in the high Arctic. *Atmospheric Chemistry and Physics*, **18**(15), 11041–11071. https://doi.org/10.5194/acp-18-11041-2018

Storer, R. L., & van den Heever, S. C. (2013). Microphysical processes evident in aerosol forcing of tropical deep convective clouds. *Journal of the Atmospheric Sciences*, **70**(2), 430–446. https://doi.org/10.1175/JAS-D-12-076.1

Storer, R. L., van Den Heever, S. C., & Stephens, G. L. (2010). Modeling aerosol impacts on convective storms in different environments. *Journal of the Atmospheric Sciences*, **67**(12), 3904–3915. https://doi.org/10.1175/2010JAS3363.1

Tao, W. K., Chen, J. P., Li, Z., Wang, C., & Zhang, C. (2012). Impact of aerosols on convective clouds and precipitation. *Reviews of Geophysics*, **50**(2). https://doi.org/10.1029/2011RG000369

Tao, W. K., Li, X., Khain, A., Matsui, T., Lang, S., & Simpson, J. (2007). Role of atmospheric aerosol concentration on deep convective precipitation: Cloud-resolving model simulations. *Journal of Geophysical Research: Atmospheres*, **112**(D24). https://doi.org/10.1029/2007JD008728

Tharammal, T., Bala, G., & Noone, D. (2017). Impact of deep convection on the isotopic amount effect in tropical precipitation. *Journal of Geophysical Research: Atmospheres*, **122**(3), 1505–1523.

Thompson, W. T., Holt, T., & Pullen, J. (2007). Investigation of a sea breeze front in an urban environment. *Quarterly Journal of the Royal Meteorological Society*, **133**(624), 579–594. https://doi.org/10.1002/qj.52

Tijm, A. B. C., Van Delden, A. J., & Holtslag, A. A. M. (1999). The inland penetration of sea breezes. *Contributions to Atmospheric Physics*, **72**(4), 317–328.

Twomey, S. (1974). Pollution and the planetary albedo. *Atmospheric Environment*, **8**(12), 1251–1256. https://doi.org/10.1016/0004-6981(74)90004-3

Twomey, S., & Squires, P. (1959). The influence of cloud nucleus population on the microstructure and stability of convective clouds. *Tellus*, **11**(4), 408–411. https://doi.org/10.3402/tellusa.v11i4.9331

van den Heever, S. C., Carrió, G. G., Cotton, W. R., DeMott, P. J., & Prenni, A. J. (2006). Impacts of nucleating aerosol on Florida storms. Part I: Mesoscale simulations. *Journal of the Atmospheric Sciences*, **63**(7), 1752–1775. https://doi.org/10.1175/JAS3713.1

van den Heever, S. C., Stephens, G. L., & Wood, N. B. (2011). Aerosol indirect effects on tropical convection characteristics under conditions of radiative–convective equilibrium. *Journal of the Atmospheric Sciences*, **68**(4), 699–718. https://doi.org/10.1175/2010JAS3603.1

Varble, A. (2018). Erroneous attribution of deep convective invigoration to aerosol concentration. *Journal of the Atmospheric Sciences*, **75**(4), 1351–1368. https://doi.org/10.1175/JAS-D-17-0217.1

Verma, S., Boucher, O., Venkataraman, C., Reddy, M. S., Müller, D., Chazette, P., & Crouzille, B. (2006). Aerosol lofting from sea breeze during the Indian Ocean Experiment. *Journal of Geophysical Research*, **111**, 07208. https://doi.org/10.1029/2005JD005953

Verma, S., Pani, S. K., Kumar, D. B., Faruqi, A. R., Bhanja, S. N., & Mandal, M. (2016). Aerosol extinction properties over coastal West Bengal Gangetic plain under inter-seasonal and sea breeze influenced transport processes. *Atmospheric Research*, **167**, 224–236. https://doi.org/10.1016/j.atmosres.2015.07.021

Waite, M. L., & Khouider, B. (2010). The deepening of tropical convection by congestus preconditioning. *Journal of the Atmospheric Sciences*, **67**(8), 2601–2615. https://doi.org/10.1175/2010JAS3357.1

Walko, R. L., Band, L. E., Baron, J., Kittel, T. G. F., Lammers, R., Lee, T. J., Ojima, D., Pielke, R. A. Sr., Taylor, C., Tague, C., Tremback, C. J., & Vidale, P. L. (2000). Coupled atmosphere–biophysics–hydrology models for environmental modeling. *Journal of Applied Meteorology*, **39**(6), 931–944. https://doi.org/10.1175/1520-0450(2000)039<0931:CABHMF>2.0.CO;2

Walko, R. L., Cotton, W. R., Meyers, M. P., & Harrington, J. Y. (1995). New RAMS cloud microphysics parameterization part I: The single-moment scheme. *Atmospheric Research*, **38**(1–4), 29–62. https://doi.org/10.1016/0169-8095(94)00087-T

Wang, C. (2005). A modeling study of the response of tropical deep convection to the increase of cloud condensation nuclei concentration: 1. Dynamics and microphysics. *Journal of Geophysical Research: Atmospheres*, **110**(D21). https://doi.org/10.1029/2004JD005720

Wang, C. C., & Kirshbaum, D. J. (2017). Idealized simulations of sea breezes over mountainous islands. *Quarterly Journal of the Royal Meteorological Society*, **143**(704), 1657–1669. https://doi.org/10.1002/qj.3037

Wang, J., Ge, C., Yang, Z., Hyer, E. J., Reid, J. S., Chew, B. N., ... & Zhang, M. (2013). Mesoscale modeling of smoke transport over the Southeast Asian Maritime Continent: Interplay of sea breeze, trade wind, typhoon, and topography. *Atmospheric Research*, **122**, 486–503. https://doi.org/10.1016/j.atmosres.2012.05.009

Wang, S., & Sobel, A. H. (2017). Factors controlling rain on small tropical islands: Diurnal cycle, large-scale wind speed, and topography. *Journal of the Atmospheric Sciences*, **74**(11), 3515–3532. https://doi.org/10.1175/JAS-D-16-0344.1

Wellmann, C., Barrett, A. I., Johnson, J. S., Kunz, M., Vogel, B., Carslaw, K. S., & Hoose, C. (2018). Using emulators to understand the sensitivity of deep convective clouds and hail to environmental conditions. *Journal of Advances in Modeling Earth Systems*, **10**, 3103–3122. https://doi.org/10.1029/2018MS001465

Wellmann, C., Barrett, A. I., Johnson, J. S., Kunz, M., Vogel, B., Carslaw, K. S., & Hoose, C. (2020). Comparing the impact of environmental conditions and microphysics on the forecast uncertainty of deep convective clouds and hail. *Atmospheric Chemistry and Physics*, **20**(4), 2201–2219. https://doi.org/10.5194/acp-20-2201-2020

Wilson, J. W., & Megenhardt, D. L. (1997). Thunderstorm initiation, organization, and lifetime associated with Florida boundary layer convergence lines. *Monthly Weather Review*, **125**(7), 1507–1525. https://doi.org/10.1175/1520-0493(1997)125<1507:TIOALA>2.0.CO;2

Xian, Z., & Pielke, R. A. (1991). The effects of width of landmasses on the development of sea breezes. *Journal of Applied Meteorology*, **30**(9), 1280–1304. https://doi.org/10.1175/1520-0450(1991)030<1280:TEOWOL>2.0.CO;2

Yang, G. Y., & Slingo, J. (2001). The diurnal cycle in the tropics. *Monthly Weather Review*, **129**(4), 784–801. https://doi.org/10.1175/1520-0493(2001)129<0784:TDCITT>2.0.CO;2

Yu, H., Liu, S. C., & Dickinson, R. E. (2002). Radiative effects of aerosols on the evolution of the atmospheric boundary layer. *Journal of Geophysical Research: Atmospheres*, **107**(D12), AAC-3. https://doi.org/10.1029/2001JD000754

Yuter, S. E., & Houze Jr, R. A. (1995). Three-dimensional kinematic and microphysical evolution of Florida cumulonimbus. Part I: Spatial distribution of updrafts, downdrafts, and precipitation. *Monthly Weather Review*, **123**(7), 1921–1940. https://doi.org/10.1175/1520-0493(1995)123<1921:TDKAME>2.0.CO;2

Zhang, Y., Fu, R., Yu, H., Dickinson, R. E., Juarez, R. N., Chin, M., & Wang, H. (2008). A regional climate model study of how biomass burning aerosol impacts land-atmosphere interactions over the Amazon. *Journal of Geophysical Research: Atmospheres*, **113**(D14). https://doi.org/10.1029/2007JD009449

Zhong, S., Leone, J. M., & Takle, E. S. (1991). Interaction of the sea breeze with a river breeze in an area of complex coastal heating. *Boundary-Layer Meteorology*, **56**(1–2), 101–139. https://doi.org/10.1007/BF00119964